COMPOSITION DEPENDENT PROPERTIES OF QUATERNARY FULL HEUSLER ALLOYS EXHIBITING FERROMAGNETISM, ANTIFERROMAGNETISM AND FERRIMAGNETISM

A thesis submitted

by

BHARGAB DEKA

to

Indian Institute of Technology Guwahati

in

partial fulfillment of the requirement for the award of the degree of
Doctor of Philosophy in Physics

Department of Physics
Indian Institute of Technology Guwahati
Guwahati – 781039, Assam, India

August 2015

Statement

The work contained in the thesis entitled "Composition dependent properties of quaternary full Heusler alloys exhibiting ferromagnetism, antiferromagnetism and ferrimagnetism" has been carried out by me under the supervision of Prof. A. Srinivasan, at the Department of Physics, Indian Institute of Technology Guwahati. This work has not been submitted elsewhere for the award of any degree.

31st August 2015

Bhargab Deka

(Bhargab Deka)

Roll No: 09612126

Department of Physics

Indian Institute of Technology Guwahati

Guwahati - 781039

Certificate

It is certified that the work contained in the thesis entitled "Composition dependent properties of quaternary full Heusler alloys exhibiting ferromagnetism, antiferromagnetism and ferrimagnetism" submitted by Bhargab Deka, a Ph. D. student of the Department of Physics, Indian Institute of Technology Guwahati for the award of degree of Doctor of Philosophy has been carried out under my supervision. This work has not been submitted elsewhere for the award of any degree.

31st August 2015

(Dr. A. Srinivasan)
Professor
Department of Physics
Indian Institute of Technology Guwahati
Guwahati – 781039

Dedicated

to

my parents
&
my brother-in-law

Acknowledgements

At the outset, I would like to express my deepest gratitude to my thesis supervisor Prof. A. Srinivasan for giving me the opportunity to carry out my Ph.D. thesis work under his supervision. I am grateful to him for his constant encouragement, confidence and patience with me through all the years of my studentship.

I am grateful to my doctoral committee members, Prof. A. Perumal, Dr. S. Ghosh and Prof. P.S. Robi for reviewing my research work regularly and for all their valuable suggestions for my doctoral research. I am thankful to the present and former Head of the Department, Dr. P. Poulose, Prof. S. Basu, Prof. S. Ravi and all the faculty members of the Department of Physics for their support.

I am thankful to Dr. S. Ghosh and Mr. A. Kundu for helping me in the *ab initio* calculations of my work.

I am very much thankful to Dr. R.K. Singh, DMRL, Hyderabad for helping me to prepare the Mn-based alloys.

I am thankful to Dr. B.S.D.Ch.S. Varaprasad, Dr. Y.K. Takahashi and Prof. K. Hono of NIMS, Tsukuba, Japan, for their help in PCAR measurements of Mn-Co-V-Al samples.

I express my sincere thanks to the Technical officers and staffs of Department of Physics, CIF and Central workshop, for their support and cooperation during the use of XRD, VSM, SEM and workshop facilities in my Ph.D. work. I am thankful to all my seniors, friends, lab-mates and research scholars of IITG for their support and cooperation. My special thanks go to Dr. Sidananda Sarma, Dr. Rahul Das, Dr. Akhilesh Kr. Singh, Dr. Tribedi Bora, Dr. Shyni PC, Nisha, Anabil, Arnab, Bhagaban, Rajkumar and Buddhadeb.

I am thankful to Anabil Gayen for his support throughout the years.

I am deeply indebted to my parents, sister and brother-in law for their support and encouragements. Finally, my sincere thanks are due to all those who have helped me in whatever manner during my Ph.D. work, some of whom I may have inadvertently forgotten to mention in this acknowledgement.

Bhargab Deka

PREFACE

Theoretical prediction and subsequent experimental verifications of the half-metallic electronic band structure in ferromagnetic Co_2MnSi alloy have led to the development of several full Heusler alloy based spintronic devices. Half-metallic ferromagnets are characterized by novel electronic band structure with coexisting metallic conduction band for spin-up electrons and semiconducting behavior with energy band gap at the Fermi level for the spin-down electrons. This novel electronic structure results in 100% spin polarized electrons at the Fermi level. Total magnetic moment of half-metallic alloys can be related to the total number of valence electrons in their unit cell through Slater-Pauling (S-P) rule. Hence, the S-P rule can be used to engineer new half-metallic Heusler alloys with desired magnetic moment for fabricating efficient spintronic devices. Though 100% spin polarization has been theoretically predicted in several Heusler alloy compositions, the same has not been achieved in reality. Fermi level engineering by substituting a fourth element in the ternary Heusler compound provides a way to overcome this drawback. Prediction of half-metallic character in several quaternary Heusler alloys by *ab initio* calculations has also been subsequently validated experimentally. The strong potential of quaternary Heusler alloys in spintronic applications serves as motivation for exploring newer Heusler alloy compositions.

Several magneto-resistive devices have been fabricated using cobalt based full Heusler alloys as ferromagnetic electrode layers. Among these alloys, Co_2FeSi has the advantage of high Curie temperature (~1100 K) and high saturation magnetic moment ($6\mu_B$). Considering the advantages offered by quaternary alloys, it may be worthy to explore the effect of substituting Si with elements such as Ge and Ga in Co_2FeSi.

$Ru_2Y(Z_{1-x}Z'_x)$ and $(Ru_{1-x}X'_x)_2YZ$ alloys offer a means for obtaining both ferromagnetic and antiferromagnetic alloys in the same quaternary system by properly choosing the fourth element (X′ or Z′) and its concentration. Since an antiferromagnetic pinning layer is an essential part of a spin valve, such materials could lead to the realization of spin valves entirely made up of full Heusler alloy layers with superior interfacial properties and hence better performance. Half-metallic ferrimagnets is another class of spintronic materials which exhibit very low magnetic moment and hence very low stray fields due to internal spin compensation. There is considerable interest in obtaining full Heusler alloys with zero total magnetic moment. *Ab initio* studies showed that Co substitution for Mn in ferrimagnetic $Mn_2VAl(Si)$ compounds can lead to a zero magnetic moment or fully compensated ferrimagnet (FCF).

In an attempt to address some of these important issues associated with the development of full Heusler alloy based spintronic materials, this thesis work explores the structural, magnetic and spintronic properties of following series of Heusler alloys: (1) $Co_2FeGe_{1-x}Si_x$ and $Co_2FeGa_{1-x}Si_x$, (2) $Ru_2FeSi_{1-x}Ge_x$ and $(Ru_{1-x}Co_x)_2FeSi$, and (3) $(Mn_{1-x}Co_x)_2VAl$ and $(Mn_{1-x}Co_x)_2VGa$. These alloys were prepared by arc melting method. *Ab initio* calculations have been performed using generalized gradient approximation (GGA) and GGA+U methods, where U is the Hubbard potential. The thesis consists of six chapters.

Chapter 1 provides a brief introduction to the content of the thesis. A review of literature related to the thesis work is also included in this chapter.

Chapter 2 discusses the experimental and computational techniques used in the investigations.

Chapter 3 reports the effect of substitution of Z element with another *sp*-valent element Z′ on the structural and magnetic properties of a ferromagnetic full Heusler alloy. Here, $Co_2FeZ_{1-x}Z'_x$ alloys with Z = Ge, Ga, Z′ = Si and $0 \leq x \leq 1$ have been investigated. Co_2FeSi alloys crystallize in $L2_1$ structure but the characteristic super-lattice peaks are absent in the XRD patterns of the alloys containing high Ge and Ga concentrations. All alloy compositions exhibit ferromagnetic behavior with high T_C. The Rhodes-Wohlfarth (R-W) ratio estimated for all the alloy compositions is less than unity, indicating half-metallic character in these alloys. The effective anisotropy constant (K_{eff}) of the alloys ($\sim 10^5$ Jm^{-3}) showed an increase with increase in *x*. *Ab initio* calculations have been performed using GGA and GGA+U for alloy compositions with $L2_1$ structure and DO_3 disorder in order to account for experimentally measured magnetic properties. Saturation magnetization (M_s) of Co_2FeGe remains unaffected by the introduction of disorder. However, M_s decreases for other alloy compositions with Z = Ge. Variation of percentage of DO_3 type disorder in these alloys shows that half-metallicity cannot be sustained in alloy with $x = 1$ if this type of disorder is present in amounts $\geq 12.5\%$. For the alloys with Z = Ga, the total magnetic moment is accurately predicted by the GGA formalism which gets overestimated by the inclusion of U for alloys $x \leq 0.25$. This indicates that the electron repulsion is less dominant in alloys containing higher amounts of Ga. For the case of $L2_1$ structure, 100% spin polarization was obtained for alloys with $x = 0.25$, 0.50, 0.75 and 1.00. However for the alloy with $x = 0$, a slight decrease in spin polarization was observed. Introduction of DO_3 disorder destroys half-metallicity for alloys with $x = 0$, 0.25 and 0.50. Thus, *ab initio* calculations help in interpreting the experimental results obtained in both series of $Co_2FeZ_{1-x}Z'_x$ alloys.

Chapter 4 describes the possibility of obtaining both ferromagnetism and antiferromagnetism in the same alloy system. In order to understand the transition from antiferromagnetism to ferromagnetism, $Ru_2FeSi_{1-x}Ge_x$ and $(Ru_{1-x}Co_x)_2FeSi$ alloys have been studied. The (111) super-lattice peak was absent in the XRD pattern of all $Ru_2FeSi_{1-x}Ge_x$ alloys which shows that the alloys crystallize in the disordered *B*2 structure. Ru_2FeSi alloy was antiferromagnetic with a Néel temperature of 270 K. As Ge concentration is increased from $x = 0.25$ to $x = 1.00$, magnetization value starts increasing due to development of ferromagnetic interaction. A*b initio* calculations performed on these alloys with $L2_1$ and B2 structures provide reasons for antiferromagnetic and ferromagnetic order exhibited by $x = 0$ and $x > 0$ alloys, respectively. XRD pattern of Ru_2FeSi alloy reveals a disordered B2 structure and so it is expected to be an antiferromagnet. However, magnetic measurements show that alloys with $x = 0.25$, 0.50, 0.75 and 1.00 are ferromagnetic despite the absence of the characteristic (111) reflection of $L2_1$ structure in their XRD patterns. The reason for this unexpected result lies in the nearly equal scattering factors of Fe and Ge atoms which reduces the intensity of (111) reflection below the detectable limit despite the structure being $L2_1$. XRD patterns of Ru rich compositions of $(Ru_{1-x}Co_x)_2FeSi$ alloys *i.e.*, $x = 0$ and $x = 0.25$, exhibited disordered B2 structure. However, with further increase in Co concentration, $L2_1$ order appeared in the alloys. Magnetization measurements also confirmed that with increasing x, the ferromagnetic state becomes dominant with the appearance of spontaneous magnetization and increase in the value of magnetization and T_C of the alloys.

Chapter 5 deals with the properties of ferrimagnetic Mn_2VGa and Mn_2VAl and experimental evidence of a fully compensated ferrimagnet (FCF) in this alloy system by

substituting Mn with Co. Both $(Mn_{1-x}Co_x)_2VZ$ (Z = Al, Ga) alloy series crystalize in highly ordered $L2_1$ structure. T_C of the alloys was found to decrease with increased Co substitution which can be attributed to the reduction in magnetic moment due to the appearance of antiferromagnetic interaction between Mn and Co atoms. M_s for the alloys with x = 0, 0.25 and 0.50 are $1.88\mu_B$ ($2.0\mu_B$), $0.84\mu_B$ ($1.0\mu_B$) and $0.07\mu_B$ ($0\mu_B$), respectively for Z = Al and $1.84\mu_B$ ($2.0\mu_B$), $0.85\mu_B$ ($1.0\mu_B$) and $0.30\mu_B$ ($0\mu_B$), respectively for Z = Ga, where the values in bracket are those predicted by S-P rule for the nominal composition. This deviation from theoretical values can be explained in terms of small variation in stoichiometry and weaker hybridization between Co–V states as compared to that of Mn–V states resulting in domination of Mn-V antiferromagnetic interaction over Co-V ferromagnetic one. It is evident that Co substitution for Mn in $Mn_2VAl(Ga)$ decreases M_s and leads to a FCF for equal amounts of Co and Mn *i.e.*, in MnCoVAl(Ga) alloy. Point contact Andreev reflection measurements have been performed on $(Mn_{1-x}Co_x)_2VAl$ alloys and the intrinsic spin polarization was found to increase from 0.57 for x = 0 to 0.60 for x = 0.50. This clearly shows high spin polarization in the alloys which is also a measure of its half-metallic character.

Chapter 6 serves as a concluding chapter where the scope for future work in this area is also pointed out in brief.

References and list of publications which have originated out of this thesis work are listed at the end of the thesis.

Contents

Chapter 1

INTRODUCTION

Though the history of magnetism can be traced back to many centuries, it is only in the last century that scientists have begun to exploit it for technological developments. Practically, all naturally occurring magnetic materials contain iron and until 20th century, all magnetic materials synthesized contained at least one of the ferromagnetic elements, *viz*.., iron, cobalt or nickel. In 1903, German mining engineer and chemist, Friedrich Heusler found that copper-manganese alloyed with the elements tin, aluminium, arsenic, antimony, bismuth or boron exhibited ferromagnetic behavior [FHEU03a]. These ternary intermetallic compounds aptly named as Heusler alloys, received enormous attention because of their ferromagnetic behavior despite none of the constituent elements being ferromagnetic. This discovery promoted numerous theoretical and experimental investigations resulting in the identification of many Heusler alloy compounds with diverse magnetic properties. In fact, almost all known quantum mechanical ground states of solids are represented within this class of alloys. These include, ferromagnets (say, Cu_2MnAl [FHEU03a]), ferrimagnets (say, Mn_2VAl [HITO83a]), antiferromagnets (say, Ru_2MnGe [TKAN06a]), semiconductors (say, Fe_2VAl [YNIS97a]), heavy fermion systems (say, Cu_2CeIn [HNAK88a]), and superconductors (say, Ni_2ZrGa [JWIN08a]). Heusler compounds can be classified as full and half (or semi) Heusler alloys on the basis of their chemical formula and crystal structure.

1.1 CRYSTAL STRUCTURE OF HEUSLER ALLOYS

Full Heusler alloys with general chemical formula X_2YZ (where, X and Y are transition metals and Z is a main group element) crystallize in the cubic structure (represented by the point $L2_1$ and space group $Fm\bar{3}m$) with Cu_2MnAl as prototype [FHEU03a, OHEU34a, AJBR34a]. The X atoms form a primitive cubic sub-lattice and adjacent

cubes of this X sub-lattice are filled alternatively by Y or Z atoms (*c.f.* Figure 1.1(a)). The primitive cell of the $L2_1$ structure contains four atoms that form the base of a face centred cubic (fcc) primitive cell. The result is a lattice with $Fm\bar{3}m$ symmetry in which the Wyckoff positions 4a (0,0,0), 4b (½,½,½), and 8c (¼,¼,¼ and ¾,¾,¾) are occupied by Z, Y, and X atoms, respectively.

Half Heusler alloys with general chemical formula of XYZ, crystallize in a non-centrosymmetric cubic structure (point group $C1_b$ and space group $F\bar{4}3m$) which is a ternary ordered variant of CaF_2 structure and can be derived from the tetrahedral ZnS-type structure by filling the octahedral lattice sites (*cf.* Figure 1.1 (b)). $C1_b$ compounds of composition XYZ consist of three interpenetrating fcc sub-lattices, each of which are occupied by the X, Y and Z atoms [KWAT76a, RADE83a]. The corresponding occupied Wyckoff positions are 4a (0,0,0), 4b (½,½,½), and 4c (¼,¼,¼). In other words, the $C1_b$ unit cell can be visualized as an $L2_1$ unit cell with one unoccupied sub-lattice.

In X_2YZ compounds, if the Y element has more valence electrons than the X element and if both the elements are from the same period, an inverse Heusler structure (space group $F\bar{4}3m$) is observed (*c.f.* Figure 1.1 (c)). Such a structure may also appear in compounds with transition metals from different periods [MPUS69a]. Unlike the normal Heusler structure where all of the X atoms fill tetrahedral positions, in the inverse Heusler structure, X and Z atoms form a rock salt lattice to achieve octahedral coordination for X atoms and the remaining X and Y atoms fill tetrahedral sites with four-fold symmetry. Though this structure is still described by four interpenetrating fcc sub-lattices, the X atoms do not form a simple cubic lattice. Instead, they are placed at Wyckoff positions 4b (½,½,½) and 4d (¾,¾,¾), while the Y and Z atoms are located at

4c (¼,¼,¼) and 4a (0,0,0) sites, respectively. $AgLi_2Sb$ is the prototype of this structure [HPAU68a]. In order to emphasize the difference in the structures of inverse Heusler alloys and normal Heusler compounds, the former is expressed with the formula (XY)XZ. Inverse Heusler structure is frequently observed in Mn_2-based alloys with atomic number of Y being larger than the atomic number of Mn. Mn_2CoSn or (MnCo)MnSn is the most prominent example of this type of structure [VVSU90a, NLAK02a].

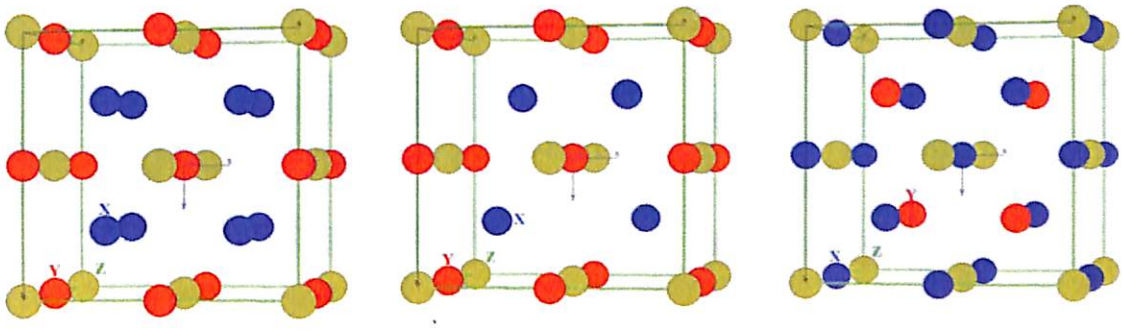

(a) (b) (c)

Figure 1.1: Unit cells of (a) full, (b) half, and (c) inverse Heusler compounds.

1.2 ATOMIC DISORDER IN FULL HEUSLER ALLOYS

Properties of Heusler alloys are strongly dependent on the nature of atomic arrangement of the atoms within the unit cell. Band structure calculations show that even small amounts of disorder in the distribution of atoms on lattice sites induce distinct changes in their electronic structure, which in turn influence their magnetic and transport properties [YMIU04a, SPIC04a, HCKA07a]. Therefore, a careful analysis of the crystal structure is essential to understand the structure-property correlation in Heusler compounds.

The most prominent disorders in full Heusler alloy structures [PJWE69a, GEBA71a, KRAZ01a, MHOR04a, TGRA09a] are shown in Figure 1.2.

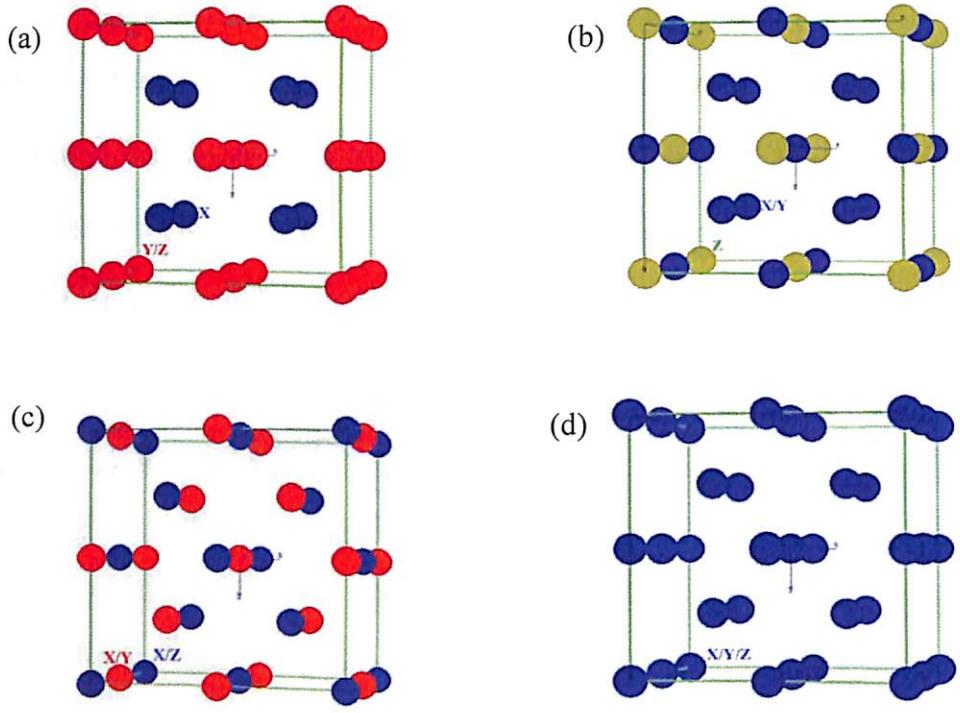

Figure 1.2: Changes in the atomic arrangement in the unit cell of full Heusler alloys due to (a) B2, (b) DO_3, (c) B32a and (d) A2-type disorders.

The most frequent type of disorder encountered in a full ordered $L2_1$ structure is the B2-type disorder which results in the CsCl-like structure shown in Figure 1.2 (a). In B2-type disordered structure, the Y and Z atoms are equally distributed in the unit cell and consequently the 4a and 4b positions become equivalent. As a consequence, the symmetry is reduced, resulting in $Pm\bar{3}m$ space group. On the other hand, the random distribution of X and Y or X and Z leads to a DO_3-type disorder or BiF_3-like structure depicted in Figure 1.2 (b) with $Fm\bar{3}m$ space group. The NaTl-like structure occurs very rarely, when the X -atoms, which occupy one of the fcc sub-lattices, are mixed with the Y atoms, whereas the X atoms on the second sub-lattice are mixed with the Z atoms. This

kind of disorder is also known as B32a-type disorder (space group $Fd\bar{3}m$) which is shown in Figure 1.2 (c). It can be seen that in this case, the X atoms are placed at Wyckoff position 8a (0,0,0), while Y and Z are randomly distributed at 8b (½,½,½) position. In contrast to these partial atomic site disorders, if all Wyckoff positions become equivalent, then A2-type of complete disorder is obtained, resulting in W-like bcc structure (depicted in Figure 1.2 (d)) with space group $Im\bar{3}m$.

Some of these disorders can be detected and estimated using X-ray diffraction (XRD) patterns of the alloys. For full Heusler compounds, we can divide all possible X-ray reflections (those allowed by the extinction rules for the fcc lattice) into three groups with three different structure factors [ASZY89a], *viz.*,

1. h, k, l all odd → ((111), (311), (331), (333), (511), (531),...)

   or $F(111) = 4(f_y - f_z)$ (1.1)

2. h + k + l = 2(2n − 1), n = 1, 2, . . . → ((200), (222), (420), (600), (442),...)

   or $F(200) = 4[2f_x - (f_y + f_z)]$ (1.2)

3. h + k + l = 4n, n = 1, 2, . . . → ((220), (400), (422), (440), (620), (444),...)

   or $F(220) = 4[2f_x + f_y + f_z]$ (1.3)

where f_x, f_y and f_z are average scattering amplitudes of the respective sub-lattices and h, k, l are the Miller indices of the crystal planes. The structure factors expressions given above are simplified forms obtained after neglecting the anomalous correction terms. The third group of reflections is independent of atomic disorder(s) in the four sub-lattices, making it a fundamental reflection. The other two groups of reflections depend on disorder. The first group vanishes if B2 disorder is present while the second group vanishes if A2 disorder is present in the alloy. However, it should be noted that some

types of disorders such as DO_3 cannot be easily detected by XRD, especially when the scattering coefficients of the concerned 3d transition metals are nearly equal [BBAL07a].

1.3 MAGNETIC PROPERTIES OF FULL HEUSLER ALLOYS

Heusler alloys exhibit interesting and diverse magnetic phenomena like ferromagnetism, ferrimagnetism, antiferromagnetism, helimagnetism, Pauli parmagnetism, *etc*. Majority of known Heusler alloys are ferromagnets that attain magnetic saturation at relatively low applied fields. Ferromagnetism occurs mainly because of quantum mechanical exchange interactions between electrons in a material. For a single atom, the magnetic moment is mainly due to the exchange interaction of the electrons within the shells of the atom. For transition metals, the 3*d* shell is responsible for the atomic moment. Atomic spin moment of transition elements can be calculated using Hund's rule [BDCU08a]. However, atomic magnetic moments do not always lead to ferromagnetism. Additional interatomic interaction is required for ferromagnetic coupling between the individual atomic moments. Depending upon the system, different theoretical approaches could be found in the literature to describe the ferromagnetic interaction. Four fundamental exchange interactions are discussed below:

1. Band magnetism

   For free atoms, the electrons occupy sharply defined energy levels in accordance with the Pauli's exclusion principle. However, when atoms are brought close together to form a solid, the energy level positions get greatly modified. For example, when two atoms containing two electrons each in their 1*s* level approach close to each other, their electron clouds overlap with each other. Now the Pauli's principle applies to them as a single unit which prevents them from having a

single 1*s* level with four electrons. So the 1*s* level must split into two levels with two electron in each. In transition elements, 3*d* and 4*s* electron clouds are first to overlap and the corresponding levels get split first. Elements with filled energy levels cannot contribute a magnetic moment as they contain exactly two electrons with opposite spin, which cancel each other. If we consider a situation where 10 atoms containing one electron each form a solid which will result in splitting of the single level in the free atom into 10 levels, then the lower five levels will contain two electrons each. However if spin of one electron gets reversed, a spin unbalance of 2 will be created resulting in a magnetic moment of 2/10 or $0.2\mu_B$ per atom. The exchange force is responsible for creating this spin unbalance in a ferromagnet. For a metal to possess ferromagnetism, it should fulfill certain criteria given below [BDCU08a]:

- Partially filled bands must be available for electrons with unpaired spin to move into.
- The density of levels in the band must be high so that the increase in energy due to spin alignment is small.
- The distance between atoms must be right so that the exchange force can cause the *d*-electron spins in one atom to align the spins in the neighboring atoms.

2. Direct exchange

This interaction is a direct consequence of Pauli's exclusion principle and depends strongly on the overlap of the participating wave functions. For small interatomic distances, antiferromagnetic coupling occurs (as in case of Cr and

Mn). When the interatomic distance increases, ferromagnetic state becomes favorable (as in case of Fe, Co, Ni). For very large distances, the coupling vanishes resulting in paramagnetism [AAHA01a]. This behavior is illustrated in Bethe-Slater plot shown in Figure 1.3 (BDCU08a). The plot displays the sign and magnitude of the direct exchange integral (J_{ex}) as a function of interatomic distance (r_{ab}) of the concerned elements. J_{ex} is negative for antiferromagnetic coupling and positive for ferromagnetic coupling. If the interatomic distance is too large, as in most ferromagnetic materials, the direct exchange interaction is too weak to mediate the ferromagnetism.

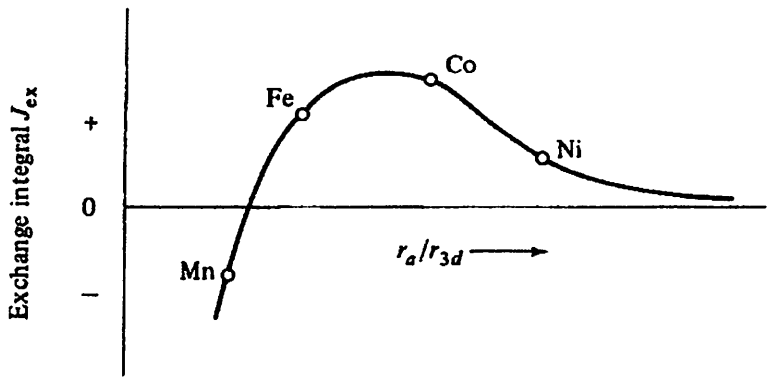

Figure 1.3: Bethe-Slater curve [after BDCU08a].

3. RKKY exchange

RKKY indirect exchange interaction (after Rudermann, Kittel, Kasuya and Yosida) takes over at distances beyond a few atomic spacing. It is mediated by the conduction electrons (s, p). A magnetic moment at site *i* polarizes the s, p-electron gas and a second moment at site *j* feels the induced polarization. This interaction starts up as ferromagnetic at small distances and oscillates between negative and positive values with a period of $\lambda_F/2$, where $\lambda_F = 2\pi/k_F$ is the Fermi wavelength

and k_F is the Fermi wave-vector. In general, the RKKY interaction gives rise to ferromagnetism if k_F is small (in nearly empty conduction band) and to antiferromagnetism when $k_F \sim \pi/a$ (in half-filled conduction band). This interaction can lead to long period magnetic structures (helimagnets, etc), that can be incommensurate with the lattice spacing. This mechanism is responsible for the oscillatory interlayer exchange coupling in giant magneto-resistance (GMR) structures [PGRU86a, PBRU91a] and the coupling of 4*f* electrons in rare earth elements [SBLU01a].

4. Super exchange

   In the absence of conduction electrons, RKKY coupling cannot be present. Nevertheless, antiferromagnetic coupling is observed in MnO and MnF_2 [FCAR00a]. This finding is attributed to the occurrence of the so-called super exchange interaction. This coupling is mediated by the presence of diamagnetic atoms. The diamagnetic atom provides one electron to the magnetic atom obeying Hund's rules. Hence, the diamagnetic ion becomes paramagnetic and couples *via* direct exchange to the next magnetic atom. This complex mechanism can induce ferromagnetic and antiferromagnetic coupling characters [CZEN53a].

The origin of ferromagnetic behavior in Heusler alloys is complicated and is not yet completely understood. Firstly, a direct exchange coupling is not realistic due to the large interatomic distance of both the X and Y atoms in Heusler alloys [PJWE69a]. A description based on pure itinerant electrons, which was successfully applied to the case if 3d transition metals, is also unrealistic due to the localization of the magnetic moments at Y (usually Mn) atomic sites [JKUB83a]. However, the presence of two of the

transition metals would favor at least a partly band-like contribution to the ferromagnetic coupling. Starting from the simple Heusler alloy Cu_2MnAl, it is possible to extract some features of the essential Mn-Mn interatomic coupling. As indicated before, direct exchange is impossible due to the large interatomic distance (about 4.2 Å) [PJWE81a]. Zener proposed a model including a direct and an indirect exchange mechanism [CZEN53a]. In this model, the direct contribution always provides antiferromagnetic coupling, whereas the indirect interaction *via* the 4*s* conduction electrons couples ferromagnetically. Zener's simple model finds its quantum mechanical foundation in the oscillatory RKKY interaction proposed as the coupling mechanism between separate Mn atoms [SPIC02a, IGAL02a]. In contrast, Kubler proposed a super exchange type of mechanism for the Mn coupling [JKUB83a]. Coupling through the diamagnetic group III-V element can be an alternative or an addition to the RKKY mechanism. In Cu_2MnAl, a coupling through Cu atoms can be neglected. If these Cu atoms are replaced by Co atoms, as in Co_2MnSi, the magnetic configuration becomes more complicated. Kubler again proposed an indirect coupling of Mn atoms through Co atoms [JKUB83a]. Alternatively, exchange interaction by means of the common *d* bands of Mn and Co hybridization is utilized in band structure calculations [SPIC02a].

In some materials, the atomic moments couple in an antiparallel arrangement leading to zero net moment antiferromagnets. In a crystalline material, the structure dictates the arrangement of antiparallel spins. Although the majority of Heusler alloys are ferromagnetic, some of them order antiferromagnetically, especially, those compounds containing 3*d* element in which the magnetic moment is carried only by Mn atoms at Y site. Experimentally, antiferromagnetic order has been observed in both half Heusler

(with $C1_b$ structure) and full Heusler alloys (with $L2_1$ and B2 structures). Antiferromagnetism appears to be more favorable in full Heusler alloys with B2-type crystal structure. In fact, antiferromagnetic behavior has been reported in several B2-type disordered X_2MnZ (where X = Ni, Pd and Z = Al, In) alloys [PJWE88a]. For example, Ni_2MnAl is ferromagnetic in its $L2_1$ state [FGJI99a]. However, when the B2 disorder occurs, the smaller neighboring Mn–Mn distance with respect to the $L2_1$ phase, leads to the stabilization of an antiferromagnetic interaction [IGAL11a]. In the $L2_1$ structure, the nearest Mn atoms are separated by $a/\sqrt{2}$ distance while in B2 structure, the closest Mn–Mn distance is $a/2$. In $L2_1$ structure, the interaction between the nearest neighbor (NN) Mn atoms is ferromagnetic giving rise to ferromagnetism in the alloy. However for B2 disorderd alloy, the nearest neighbor Mn atoms interact antiferromagnetically. This picture is consistent with the Bethe–Slater curve for transition metals which represents the behavior of the exchange energy as a function of the ratio of the NN distance over the radius of the *d*-orbitals as shown in Figure 1.3. When the ratio decreases, the exchange energy becomes negative leading to an antiferromagnetic state. Many Ru based full Heusler alloys (Ru_2MnZ (Z = Si, Ge, Sn, Sb) [SMIZ09a, TKAN06a], Ru_2FeSi [SNMI85a, ASZY89a], Ru_2CrGe [HOKA08a]) have been reported to be antiferromagnetic. Theoretical investigations on Ru_2MnZ alloys show that as opposed to Ni_2MnAl alloy, these alloys shows antiferromagntic ordering even in fully ordered $L2_1$ state.

When two antiferromagnetically coupled sub-lattices in a material have unequal moments (usually because of different atomic species in different sites), the net moment is not zero. This weakly magnetic state is called ferrimagnetism. Ferrimagnetic Heusler

alloys are fewer as compared to ferromagnetic ones. Mn_2VZ (Z = Al, Ga, Si, In, Ge, Sn) alloys have been shown through *ab initio* calculations to possess a ferrimagnetic ground state [KOZD06a]. Neutron diffraction studies on Mn_2VAl compound also provide evidence of ferrimagnetic coupling between Mn and V atoms in these alloys [HITO83a]. Formation of ferrimagnetic ordering in Mn_2VAl is due to the parallel alignment of all Mn with respect to each other and oppositely aligned V moments [ESAS05a]. Due to internal spin compensation, ferrimagnetic alloys have low magnetic moment but exhibit high Curie temperature.

Apart from exhibiting diverse magnetic properties, Heusler alloys also display a wide range of multifunctional properties such as magneto-optical [PGVA83a], magneto-caloric [TKRE05a, RKAI06a] and thermoelectric [SSAK05a] effects. A very important aspect of Heusler compounds is their magneto-optical behavior. Magneto-optical effects involve various changes in the polarization state of light upon interaction with materials possessing a net magnetic moment, including rotation of the plane of linearly polarized light (Faraday and Kerr rotations), and the complementary differential absorption of left and right circularly polarized light (circular dichroism). Discovery of an extremely large Kerr rotation in half Heusler compound MnPtSb (-1.27° at 300 K and 5° at 80 K) demonstrated the technological relevance of such compounds in the context of magneto-optical reading and recording [PGVA83a, RCAR00a]. Several Hesuler compounds are potential candidates for both solar cell and thermoelectric applications. In fact, excellent thermoelectric properties have recently been demonstrated by TiNiSn-based [SSAK05a] and Fe_2VAl-based alloys [YNIS11a]. By applying an alternating magnetic field, faster shape or volume change or mechanical strain can be achieved in some ferromagnetic

Heusler alloys called ferromagnetic shape memory alloys (FSMAs) which have the potential to be the next generation 'very smart' actuator materials. In FSMAs, the magnetic and structural properties are strongly coupled with each other, which is rather rare in condensed matter systems. Such coupled phenomena in solids can lead to many interesting properties such as magneto-caloric effect (MCE) and magnetic field induced strain (MFIS) which have many technological applications. Off-stoichiometric Ni-Mn-X (Ga, In, Sn, Sb) based full Heusler alloys shows ferromagnetic shape memory effect. Ni-Mn-Ga is the prototype Heusler alloy based FSMA [PJWE84a, KULL96a, KULL97a]. After the discovery of Ni2MnGa FSMA, several off-stoichiometric Heusler alloys such as Co-Ni-Al [RKAI96a, KOIK01a, KOIK01b], Ni-Mn-Al [FGEJ99], Co-Ni-Ga [KOIK01b, MWUT01a], Fe-Ni-Ga [KOIK02a, KOIK02b] have also been found to display ferromagnetic shape memory effect. Magnetic field induced strain (MFIS) in single crystalline Ni-Mn-Ga alloys has reached a remarkable value of 10% [ASOZ02a, JPON08a] with a field response time of less than a millisecond. MCE has been observed in a host of Ni–Mn–Ga [ANVA99a], Ni–Mn–Sn [TKRE05a], Ni–Mn–In [TKRE07a] alloys. High MCE exhibited by Ni-Mn-In-Si [RDAS11a, RDAS13a, RDAS13b] alloys make them suitable for use as room temperature magnetic refrigerants.

1.4 HALF-METALLIC HEUSLER ALLOYS

Recent discovery of half-metallicity in half Heusler alloy NiMnSb by de Groot *et al.* [RADE83a] and subsequently in full Heusler compound Co_2MnSi [JKUB83a] marked the advent of a new class of materials called half-metals. Half-metallic ferromagnets are characterized by novel electronic band structure with coexisting metallic conduction band

for spin-up electrons and semiconducting behavior with energy band gap at the Fermi level for the spin-down electrons. This novel electronic structure results in 100% spin polarized electrons at the Fermi level. Since this pioneering work, several full and half Heusler alloys have been predicted to be half-metallic. Apart from Heusler alloys, half metallicity has also been found in other systems such as oxides (*e.g.* CrO_2 [RJSO98a]), manganites (*e.g.* $La_{0.7}Sr_{0.3}MnO_3$ [RJSO98a]), double perovskites (e.g. Sr_2FeReO_6 [HKAT04a]), pyrites (*e.g.* CoS_2 [TSHI01a]) and transition metal chalcogenides (*e.g.* CrSe [IGAL02a, IGAL03a]). However, among the proposed half-metallic ferromagnets, the Heusler alloys hold the greatest potential due to their lattice constant match with the III-V semiconductors, very high Curie temperature and large band gap at Fermi level [PJWE88a]. Since half-metals are the materials of interest to this thesis work, their salient features are discussed below.

1.4.1 Spin Polarization

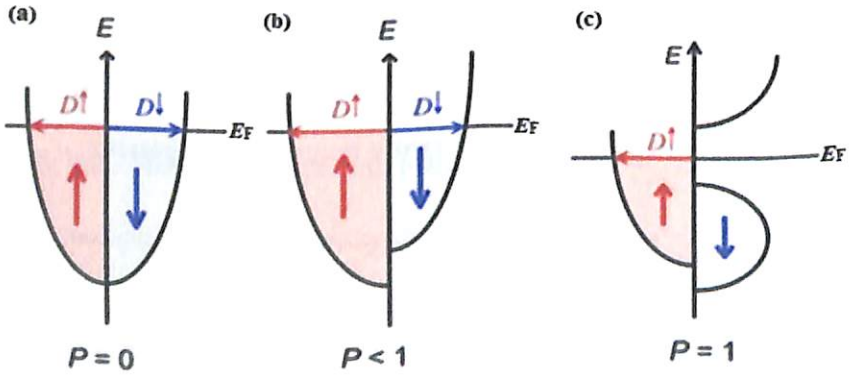

Figure 1.4: Electronic structure near E_F of a (a) Pauli's paramagnet, (b) ferromagnet and (c) ferromagnetic half-metal. P is the electron spin polarization as defined by Eq. (1.4) [WWWNa].

Spin polarization is defined as the ratio of the density of states of spin-up and spin-down electrons at a Fermi level [RJSO98a],

$$P = \frac{D_{\uparrow}(E_F) - D_{\downarrow}(E_F)}{D_{\uparrow}(E_F) + D_{\downarrow}(E_F)} \tag{1.4}$$

Since the density of states of spin-up and spin-down electrons are equal in paramagnetic materials, $P = 0$ for paramagnetic materials as depicted in Figure 1.4(a). On the other hand, the density of spin-up states is more than the spin-down states in ferromagnetic materials and so P is larger than 0, but smaller than 1 as shown in Figure 1.4(b). However, for half-metals, since only spin-up electrons are present at the Fermi level with no spin-down electrons, $P = 1$ (*c.f.* Figure 1.4(c)). To understand the scientific interest in half-metallic compounds, one can consider the case of a typical transition metal ferromagnet. While the elements cobalt and nickel have fully polarized $3d$ bands, they are not half-metals because the Fermi level crosses the (unpolarized) $4s$ band, thereby lowering the polarization to about 40% [JMDC04a]. On the other hand, the hybridization can be employed to gain access to the complete polarization of the d band by either raising the $4s$ band above the Fermi level or depriving the system of electrons until the Fermi level is situated below the $4s$ band. This explains why there are no half-metals among pure elements at all. However, half-metallicity can be realized when the pure metal becomes a component of an alloy or a compound. Heusler compounds are of particular interest in this respect, because Heusler compounds retaining their cubic crystal structure for a wide range of composition variation.

1.4.2 Origin of the gap in full Heusler alloys

The origin of half-metallicity in full-Heusler alloys was initially described by Galanakis *et al.* [IGAL02b] for the compound Co_2MnGe. In this interpretation, the lattice is initially treated as made up of only the Co_2 positions, and the hybridization of *d*-orbitals of the minority states in Co-Co interactions are calculated first. These are shown in Figure 1.5(a). In the figure, d_1 to d_5 correspond to $d_{xy}, d_{yz}, d_{zx}, d_{3z^2}$ and $d_{x^2-y^2}$ orbitals, respectively. Between two neighboring Co atoms in the lattice, two hybridized orbitals form from the d_4 and d_5 orbitals, leading to the formation of a low energy bonding e_g orbital and a high energy e_u antibonding orbital. The d_1, d_2 and d_3 orbitals hybridize to form a triply degenerate low energy bonding t_{2g} orbital and a triply degenerate high energy antibonding t_{1u} orbital, where t_{1u}, t_{2g}, e_g and e_u are the chemical nomenclature describing the shape (angular momentum) of the hybrid orbital. The contribution from the Mn atoms in the lattice must also be considered as well as the Co-Co interaction. The *d*-orbitals from the Mn atoms hybridize in a similar way as seen in the case of Co-Co. Figure 1.5(b) shows that the d_4 and d_5 orbitals hybridize with the double degenerate e_g orbital of the Co-Co to form two e_g orbitals, *viz.*, one low energy bonded and one high energy antibonded orbital. The d_1, d_2, and d_3 orbitals also hybridize with the triple degenerate t_{2g} orbital from the Co-Co to form 6 more t_{2g} orbitals, three of which are bonding and sit below the Fermi energy and another three which are antibonding and are of higher energy. This interaction with the Mn leaves 5 hybridized orbitals from the Co-Co interaction free. The three t_{1u} orbitals sit just below Fermi energy while the two e_u orbitals sit just above E_F. The result of this is the formation of an energy gap in the band structure at E_F for the minority spin channel. This treatment of the interatomic

interactions does not include any contributions from the Z (= Ge, in this case) element. This short-coming was subsequently addressed by other researchers [SIFU95a].

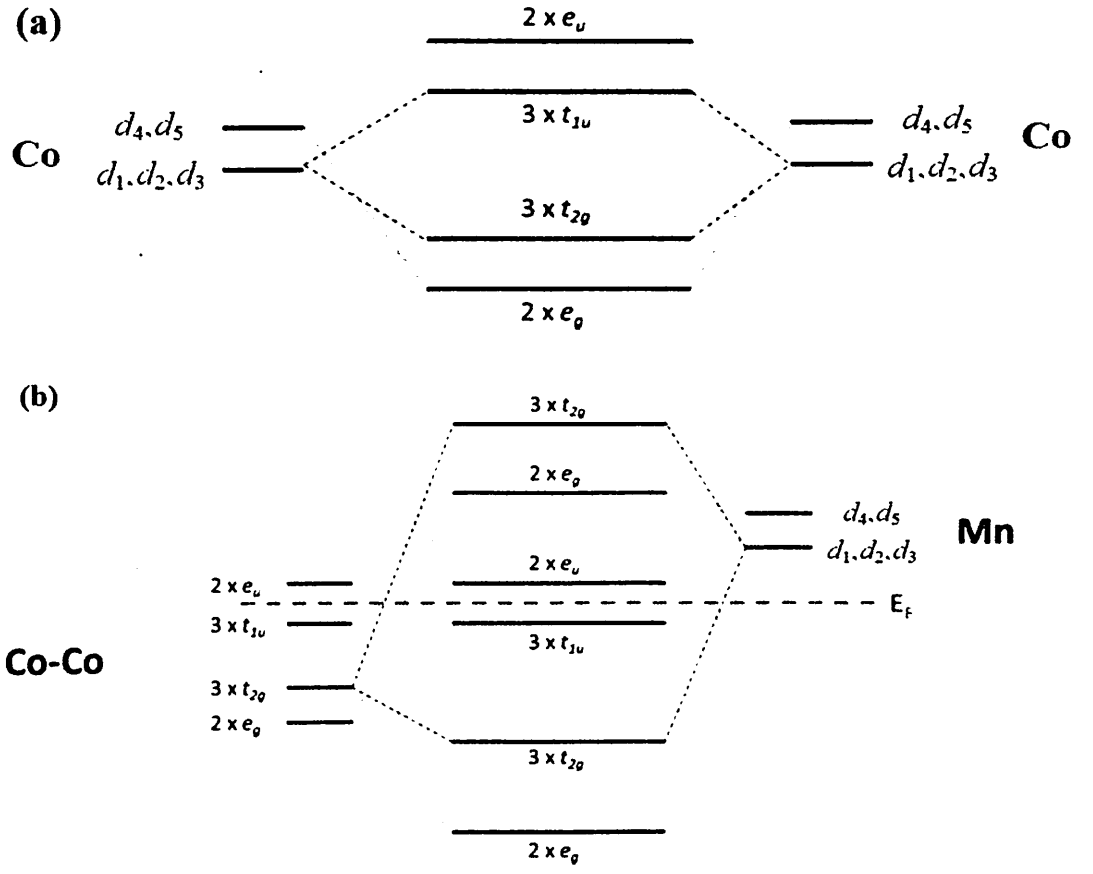

Figure 1.5: Possible hybridization between *d* orbitals of minority states of the compound Co_2MnGe by considering a) Co-Co and b) Mn-(Co-Co) interactions [IGAL02b].

Since these early works, a number of more refined models have appeared. A comprehensive model, which considers interactions between the X, Y and Z sites as well as the *s*, *p* and *d* orbitals of both minority and majority spin states is described in the review by Graf *et al.* [TGRA11a]. Although the origin of the half-metallic properties in

Co-based Heusler alloys is well understood, there are large variations in the reported electronic band structures obtained from these models [IGAL02b, SWUR05a, HCKA06a, ZGER07a, SCHA09a, LGUA10a].

1.4.3 The Slater-Pauling rule

The total magnetic moment (M_t) of half-metallic full Heusler alloys follows the relation,

$$M_t = Z_t - 24 \quad (1.5)$$

where Z_t is the total number of valence electrons [IGAL02b]. Z_t is the sum of the number of spin–up and spin–down electrons, while the total moment M_t is given by the difference, *i.e.*,

$$Z_t = N_\uparrow + N_\downarrow \text{ and } M_t = N_\uparrow - N_\downarrow. \quad (1.6)$$

Since 12 minority bands in a full Heusler alloy are fully occupied {4 in low-lying *s* and *p* bands of the *sp* element and 8 ($2\times e_g$, $3\times t_{2g}$ and $3\times t_{1u}$) in minority Co *d*-bands (cf. Figure 1.5)}, a simple rule of 24 (i.e., $M_t = Z_t - 2\times N_\downarrow$) is obtained for half-metallicity in $L2_1$–type full Heusler alloys. Figure 1.6 (a) illustrates the significance and the applicability of this simple rule for various X_2YZ compounds. This relationship is analogues to the well-known Slater-Pauling behavior of binary transition metal alloys depicted in Figure 1.6 (b) [JKUB84a]. The main difference between the two is, in the case of full Heusler alloys, the minority population is fixed to 12, so that the screening is achieved by filling the majority band, whereas in the case of transition metal alloys, the majority band is either filled with 5 *d*-states or completely empty and charge neutrality is achieved by filling the minority or majority states. Therefore, in the case of transition metal alloys, $M_t = 10 - Z_t$ for the systems on the left side and $M_t = Z_t$ for the systems on the right side of the Slater-Pauling curve.

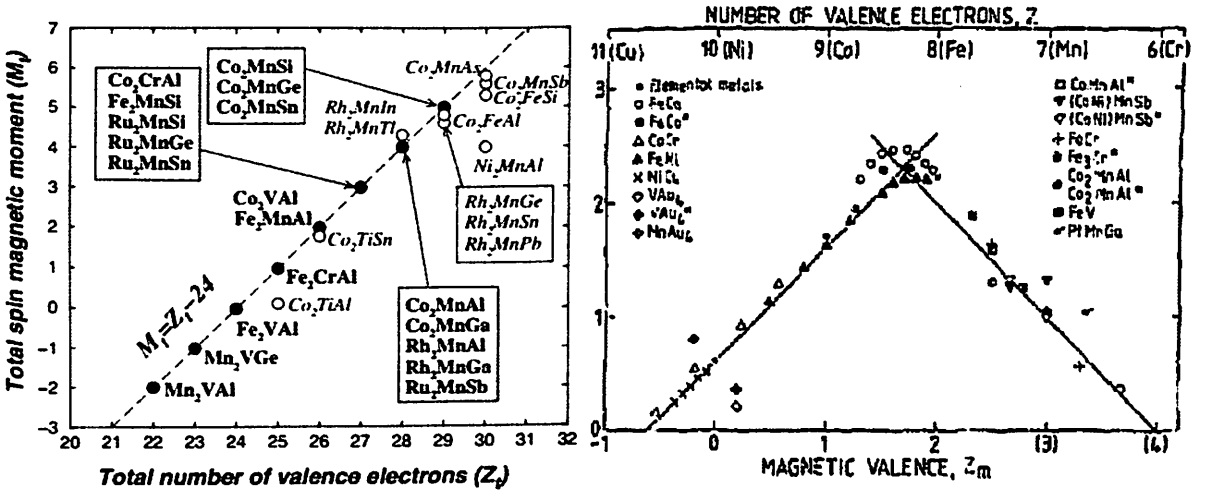

(a) (b)

Figure 1.6: (a) Linear variation of total magnetic moment of full Heusler alloys with total number of valence electrons in various full Heusler compounds [IGAL02b]. (b) Slater-Pauling rule for binary transition metal alloys [JKUB84a].

Based on the M_t versus Z_t plot shown in Figure 1.6(a), full Heusler alloys can be classified into three categories. Those alloys having $Z_t > 24$ will have positive value of M_t. These alloys normally show ferromagnetic behavior. Co_2-based full Heusler alloys fall in this category. These alloys are characterized by a gap in the minority spin band. However, alloys with $Z_t < 24$ (*e.g.*, Mn_2VAl and Mn_2VGa) are ferrimagnetic in nature [KOZD06a]. The half-metallic gap in these alloys is in the majority spin band as opposed to their ferromagnetic counterpart. Fe_2VAl has $Z_t = 24$, and is therefore a semi-metal, *i.e.*, nonmagnetic with a very small DOS at the Fermi level, as observed experimentally [AMAT02a]. So, this simple linear relationship between Considering the large possibilities of elements available for constituting the X_2YZ compounds, M_t and Z_t provides a way to engineer new half-metallic alloys with desired magnetic properties. It

is worthy to point out here that such a Slater-Pauling rule also exists for half-metallic half Heusler compounds, which can be expressed as [IGAL02c],

$$M_t = Z_t - 18 \tag{1.7}$$

Though 100% spin polarization has been theoretically predicted in several Heusler alloy compositions, the same could not be realized experimentally. Moreover, spin polarization of the half-metallic Heusler compounds measured at 4 K decreased drastically at room temperature. Galanakis [IGAL04a] proposed Fermi level engineering by substituting a fourth element in the ternary Heusler compound as a means to overcome this drawback. Prediction of half-metallic character in several quaternary Heusler alloys such as $(XX')_2YZ$, $X_2(YY')Z$, and $X_2Y(ZZ')$ by *ab initio* calculations [IGAL04a] have also been subsequently validated by experimental studies [SVKA06a, BSDC09a, BSDC10a, , BSDC12a].

1.4.4 Determination of half metallicity

To evaluate whether a material is a half-metal or not, different experimental techniques are being used. Measuring intrinsic spin polarizaion (P) requires a spectroscopic technique that can discriminate between the spin-up and spin-down electrons near E_F. Spin-polarized photoemission spectroscopy is technically capable of providing the most direct measurement of P, but it lacks the necessary energy resolution ($\approx$ 1 meV) [RFED85a]. An effective alternative to photoemission is the use of spin-polarized tunneling in a planar junction geometry that allows the electronic spectrum near E_F to be probed with sub-meV energy resolution. Tedrow and Meservey [PMTE94a] pioneered this technique by making a ferromagnet-superconductor (SC) tunnel junction and Zeeman splitting the SC's strongly peaked single-particle excitation spectrum by the application

of a magnetic field. The resulting spectrum of the SC roughly corresponds to two fully spin-polarized peaks (neglecting spin-orbit coupling effects) that can be used to detect P of a current from the ferromagnetic layer. This technique has been successfully employed to estimate P of a number of half-metallic materials. The drawback of the technique is the need of a three layered structure consisting of ferromagnetic and SC layers sandwiched between an oxide layer 10 to 20 Å thickness.

Intrinsic spin polarization can also be measured using point contact Andreev reflection (PCAR) technique. PCAR technique developed by Soulen *et al.* requires no magnetic field and places no special constraints on the sample shape. Andreev reflection is a scattering process where electrical current is converted to super current at the interface between a normal ferromagnetic metal and a superconductor [MJMD95a]. An electron incident from the metal side with energy smaller than the energy gap in the superconductor is converted into a hole which moves backward with respect to the electron. The missing charge 2e propagates as an electron pair into the superconductor. The electron-hole conversion is known as Andreev reflection. Hence, in the PCAR technique, the difference between spin-dependent currents is measured. In a non-magnetic metal, the Andreev process is always allowed, because every energy state in a normal metal has both spin-up and spin-down electrons. However, in a magnetic metal this is no longer true and Andreev reflection is limited by a minority spin population. The uniqueness of this situation was first emphasized by de Jong and Beenakker in 1995 [MJMD95a], when they discussed Andreev reflection at the interface between a half-metal (which is 100% spin polarized) and a conventional SC. Andreev reflection is then

forbidden, as there are no states for a hole to get reflected into, resulting in zero conductance across the interface below the gap.

Kokado *et al.* [SKOK10a] have systematically investigated the sign of the anisotropy magnetoresistance (AMR) of ferromagnetic materials. It has been found that for half-metallic ferromagnets, the dominant scattering is $s\uparrow \rightarrow d\uparrow$ or $s\downarrow \rightarrow d\downarrow$, which causes the sign of the AMR to be negative [APMA85a, MZIE00a]. Subsequently, Yang *et al.* [FJYA12a] measured the AMR ratio in Heusler $Co_2(Fe,Mn)Si$ epitaxial films and demonstrated that it can be used to identify a half-metal without the need for any microfabricated device structure.

Rhodes-Wohlfarth (R-W) ratio (p_c/p_s), where where p_s is the saturation magnetic moment expressed in units of μ_B and the factor p_c is the effective magnetic moment per magnetic atom), can also indicate half-metallicity in a ferromagnetic material. p_c/p_s is expected to be unity for local moment ferromagnets and larger than unity for itinerant ferromagnets. However, the R-W ratio was found to be less than unity for half-Heusler CoMnSb, NiMnSb and PtMnSb alloys [MJOT89a, NPDU07a]. To correlate the R-W ratio with the nature of magnetic interaction in half Heusler alloys, Otto et al [MJOT89a] used a simple molecular field model which takes into account both local moments and spin polarized itinerant electrons. According to the model, a strong interaction between local moments and spin polarized itinerant electrons makes the R-W ratio to become less than unity. Experimentally, NiMnSb has been shown to be a half-metal [KEHM90a, RJSO98a] and so this prediction of $p_c/p_s < 1$ for half-metallic NiMnSb is considered as a characteristic of half-metallic ferromagnets [NPDU07a].

Ab initio calculations provide a powerful way to predict and verify half-metallic nature of Heusler alloys. Band structure calculation on Heusler alloys was by Ishida *et al.* [SISH78a, SISH80a] in the early 1980s. Apart from the discovery of half-metallicity in NiMnSb and Co_2MnSi, large numbers of other Heusler alloys have been identified to be half-metallic by *ab initio* calculations. This technique permits one to explore the effects of atomic substitutions for X, Y or Z elements and different types of atomic disorders on half metallic nature of Heusler alloys by suitably manipulating the unit cell representing the alloy in question.

1.5 EFFECT OF STRUCTURAL DISORDER ON FULL HEUSLER ALLOYS

Though full Heusler alloys with highly ordered (stable) $L2_1$ structure is desirable, it not always possible to fully stabilize the $L2_1$ structure in all the alloys. As discussed in section 1.2, different antisite disorders can be present in Heusler alloys. Understanding the influence of these disorders on magnetic and half-metallic properties of these alloys is very important from both basic science and application points of view.

1.5.1 On magnetic properties

Any deviation from the 2:1:1 full Heusler stoichiometry or changes in the atomic arrangement in the full Heusler structure can have significant effect on the magnetic properties of the compound. Magnetism in Heusler alloys is the result of the complex hybridization of the atomic orbitals in the compound. As a direct consequence of this, any atomic swapping changes this local hybridization and hence the band structure of the compound. Because the magnetic moments in Heusler compounds come from spin moments of valance electrons localized in the d orbitals of the X and Y atoms, any

change in the interatomic spacing also has a large effect on this localization. In other words, any changes in the lattice constant in these materials can also have a dramatic effect on the magnetic properties of these alloys. Due to the large variety of Heusler compounds, it is impossible to describe how disorder affects all Heusler alloys. Therefore, Co_2FeSi is taken as an example to discuss the effect of disorder on full Heusler alloys. The most probable atomic swaps that can result in disorder in the $L2_1$ structure are Fe-Si (B2 disorder), Co-Fe (DO_3 disorder) and Co-Fe-Si (A2 disorder). The fully ordered $L2_1$ unit cell should result in a total moment of $6\mu_B$ [HCKA06a]. The effect of these atomic swaps has been calculated by Li *et al.* [LGUA10a] using density functional theory (DFT). Their model predicts that 6.25% Co-Fe swaps reduce the moment of Co_2FeSi to 5.5 μ_B. Surprisingly, introduction of 12.5% A2 disorder increases the moment to $6.15\mu_B$ [ZGER07a]. However, Fe-Si swaps (up to 10%), which induces B2 disorder, did not change the moment from $6\mu_B$. This is however in contradiction to a number of experimental studies which show a decrease in magnetic moment with increasing B2 ordering [SWUR05a, YTAK08a, MOOG09a]. This is most likely due to the effect of widespread disordered regions in the materials and not to just atomic swapping localized to the unit cell.

1.5.2 On half-metallicity

The effect of disorder on the half-metallic nature of Heusler alloys is quite considerable. This is due to the sensitivity of the band gap in minority spin states to changes in the hybridization of atomic orbitals due to changes in atomic positions [VKSE10a, FJYA13a]. It is extremely difficult to quantify and discriminate the effects of different types of disorder from experimental data as they are often randomly distributed

throughout a system, as well as being specific to a particular experiment. A number of atomic swap type disorders in Co_2FeSi have been considered in the literature to provide us with a reasonable understanding. Of these, Fe-Si (B2) and Co-Fe-Si (A2) disorders are most widely studied with Co-Fe (DO_3) disorder receiving much less attention [ZGER07a, LGUA10a]. Unfortunately, the models used to calculate the extent of disorder are often limited by the size of the initial unit cell used. For example, one on the most extensive studies on the effect of disorder in Co_2FeSi-based alloys by Gercsi and Hono [ZGER07a] used a 16 atom unit cell, which limits the minimum amount of disorder that could be modelled to 25% for B2 type and 12.5% for the A2 and DO_3 types. However, this effort was sufficient to acquire some basic understanding of how these disorders affect the half-metallicity of this compound.

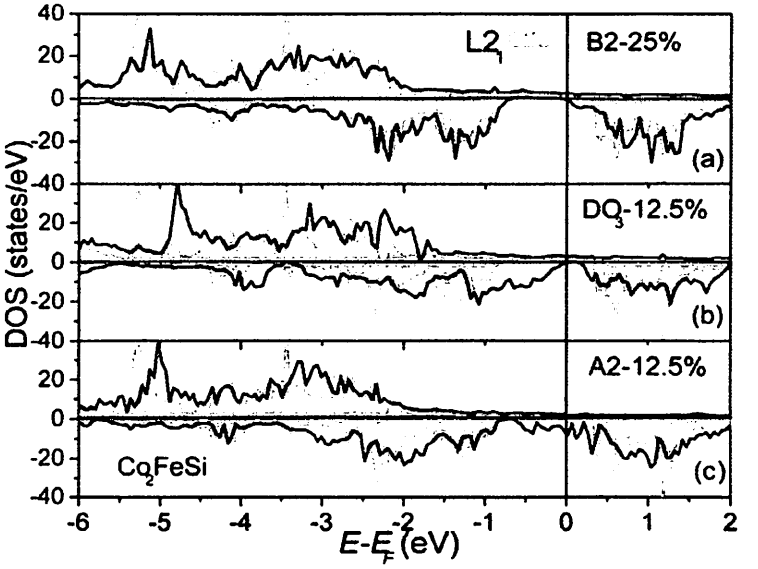

Figure 1.7: Variation in the spin dependent density of states of Co_2FeSi with different amounts of a) B2, b) DO_3 and c) A2 disorders. The $L2_1$ spin density of states is shown in grey background as a reference [ZGER07a].

As shown in Figure 1.7, different disorders affect the DOS in different ways. The B2 type disorder is seen to retain the minority state band gap and hence the half-metallic conduction properties even at 25% disorder. This retention of the band gap despite B2-type disorder is because of the lack of disorder in Co-Co symmetry in the lattice. It has been shown that the band gap is constructed by 3d states localized at Co atoms [YMIU04a]. Therefore, if these states are not altered by the atomic disorder, the half-metallic electronic properties should remain unaltered. For the DO_3 disorder, the band gap is reduced and moves relative to E_F, producing a small but finite number of states for the minority channel at E_F. However with A2 disorder, the band gap is completely destroyed.

1.6 FULL HEUSLER ALLOYS BASED MAGNETORESISTIVE DEVICES

Since the discovery of half-metallic ferromagnetism in a number of full Heusler alloys, several spintronic devices have been fabricated with them as electrode layers. Co-based Heusler alloys are of particular interest due to their high magnetic moment and high Curie temperature, as well as their theoretically predicted 100% spin polarization. A brief discussion on Heusler alloy based giant magnetoresistance (GMR), tunnel magnetoresistance (TMR) and lateral spin valve (LSV) devices is given below.

1.6.1 GMR devices

Fully epitaxial current-perpendicular-to-plane (CPP) giant magnetoresistance (GMR) devices with half-metallic Co_2MnSi (CMS) as electrodes and a Ag spacer, annealed at 550 °C showed the magneto-resistance ratio (ΔMR) of 36.4% and 67.2% at 300 K and 110 K, respectively [YSAK10a]. CMS layers grown at 250 °C showed ΔMR of 33% at

300 K [YSAK13a]. CPP-GMR devices with a $Co_2Fe_{0.4}Mn_{0.6}Si$/Ag/$Co_2Fe_{0.4}Mn_{0.6}Si$ structure exhibited ΔMR of 50.1% for 3 nm thick upper layer and 74.8% ΔMR for 10 nm thick upper layer [JSAT11a]. Usage of Co_2Fe(Ga0.5Ge0.5) (CFGG) as ferromagnetic layers with a thickness 12 nm in CPP-GMR pseudo-spin valve device has led to ΔMR exceeding 41.7% at 300 K and 129.1% at 10 K [YKTA11a]. With 10 nm thick CFGG layers room temperature ΔMR increased to 45.8% [HSGO13a]. For Co_2Mn(Ga0.25Ge0.75) and Co2FeAl0.5Si0.5 ferromagnetic layers, ΔMR of 40.2% and 34% were obtained at 300 K, respectively [YKTA13a, TMNA10a]. CPP–GMR of pseudo-spin valves with polycrystalline $Co_2Fe(Al_{0.5}Si_{0.5})$ and $Co_2Fe(Ga_{0.5}Ge_{0.5})$ alloy films exhibited relatively large CPP–GMR values of ΔRA up to 4 mΩ -μm^2 and ΔR/R up to 10% with 5 nm thick films [TMNA13a].

1.6.2 TMR devices

An out-of-plane tunnel magnetoresistance (TMR) ratio of 53% at room temperature was reported in Co_2FeAl/MgO/$Co_{20}Fe_{60}B_{20}$ perpendicular magnetic tunnel junction (MTJ). By inserting a 0.1-nm-thick Fe ($Co_{50}Fe_{50}$) layer between the MgO and $Co_{20}Fe_{60}B_{20}$ layers, the TMR ratio was significantly enhanced to 91% (82%) due to improved interface [ZWEN12a]. TMR ratio of 104% at 300 K was obtained for Co_2FeSi/BaO/Fe MTJ [JROG12a]. TMR ratios of 262% at 15 K and 159% at 300 K were observed for $Fe_{1.75}Co_{1.25}Si$ electrodes and MgO barrier [CSTE13a]. TMR ratios up to 228% (398%) at 300 K (5 K) in a perfectly lattice-matched MTJ with a B2-ordered Co_2FeAl electrode and a cation-disorder spinel Mg-Al-O barrier MTJ was obtained. The TMR ratio further increased up to 280% (451%) at RT (5 K) by inserting a 1-nm-thick CoFe layer between

the Co_2FeAl and Mg-Al-O barrier [TSCH14a]. Giant TMR ratios of up to 1995% at 4.2 K and up to 354% at 290 K were obtained for epitaxial CMS/MgO/CMS MTJs featuring a reduced lattice mismatch in the MTJ tri-layer by introducing a thin CMS lower electrode deposited over a $Co_{50}Fe_{50}$ buffer layer [HLIU12a]. The ratio increased up to 2610% at 4.2 K and 429% at 290 K for MTJs with $Co_2Mn_{1.24}Fe_{0.16}Si_{0.84}$ electrodes [HLIU15a].

1.6.3 LSV devices

The first report on lateral spin valve (LSV) device by Jedema *et al.* [FJJE01a] using $Ni_{80}Fe_{20}$ showed spin signal (ΔR_s) value of 0.1 mΩ which increased to 50 mΩ at 300 K by inserting a thin MgO layer between ferromagnetic and non-magnetic wires [YFUK11a]. Large ΔR_s of 12.8 mΩ was obtained at 300 K without the MgO layer in the all-metallic LSV device using CFGG [YKTA12a]. The reasons of the large ΔR_s were attributed to the high spin polarization of CFGG and the resulting small spin absorption. For LSV devices with Co_2FeSi (CFS) or Fe_3Si (FS) electrodes, ΔR_s of 11.2 mΩ was obtained at the CFS-Cu-CFS side and 6.8 mΩ for the (FS/CFS)-Cu-(FS/CFS) side [SOKI13a]. ΔR_s of 4.2 mΩ was obtained for CMS/Ag based LSV devices [FYAN13a]. Micro fabrication of CFGG based LSV device yielded ΔR_s of 11.75mΩ [IKHT14a].

1.7. MOTIVATION AND SCOPE OF THE PRESENT WORK

The above review of the literature shows the current interest and technological potential of full Heusler alloys. Although theoretical studies have predicted several full Heusler alloys with 100% spin polarization, practical realization of the same has not yet been achieved. Therefore along with the search of new Heusler alloys, various factors affecting

the spin polarization have to be studied. After Co_2MnSi, Co_2FeSi is one of the most extensively studied Heusler compounds. Co_2-based quaternary alloys have shown excellent magnetoresistive properties as discussed in the previous section. So, it would be worthwhile to explore the influence Ge and Ga substitution for Si in Co_2FeSi.

Spin valves using Heusler alloy based electrode layers invariably use an Ir-Mn antiferromagnetic layer to pin one of the ferromagnetic layers [KNIK09a, TMNA12a]. Ru_2YZ alloys exhibit antiferromagnetism near room temperature [SMIZ09a, TKAN06a, SNMI85a, ASZY89a]. $Ru_2Y(Z_{1-x}Z'_x)$ and $(Ru_{1-x}X'_x)_2YZ$ alloys offer a means for obtaining both ferromagnetic and antiferromagnetic materials in the same quaternary system by properly choosing the fourth element (X′ or Z′) and its concentration. Antiferromagnetic Heusler alloys with high T_N could lead to the realization of spin valves entirely made up of full Heusler alloy layers with superior interfacial properties and hence better performance. An understanding of the crystallographic and magnetic properties of $Ru_2Y(Z_{1-x}Z'_x)$ and $(Ru_{1-x}X'_x)_2YZ$ alloys is the first step in this direction.

Half-metallic materials exhibiting high spin polarization and no stray magnetic fields are in demand for fabricating high density information storage and vertical recording devices [RADE91a, HVAN95a]. Zero net moment half-metals have been proposed as the basis for a new class of superconductor called single-spin superconductor that has only one superconducting spin channel [WEPI96a]. High perpendicular magnetic anisotropy exhibited by thin films of ferrimagnetic $Mn_{2.5}Ga$ has also opened up the possibility of realizing spin transfer torque based devices [FWU09a]. *Ab initio* calculations have demonstrated that progressively substituting for Mn with Co in ferrimagnetic $Mn_2VAl(Si)$ compound can lead to zero moment or a fully compensated

ferrimagnet (FCF) [IGAL07a]. Search for FCF in Mn_3Ga and substituted $Mn_{3-x}Ga$ alloys [HNII96a, BBAL07b, HKUR11a] has yielded ferrimagnetic thin films with low saturation magnetization of $0.65\mu_B$ and spin polarization of 58%. However, these alloys exhibit tetragonal DO_{22} structure instead of the stable $L2_1$ structure of a full Heusler alloy. Practical difficulties in obtaining oxygen free Heusler alloys with high Mn content and maintaining the nominal stoichiometry have been the main deterrents in preparing these alloys as observed by very few experimental reports on bulk and thin film.

In an attempt to address some of these important issues associated with the development of full Heusler alloy based spintronic materials, this thesis work explores the structural, magnetic and spintronic properties of following series of alloys:

1) $Co_2FeGe_{1-x}Si_x$ and $Co_2FeGa_{1-x}Si_x$ $(0 \leq x \leq 1)$,

2) $Ru_2FeSi_{1-x}Ge_x$ and $(Ru_{1-x}Co_x)_2FeSi$ $(0 \leq x \leq 1)$, and

3) $(Mn_{1-x}Co_x)_2VAl$ and $(Mn_{1-x}Co_x)_2VGa$ $(0 \leq x \leq 0.5)$.

Chapter 2

EXPERIMENTAL AND COMPUTAIONAL METHODOLOGIES

This chapter discusses the experimental and computational techniques used in the investigations, including sample preparation and methodologies adopted. The principle and theory behind the experiments performed, the experimental set up used and the measurement methodology followed for determination of the physical properties are also discussed here.

2.1. PREPARATION AND PROCESSING OF SAMPLES

2.1.1. Preparation of alloy ingots

In the present work, all the alloy ingots were prepared by arc melting constituent elements. A commercial arc melting furnace (Make: Vacuum Techniques, India) was used for preparing the alloy ingots. Schematic diagram of an arc melting furnace is presented in Figure 2.1 [a high current (200 A) dc power supply used as electrical source is not shown here].

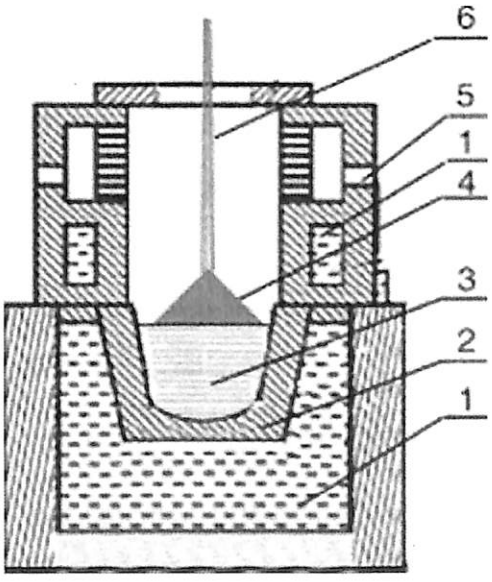

Figure 2.1: Schematic diagram of water-cooled copper-hearth electric arc melting furnace. Labels denote: (1) circulating water to cool the hearth, (2) copper hearth (cathode), (3) compacted metal blend, (4) electric arc struck between the electrodes (5) gas inlet valve (6) water cooled flexible electrode with tungsten tip (anode) [QDQI06a].

High purity (≥ 99.99%) elemental pieces as per the requirement of the target composition were weighed in a calibrated electronic balance of 0.01 mg resolution. The total charge weighing about 5 g was placed in the water-cooled copper hearth of the arc furnace and the chamber was pumped down to ~10^{-5} Torr (10^{-3} Pa) using a combination of diffusion and rotary pumps. The chamber was then purged with high purity argon gas to remove traces of oxidizing atmospheric gases and finally filled with argon gas. DC arc was then struck between a high purity tungsten anode and the copper hearth cathode and the elemental pieces were melted in the heat generated by the arc carefully so as to ensure minimal loss of material. The cast ingot was then flipped around and re-melted several times to ensure complete melting and mixing of the constituent elements to yield a homogeneous alloy ingot. The ingot obtained after melting was molded (re-melted) in a dismountable copper cylinder kept on the water cooled hearth in order to obtain a 10 mm diameter cylindrical sample. Since loss of highly volatile and low melting point elements such as Mn cannot be completely prevented, excess (up to 2 at.%) amount of such volatile elements were added to achieve the desired net composition in the alloy ingot.

2.1.2. Processing of alloy ingots

As-prepared samples were processed under different conditions depending upon requirements. The different processing procedures adopted are briefly described below: The as-cast ingots had to be further homogenized and then annealed at appropriate temperature in order to obtain highly ordered alloys with consistent and reproducible properties. Metallic samples cannot be heat treated in air since they would oxidize. So, the as-prepared alloy ingots were taken separately in fused silica ampoules, pumped down to 10^{-3} Pa using an oil diffusion with rotary pump combination (Make: Vacuum Techniques, India) and then sealed with a neutral oxygen-liquid petroleum gas flame. The vacuum-sealed ampoules

containing the samples were placed inside a raising hearth furnace (Make: OKAY, India, Model: 70T-4), and heated to a homogenizing temperature of ~1200 K. The well homogenized ingot was annealed at ~ 1073 K followed by quenching in ice water.

Arc melted cylindrical ingots were cut into small pieces using a diamond saw (Make: Buehler, Model: Isomet 2000) and cleaned with acetone in an ultrasonic bath. A part of the annealed ingot was crushed into fine powder, heat treated again at 1073 K followed by quenching and used for structural studies.

2.2. STRUCTURAL CHARACTERIZATION AND COMPOSITION ANALYSIS

2.2.1. Powder X-ray diffraction

Two powder X-ray diffractometers *viz.* Seifert XRD 3003 T/T with sealed X-ray tube (shown in Figure 2.2a) and a rotating anode based Rigaku TTRAX III 18 kW were used for structural characterization of the processed alloy powders, depending upon their availability. X-ray diffraction (XRD) technique allows identification of crystalline phases present in the alloys, degree of crystalline order in the alloy and provides other structural information. A theta-theta (θ-θ) goniometer depicted in Figure 2.2b was used in the reflection (Bragg-Brentano) geometry [BDCU01a] for collecting the XRD data.

A poly(methyl methacrylate) (PMMA) plate with a square depression of dimensions 25 mm (L) × 25 mm (B) × 0.5 (W) $(mm)^3$ coated with a thin layer of high vacuum grease was used as sample holder for XRD measurements. The sample in fine powder form was evenly spread over the square depression on the PMMA sample holder. The holder was mounted on the goniometer for recording the XRD patterns. Diffraction of X-rays occurs through constructive interference of X-rays scattered from atoms of a set of parallel planes in crystal lattice at a particular angular positions of the incident wave known as Bragg angles

[BDCU01a]. A schematic representation of the XRD phenomenon from a crystal and the geometry employed to record the powder XRD pattern are shown in Figure 2.3.

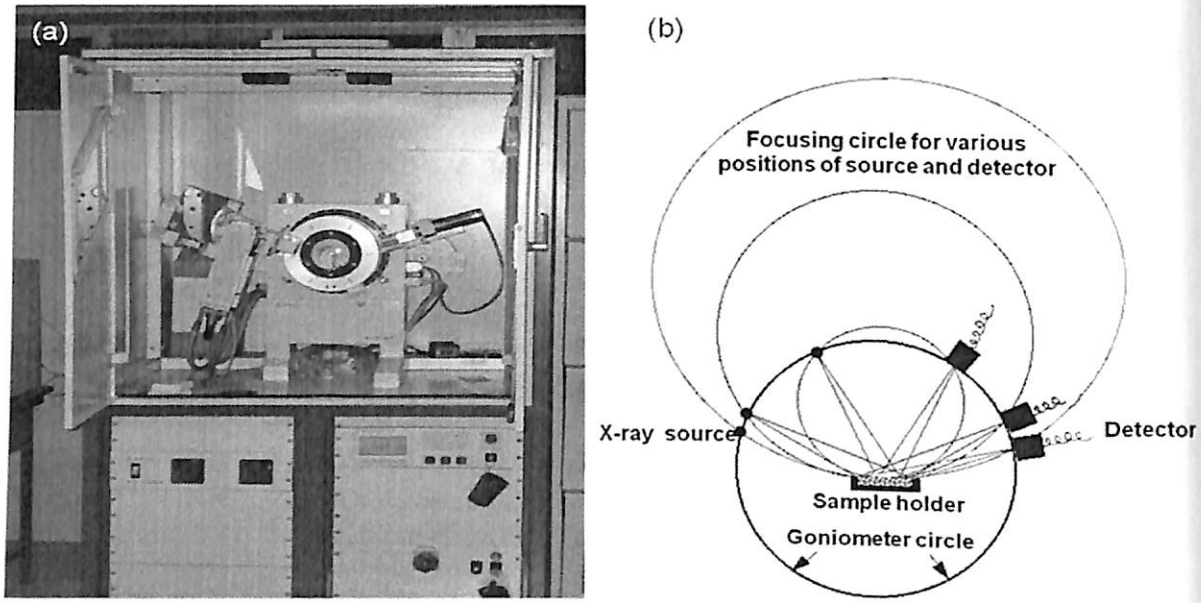

Figure 2.2: (a) Photograph of Seifert XRD 3003 T/T powder X-ray diffractometer, and (b) Bragg-Brentano diffraction geometry of a powder X-ray diffractometer.

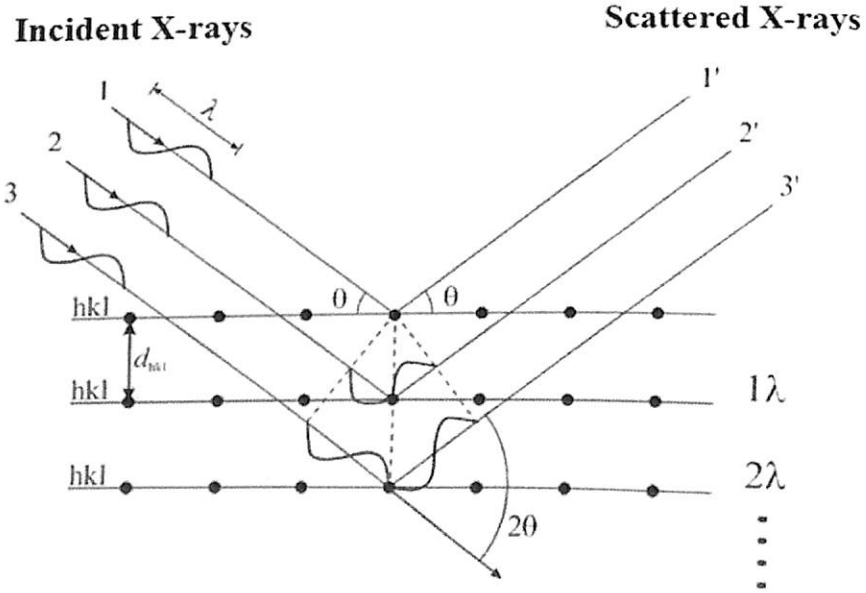

Figure 2.3: Schematic ray diagram of diffraction of X-rays by a crystal.

The condition for obtaining constructive interference from a set of parallel planes is specified by the Bragg's law [BDCU01a],

$$2d_{\mathrm{hkl}} \sin\theta = n\lambda \qquad (2.1)$$

where d_{hkl} is the inter planer spacing of a set of planes with Miller indices (h k l), θ is the glancing angle, λ is the wavelength of the X-ray and n is the order of diffraction. A specific series of these angles at which constructive reflections are observed in a 2θ scan can be used to determine the Miller indices of crystal planes causing these reflections and the crystal structure can be identified from the systematic behavior of these indices [BDCU01a]. A standard polycrystalline silicon (Si) sample was used for calibrating the instrument. A typical XRD pattern recorded for the standard polycrystalline Si sample is shown in Figure 2.4.

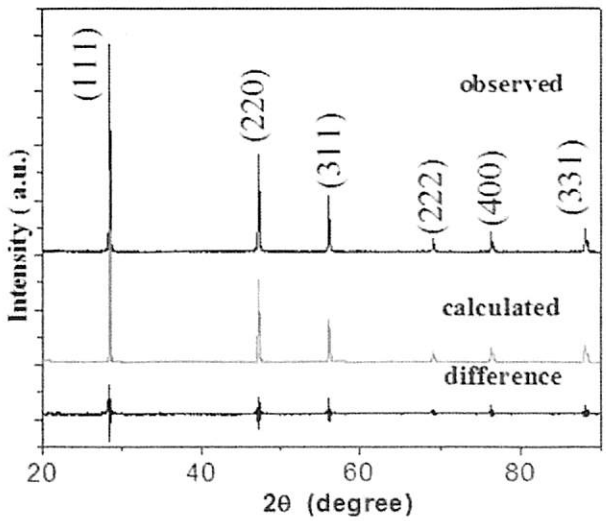

Figure 2.4: XRD pattern of standard polycrystalline Si sample. Calculated and difference data correspond to least squares fitting performed on the observed data are also shown.

As discussed in section 1.2 of this thesis, Bragg reflections with non-zero structure factor for a fully ordered Heusler alloy (X_2YZ) with $L2_1$ structure are obtained only when all

indices are either even or odd. The structure factor of the first three reflections can be expressed as,

$$F(111) = 4(f_y - f_z),\quad F(200) = 4[2f_x - (f_y + f_z),\quad F(220) = 4[2f_x + f_y + f_z] \qquad (2.2)$$

where f_x, f_y and f_z are average scattering amplitudes of the respective sub-lattices. Therefore, two very common types of disorder in $L2_1$ structure, *viz.*, B2 (intermixing of Y and Z atoms) and A2 (intermixing of all X, Y and Z atoms) can be identified from the absence of (111) and (200) peaks, respectively. The degree of atomic ordering can be estimated from the ratio of the intensity (I_{hkl}) of the super-lattice reflections from (111) and (200) planes using the relations,

$$S = ((I_{200}/I_{220})_E/(I_{200}/I_{220})_T)^{1/2} \qquad (2.3)$$

$$(1-2\alpha)S = ((I_{111}/I_{220})_E/(I_{111}/I_{220})_T)^{1/2} \qquad (2.4)$$

where the suffixes E and T denote data obtained experimentally and data theoretically generated for the $L2_1$ unit cell. According to Webster and Ziebeck [BSDC09a, PJWE69a, PJWE73a], $S = 1$ and $\alpha = 0$ signify perfect $L2_1$ ordering in a full Heusler alloy. Typical XRD patterns of alloys with $L2_1$ order as well as with B2 and A2 disorders are shown in Figure 2.5.

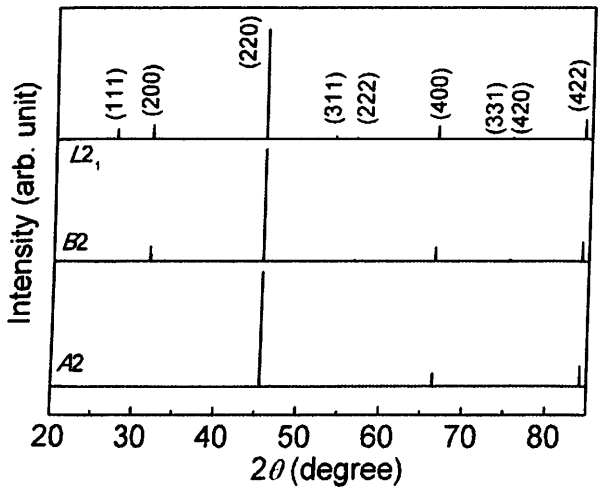

Figure 2.5: Typical XRD patterns for ordered $L2_1$ structure and with B2 and A2 disorder.

Rietveld refinement technique has been employed to refine the crystal structure and extract crystallographic parameters from recorded powder XRD patterns. Fullprof 2.00, a public domain software was used for Rietveld refinement [HMRI67a, HMRI69a, DLOU98a] of XRD patterns of the processed alloys. Two versions of source codes of Fullprof are available to users. The first corresponds to a program written in FORTRAN 77 which can be used in multiple platforms. The second version developed from the previous one is coded in FORTRAN 95. Input files for this program should carry the extensions '*.pcr' and '*. dat'. The *.pcr file contains the title, type of analysis (X-ray, neutron or profile fitting), profile function used for fitting, number of phase present, wave length of the beam used for the collection of data along with the step size and 2θ range, number of iteration cycles, number of refined parameter and other crystallographic data. The *.dat file contains the intensity [counts per second (cps)] data which are recorded by the scintillation detector as a function of 2θ. Optional input files such as '*.bac' and '*.irf' can be used for specifying the background at each step of the scattering variable, and incorporating the instrumental resolution function, respectively. The two main output files are '*.out' and '*.sum' that contain all control variables and refined parameters. Another important output file is '*.prf' which contains observed and calculated profiles that are automatically used by a graphical interface program called *WinPLOTR*. This program generates three plots, *viz.*, the calculated pattern from the input file *.pcr, the observed pattern from *.dat and their differences to graphically show the goodness of the fit. Figure 2.4 shows one such typical graphical output of the Fullprof program. The control of the refined parameter is achieved by using a flag in the form of a code word. The sequences for refinement involves setting / optimizing the following parameters: (1) scale factor, (2) zero point of detector, first two background parameters and lattice constant(s), (3) overall Debye-Waller factor, (4) peak shape and asymmetry

parameters, (5) atom occupancies, (6) individual isotropic thermal parameters, and (7) additional background parameters.

The quality of refinements are known based on the values of reliability factors such as R_p, R_{wp}, R_{exp}, R_{Bragg}, χ^2 and R_F that are defined as follows [ANIN01a]:

Profile factor,
$$R_p = 100 \frac{\sum_{i=1,n} |y_i - y_{c,i}|}{\sum_{i=1,n} y_i} \tag{2.5}$$

Here, 'y_i' is the observed point (experimental), '$y_{c,i}$' is the calculated point and n represents the number of data points.

Weighted profile factor,
$$R_{wp} = 100 \left(\frac{\sum_{i=1,n} \omega_i |y_i - y_{c,i}|^2}{\sum_{i=1,n} \omega_i y_i^2} \right)^{1/2} \tag{2.6}$$

Here, $\omega_i = \frac{1}{\sigma_i^2}$; σ_i^2 is the variance of the observation y_i.

Expected weight factor,
$$R_{exp} = 100 \left(\frac{n-p}{\sum_i \omega_i y_i^2} \right)^{1/2} \tag{2.7}$$

Here $(n - p)$ is the number of degrees of freedom and 'p' is the number of refine parameters.

Reduced chi-square,
$$\chi^2 = \left(\frac{R_{wp}}{R_{exp}} \right)^2 \tag{2.8}$$

Bragg factor,
$$R_B = 100 \left(\frac{\sum_h |I_{obs,h} - I_{cal,h}|}{\sum_h |I_{obs,h}|} \right)^{1/2} \tag{2.9}$$

Here, 'h' levels the Bragg's reflections. $I_{obs,h}$ are the observed integrated intensities and $I_{cal,h}$ are the calculated intensities.

The crystallographic R_F factor, $$R_F = 100\left(\frac{\sum_h \left|F_{obs,h} - F_{cal,h}\right|}{\sum_h \left|F_{obs,h}\right|}\right) \quad (2.10)$$

Here, $F_{obs,h}$ and $F_{cal,h}$ are the observed and calculated structural factors, respectively. The refinement procedure involves careful preparation of the input files and re-iteratively performing the refinement until a good graphical fit (difference plot with minimal undulation) along with least values of χ^2, R_B and R_F are obtained for the measured XRD pattern. The Bragg's factor R_B should be zero for an ideally best fit. However, R_B values less than 10 are considered to represent acceptably good fit to the data.

2.2.2. Scanning electron microscope

Scanning Electron Microscope (SEM, Leo 1430VP) with Energy Dispersive Spectroscopy (EDS) attachment (Oxford) was used to study the surface morphology of the alloys and to determine the chemical composition of the alloys. SEM is a powerful microscope that uses electrons rather than light to form an image of objects such as fractured metal components, foreign particles, residues, polymers, electronic components, biological samples, and countless others. The shorter wavelength of electrons permits image magnifications of up to 100,000X as compared to about 2,000X for conventional light microscopy. A SEM also provides a greater depth of field than a light microscope, allowing complex, three-dimensional objects to remain sharp and in focus. Hence, details that cannot be resolved by light microscopy can be observed under a SEM [SCAN12a].

A schematic representation and a photographic view of a SEM are shown in Figure 2.6(a) and 2.6(b), respectively. Thermionically emitted electrons from a tungsten filament are accelerated towards an anode in a potential difference typically of the order of 10-20 keV and focused by condenser lenses on a spot volume of the specimen, resulting in the transfer of

energy to the spot. These bombarding electrons, also referred to as primary electrons, dislodge electrons from the specimen itself. The dislodged electrons, also known as secondary electrons, are attracted and collected by a positively biased grid or detector, and then translated into a signal. To produce the SEM image, the electron beam is swept across the area being inspected, producing many such signals. These signals are then amplified, analyzed, and translated into images of the topography being inspected. Finally, the image is displayed on a screen.

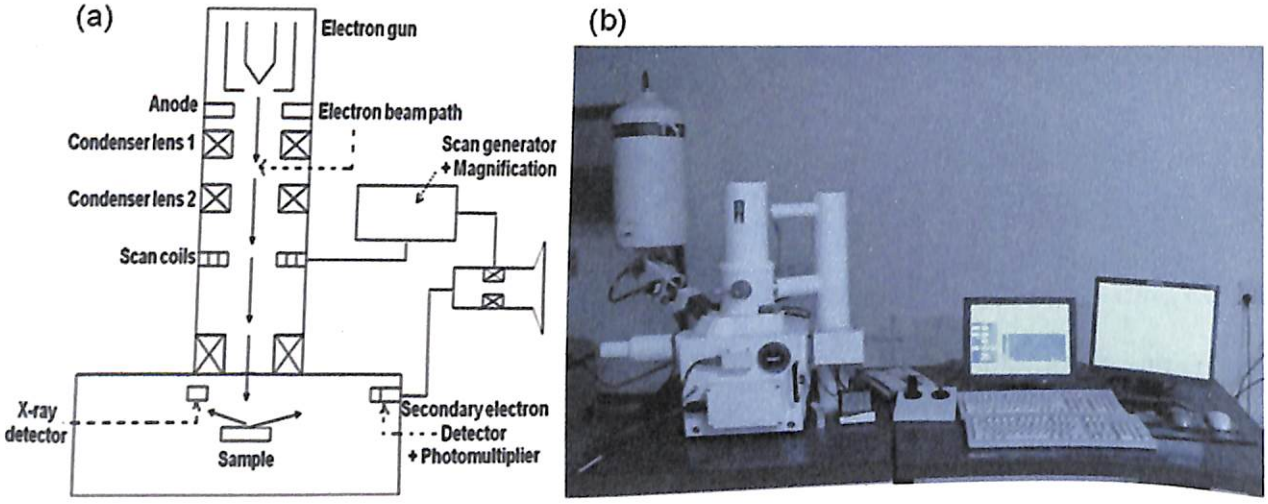

Figure 2.6: (a) Schematic view and (b) photograph of Leo 1430VP SEM equipped with EDS.

The energy of the primary electrons determines the quantity of secondary electrons collected during inspection. The emission of secondary electrons from the specimen increases as the energy of the primary electron beam increases, until a certain limit is reached. Beyond this limit, the collected secondary electrons diminish as the energy of the primary beam is increased, because the primary beam is already activating electrons deep below the surface of the specimen. Electrons coming from such depths usually recombine before reaching the surface for emission.

The most common imaging mode relies on detection of the lowest portion of the emitted energy distribution. Their very low energy means they originate from a subsurface depth of no larger than several angstroms. The signal is captured by a detector consisting of a scintillator-photomultiplier combination, and the output serves to modulate the intensity of cathode ray tube, which is rastered in synchronization with the raster-scanned primary beam.

Apart from secondary electrons, the primary electron beam results in the emission of backscattered (or reflected) electrons from the specimen. Backscattered electrons possess more energy than secondary electrons and have a definite direction. As such, they cannot be collected by a secondary electron detector, unless the detector is directly in their path of travel. All emissions above 50 eV are considered to be backscattered electrons.

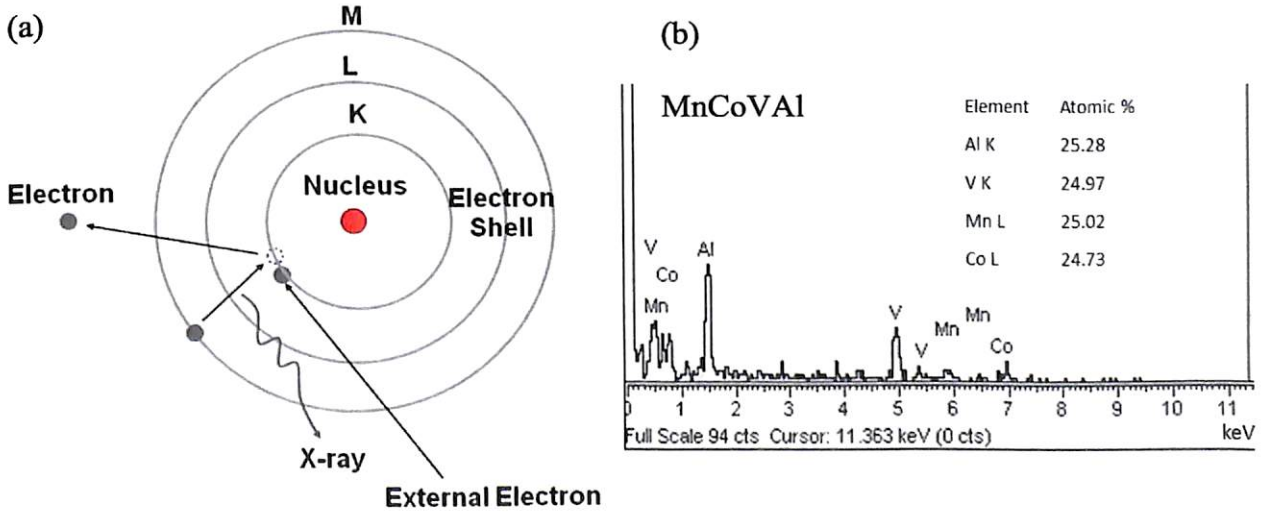

Figure 2.7: (a) X-ray emission by an atom excited by a high energy electron [YLEN08a].

(b) Typical EDS spectrum of a specimen (MnCoVAl) and its atomic constitution.

Backscattered electron imaging is useful in distinguishing one material from another, since the yield of the collected backscattered electrons increases monotonically with the specimen's atomic number Z ($\propto 0.05Z^{1/2}$). Backscatter imaging can distinguish elements with

atomic number differences of at least 3, *i.e.* materials with atomic number differences of at least 3 would appear with good contrast on the image.

A SEM may be equipped with an EDS (*a.k.a.* EDX or EDAX) system to enable composition analysis on specimen. EDS analysis is useful in identifying materials and contaminants, as well as estimating their relative concentrations on the surface of the specimen. During EDS analysis, an electron bean collides with the electrons in the atoms of the specimen, knocking some of them off in the process. A position vacated by an ejected inner shell electron is eventually occupied by a higher-energy electron from an outer shell. To enable this, the transferring outer electron must give up some of its energy by emitting X-rays. This process is schematically shown in Figure 2.7(a). The amount of energy released by the transferring electron depends on which shell it is transferring from, as well as which shell it is transferring to. Furthermore, the atom of every element releases X-rays with unique amounts of energy during the transferring process. Thus, the energy spectrum of X-rays released by a specimen during electron beam bombardment is used to identity of the type and amount of elements present. In the present work, an EDS (Oxford) attached to a scanning electron microscope (SEM, Leo 1430 VP) was used. The alloy specimen was placed on carbon coated tape and then gold coated to make it electrically conducting. Figure 2.7(b) shows a typical EDS spectrum of a specimen (MnCoVAl) and the elemental distribution.

2.3. MAGNETIC PROPERTY CHARACTERIZATION

2.3.1. Vibrating sample magnetometer

Vibrating Sample Magnetometer (VSM, Lakeshore Model 7410) has been used for performing magnetic measurements on the alloy samples. VSM [JSVO04a, CHOR06a] measures the net dipole moment when the material is exposed to a magnetic field. The magnetic moment of the sample can be obtained either as a function of field (*M-H* curve) or

as a function of temperature (*M-T* curve) using this instrument. Figure 2.8a and Figure 2.8b depict a schematic diagram and a snap shot of the Lakeshore Model 7410 VSM, respectively.

The VSM operates on the principle of Faraday's law of induction, which tells us that a changing magnetic flux will produce an electric field [DJGR95a]. When a sample is placed in a uniform magnetic field, a dipole moment proportional to the product of the sample's susceptibility and the applied field is induced in the sample. If the sample is vibrated in a

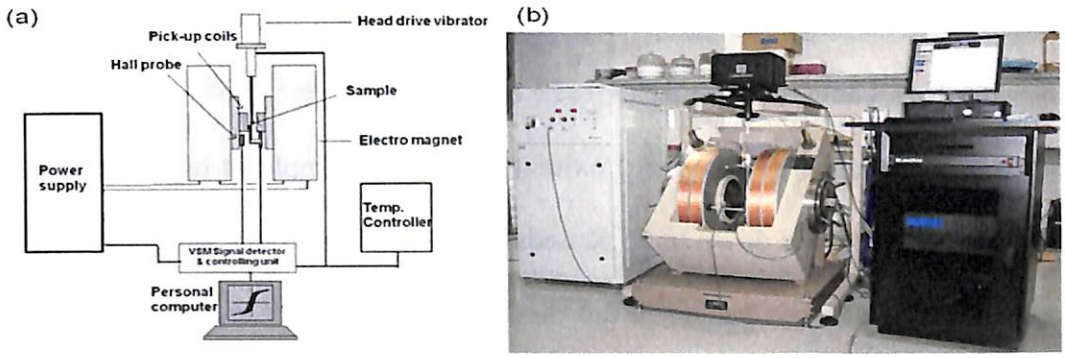

Figure 2.8: (a) Schematic diagram and (b) photograph of a Lakeshore VSM Model 7410.

sinusoidal manner, an electrical signal can be induced in suitably located stationary pick-up coils (*c.f.* Figure 2.8(a)). This signal has amplitude proportional to the magnetic moment of the sample, the vibrating amplitude and the vibration frequency. Through the use of lock-in-amplifier and feedback techniques, only that portion of the signal arising from the magnetic moment is picked up and is converted into direct read-out in *emu* units on a digital panel meter. The VSM consists of the following major parts: (1) water cooled electromagnet and power supply, (2) vibration exciter and sample holder, (3) sensing (pick-up) coils, (4) Hall probe, (5) amplifier, (6) control chassis, (7) lock-in amplifier and (8) computer interface.

The sample is fixed to the lower end of a nonmagnetic (fused silica) sample holder after performing the calibration procedure using standard spherical Ni sample. Subsequently, the measurement sequence is programmed using the software (IDEASVSM) provided with the instrument. The vibration exciter is then activated and the signal received from the probe

and the pick-up coils is converted into the magnetic moment value of the sample. Normally, magnetic field is automatically increased in steps at a constant temperature (*M* - *H* measurements) by an appropriately configured program.

To obtain information on the magnetic phase transition temperatures (say, Curie temperature, T_C and Néel temperature, T_N), magnetization as a function of temperature at a constant applied field (*M* - *T* curves) was recorded for the samples. Variable temperature sample holders attachment capable of providing a controlled heating/cooling of the sample from 25 - 325 K (CCR) and from 325 - 1223 K (HT oven) were used. The oven was purged with high purity nitrogen gas to avoid oxidization of the sample at high temperatures. The sample was initially cooled down to 25 K under zero-field condition. Magnetization was then recorded as the sample was heated to the desired temperature in the presence of a constant magnetic field. Measurement sequences were programmed using in-built IDEASVSM software. Average heating rate of ~3K/minute was employed throughout the studies A sharp decrease in magnetization is observed at the ferromagnetic/ferrimagnetic to paramagnetic phase transition at T_C. T_C is generally determined from the minimum value of the first derivative of *M* - *T* data recorded close to the transition. In antiferromagnetic materials, a peak in magnetic moment value is obtained in *M* - *T* curve at T_N signifying the transition from antiferromagnetic to paramagnetic state.

Paramagnetic Curie temperature, θ_p can be deduced from the inverse susceptibility (χ^{-1}) versus temperature (*T*) plots obtained using Curie-Weiss law in the paramagnetic region,

$$\chi^{-1} = C^{-1}T - C^{-1}\theta_P \qquad (2.11)$$

where *C* is the Curie constant. Positive values of θ_p signify ferromagnetic behavior while and negative values can signify either ferrimagnetic or antiferomagnetic behaviour.

Rhodes-Wohlfarth ratio (p_c/p_s), can be determined from the saturation magnetic moment p_s expressed in units of μ_B at 0 K and p_c (effective magnetic moment per magnetic

atom). The latter factor can be deduced from the Curie constant using the relation [EPWO78a, MJOT89a, NPDU07a],

$$C = \frac{N_A \mu_B^2 p_c(p_c+2)}{3k_B} \quad (2.12)$$

As mentioned in section 1.4.3 in the previous chapter, $p_c/p_s < 1$ for half-metals. A simple molecular field model developed by Otto *et al.* [MJOT89a] to correlate the Rhodes-Wohlfarth ratio with the nature of magnetic interaction in half-Heusler alloys is briefly described below.

The total magnetization (M) of a ferromagnet has contributions from local moments M_1 and itinerant holes M_2, *i.e.*

$$M = M_1 + M_2 \quad (2.13)$$

The magnetization induced by an applied magnetic field H at a temperature above T_C can be written as,

$$M_1 = (C_1/T)(\lambda_{11}M_1 + \lambda_{12}M_2 + H) \quad (2.14)$$

$$M_2 = \chi_P(\lambda_{21}M_1 + \lambda_{22}M_2 + H) \quad (2.15)$$

where $C_1 = N_A g^2 \mu_B^2 S_0(S_0+1)/3k_B$ (2.16)

is the Curie constant of the local moments with spin S_0, χ_P is the Pauli susceptibility of the holes and λ_{ij} are the coupling constants. Therefore, the total susceptibility can be written as,

$$\chi = C_1(1 + \gamma\chi_P\lambda_{12})^2/(T - \theta) + \gamma\chi_P \quad (2.17)$$

with $\gamma = (1 - \lambda_{22}\chi_P)^{-1}$ and $\theta = C_1(\lambda_{11} + \gamma\lambda_{12}^2\chi_P)$. Here, $\gamma\chi_P$ is the temperature-independent Pauli susceptibility and the effective Curie constant,

$$C_{eff} = C_1(1 + \gamma\lambda_{12}\chi_P)^2 \quad (2.18)$$

The value of M_2 at $T = 0$ K, obtained from Eq. 2.15 for $H = 0$ is

$$M_2(0\text{ K}) = -\beta M_1(0\text{ K}) \quad (2.19)$$

with $\beta = -\gamma\lambda_{12}\chi_P$ and $M_1(0\text{ K}) = N_A g\mu_B S_0$. This equation is not valid if β is large. In such a case, M_2 saturates at the value $-p\mu_B$ (where p is the hole concentration). Therefore, the total saturation magnetization at T = 0 K is given by

$$M(0\text{ K}) = N_A g\mu_B S_0(1-\beta) \quad \text{for } \beta < p/NgS_0 \tag{2.20}$$

and

$$M(0\text{ K}) = N_A g\mu_B S_0 - p\mu_B \quad \text{for } \beta > p/NgS_0 \tag{2.21}$$

The R-W ratio (p_c/p_s) can be calculated from these equations. As defined earlier, p_s is calculated from Eq. (2.20) and Eq. (2.21) by the relation $p_s = M(0\text{ K})/N_A\mu_B$. Similarly, p_c can be calculated using the Eq. (2.12), Eq. (2.16) and Eq. (2.18) and applying specific values of S_0, g and p corresponding to a particular alloy composition. For example, in the case of NiMnSb, by considering local moment contribution from Y (Mn) atom, we get S_0 = 5/2, g = 2 and p = N, which gives β = 0.2. So for β < 0.2, M(0 K) = 5N(1 - β)μ_B and p_c/p_s varies from 1 for β = 0 to 0.96 for β = 0.2. For β > 0.2, M(0 K) = 4$N\mu_B$, and p_c/p_s takes the values 0.82 and 0.67 for β = 0.3 and 0.4, respectively. Similarly, for alloys with Fe asY atom, we will get S_0 = 2, g = 2 and p = N which gives β = 0.25. So we get the p_c/p_s becomes 0.93, 0.85 and 0.70 for β = 0.25, 0.3 and 0.4, respectively. Therefore, if we consider the interaction between local moment and spin polarized itinerant electrons, p_c/p_s values will be less than unity. Since NiMnSb has been established to be a half-metallic intermetallic alloy [KEHM90, RJSO98], the prediction of $p_c/p_s < 1$ for half-metallic NiMnSb by Otto et al is considered as a characteristic feature of half-metallic ferromagnets [NPDU07a].

Assessment of the magnetic anisotropy in a material is important to evaluate its potential for spin torque applications. Effective magnetic anisotropy constant K_{eff} is commonly used to represent this parameter. K_{eff} can be estimated from the initial

magnetization (M–H) curves using the law of approach to saturation [SVAN97a]. Magnetization (M) can be expressed as a function of applied field (H) by the relation,

$$M = M_s\left(1 - \frac{a}{\sqrt{H}} - \frac{b}{H} - \frac{c}{H^2} - \cdots\right) + \chi_{hf} H + d\sqrt{H} \qquad (2.22)$$

where χ_{hf} is high field susceptibility and a, b, c, d are constant coefficients were a and b represent contributions from various defects. c and d are assigned to magneto-crystalline anisotropy and thermally excited spin waves, respectively. At high fields, only the c/H^2 term dominates and hence all other contributions can be neglected [ZQJI98a, CJIA04a]. So, for high applied field is, Eq. (2.22) simplifies to

$$M(H) = M_s\left(1 - \frac{c}{H^2}\right) \qquad (2.23)$$

Once c is correctly estimated, magneto crystalline anisotropy constant, K_{eff} for cubic sample can be estimated from the relation [XYXI01a],

$$K_{eff} = \mu_0 M_s\left(\frac{105c}{8}\right)^{\frac{1}{2}} \qquad (2.24)$$

where μ_0 is the permeability of free space.

2.4. SPIN POLARIZATION MEASUREMEMT

2.4.1. Point contact Andreev reflection (PCAR) technique

Andreev reflection is a process that occurs at the interface between normal metal and a superconductor [AFAN64a]. For a given bias across the metal-superconducting interface, the electrons from the metal enter into the superconductor by forming Cooper pairs. Since the normal metal has the equal number of both spin-up and spin-down density of states, the spin-up electron pairs up with spin-down electron to form Cooper pair and enters into the superconducting condensate states as super-current, leaving behind a hole in the spin-down

density of states (apart from the normal hole in the spin-up states) as shown in Figure 2.9. As a result, electrical conduction due to the conventional current (due to holes) doubles at the interface. This coherent interspin-subband transfer process is sensitive to the relative electronic spin density of states or P at E_F. If $P = 0$, then the Andreev reflection is unhindered. However, if $P = 100\%$ near E_F, then there are no spin-down states in the metal to provide the other member of the Cooper pair for Andreev reflection. So, super-current conversion *via* Andreev reflection at the interface is effectively blocked, allowing only single-particle excitations to contribute to the conductance. These single-particle states necessarily see the gap (Δ) in the energy spectrum of the superconductor, thus suppressing the conductance G for $eV < \Delta$.

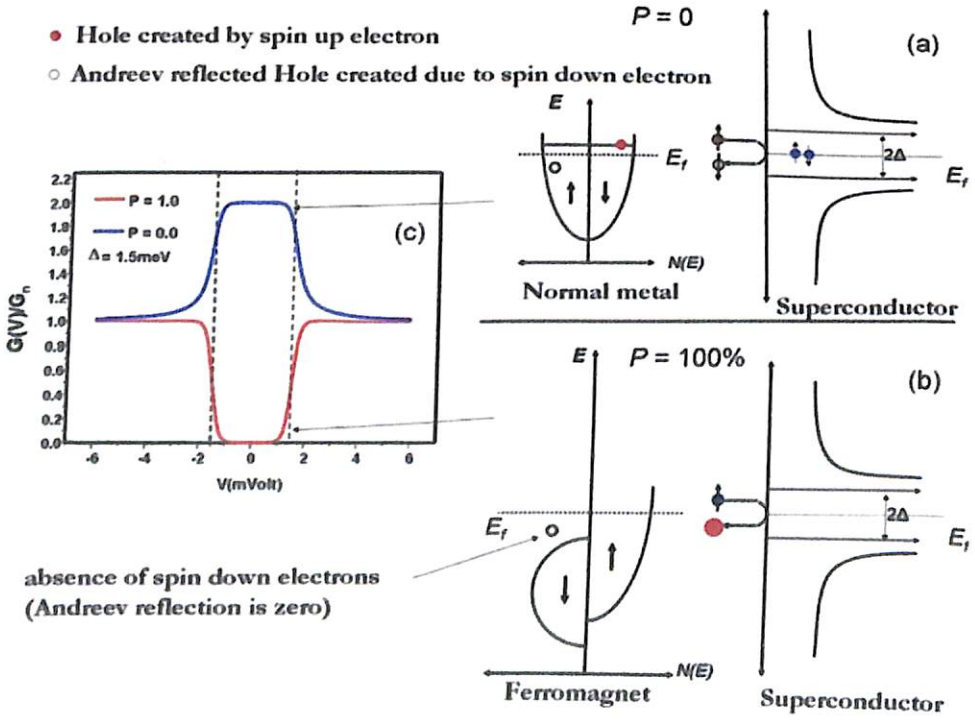

Figure 2.9: (a) Metal-superconductor junction. (b) Ferromagnetic metal-superconducting junction. (c) Blue curve represents Andreev reflection with double conductance and red the curve represents the suppression of Andreev reflection [RJSO98a].

The Andreev reflection process only occurs for a micro-constricted contact and the transport regime in these experiments are mainly ballistic in nature. In PCAR, this is realized by bringing a superconductor tip in close contact with a ferromagnetic material or *vice versa* as proposed by Soulen *et al.* [RJSO98]. Later, Striker *et al.* [GJST01a] developed a new model with some modifications to the original Blonder-Tinkham-Klapwijk (BTK) theory [GEBL82a]. In our study, the modified BTK model was used to fit the normalized conductance-voltage curves for the estimated interfacial scattering parameter (Z) and the temperature (T). To apply BTK model, the diameter of the contact has to be smaller than the electron mean free path.

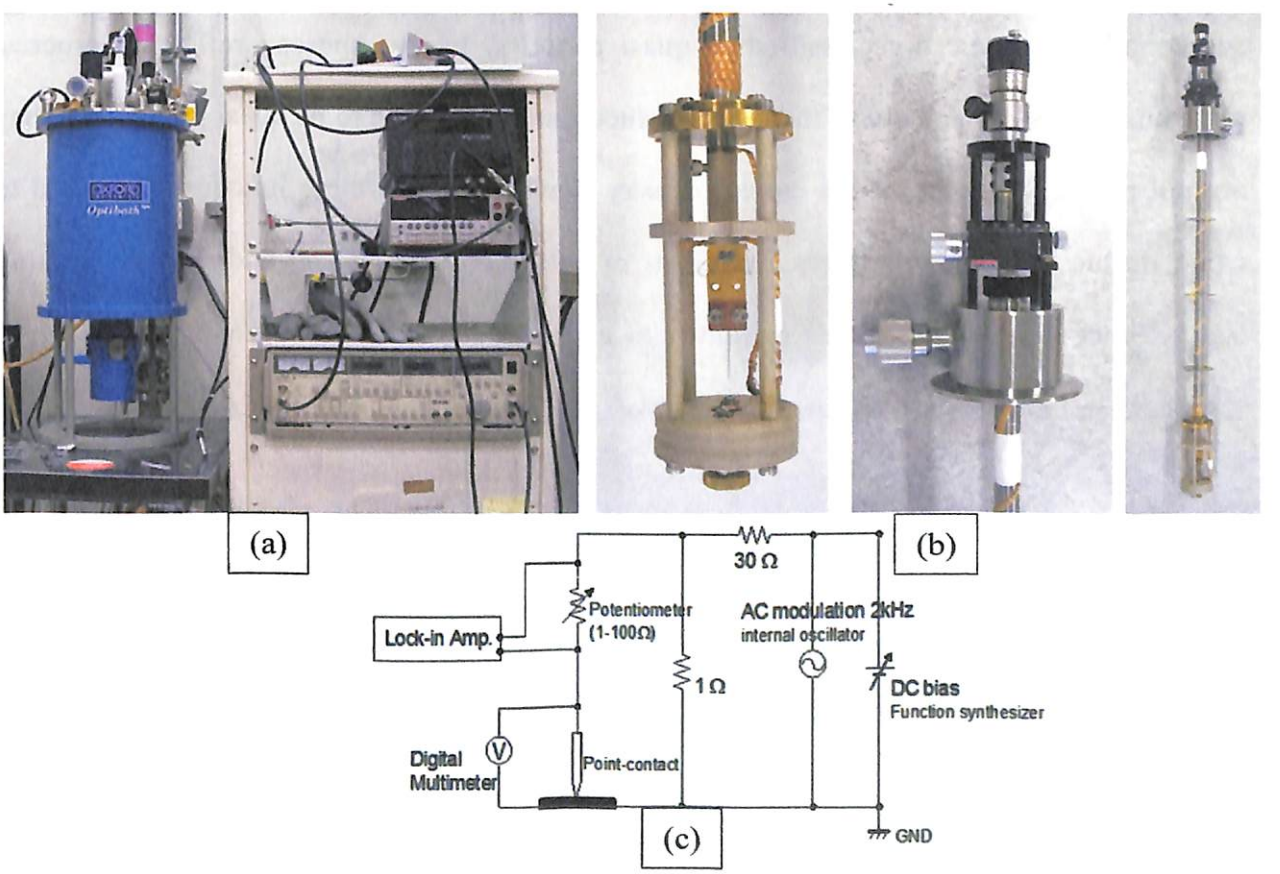

Figure 2.10: (a) PCAR measurement apparatus consisting of a liquid He cryostat and electronic instruments. (b) Close-up view of the sample holder with Nb tip mounted on it. (c) Electronic circuit for recording the conductance as a function of DC bias [WWWNb]

Figure 2.10(a) shows the picture of PCAR measurement set-up. The sample is placed inside the liquid He cryostat. Sample holder with the sample and the Nb tip is shown in Figure 2.10(b). Polished Nb tip is pushed down on to the sample surface by externally operating a micrometer screw. The electronic circuit consisting of a power supply, multimeter and lock-in amplifier for measuring the conductance in the samples is also shown in the figure 2.10(c). A computer interface used for continuous recording of the normalized conductance-voltage curves is not shown in the figure.

Analysis of conductance-voltage curves using BTK model

In a typical superconductor, all electrons and holes which are not paired in the superconducting state are classified as quasi particles. In the Andreev reflection process, electrons flowing in and out of the superconductor are considered to be quasi particles as they are not paired. To estimate the current density flowing through these junctions, we need to calculate the Eigen states of quasi particles in both the normal metal and superconducting states. Since quasi particles can exhibit both electron-like and hole-like nature, their wave function can be represented by the Bogoliubov–de Gennes equation [PGDE66a],

$$i\hbar\frac{\partial\Psi(x,t)}{\partial t} = \begin{pmatrix} H(x) & \Delta(x) \\ \Delta(x) & -H(x) \end{pmatrix}\Psi(x,t) \qquad (2.25)$$

where $\Psi(x,t) = \begin{bmatrix} f(x,t) \\ g(xt) \end{bmatrix}$, $\Delta(x)$ is the spatially dependent superconducting energy gap, and

$H(x) = -\frac{\hbar^2}{2m}\frac{d^2}{dx^2} + V(x) - E_F$.

In BTK model, $\Delta(x)$ is assumed to be spatially independent and $V(x)$ is assumed to be zero. With these assumptions we can obtain an Eigen function solution of the form,

$$\Psi(x,t) = \begin{bmatrix} u \\ v \end{bmatrix} \exp^{i(kx-\omega t)} \qquad (2.26)$$

which gives the Eigen energy solution, $E^2 = \left[\frac{\hbar^2 k^2}{2m} - E_F\right]^2 + \Delta^2$ (2.27)

The sketch of this energy is shown in Figure 2.11 for a normal metal (with $\Delta = 0$) and a superconductor (with $\Delta > 0$). The positive solution of the energy refers to the electron quasiparticles and the negative one to hole quasiparticles. Using boundary conditions at the interface, probability of reflection $A(E)$, $B(E)$ and probability of transmission $C(E)$, $D(E)$ can be evaluated in terms of a dimensional quantity Z often called the barrier strength, representing the strength of the scattering potential $H\delta(x)$. Z is defined as

$$Z = \left(\frac{mH^2}{2\hbar^2 E_F}\right)^{1/2} \quad (2.28)$$

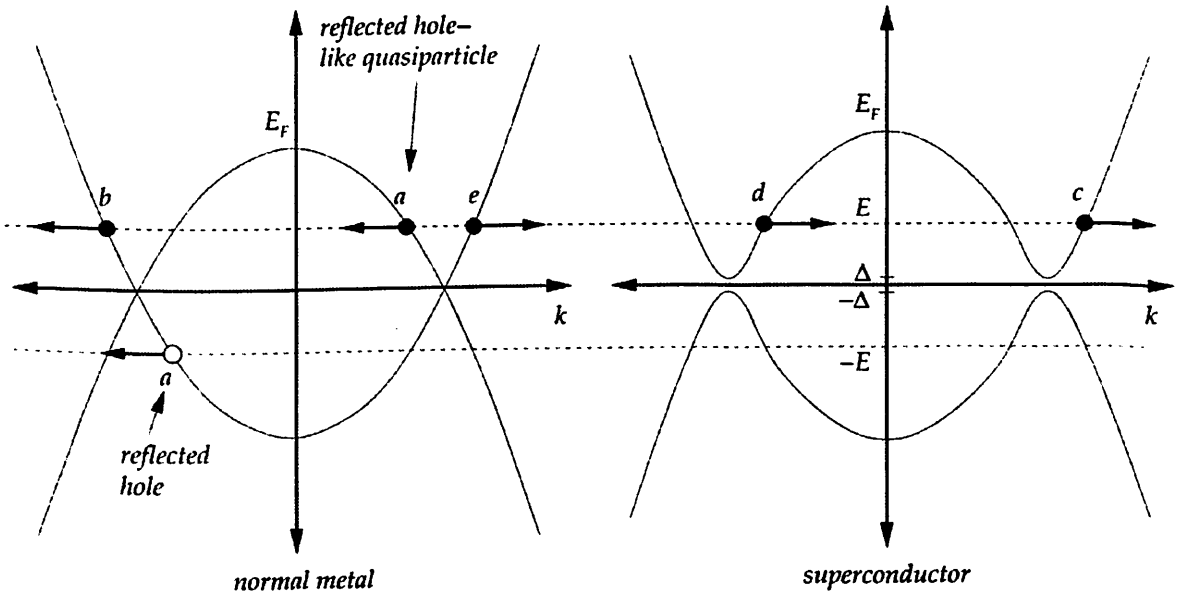

Figure 2.11: Band diagram for normal (left) superconductor (right) interface for the BTK model. Label *e* is the incident electron, *a* is Andreev reflection, *b* is normal reflection, *c* is electron like transmission, and *d* is hole like transmission [ANUR12a].

The conductance, defined as $G = dI/dV$ can be derived for both normal metal and normal metal-superconductor system, giving the conductance ratio as

$$\frac{G(V)}{G_n} = -(1+Z^2)\int[1+A(E)-B(E)]f'(E-\mathrm{eV})dE \qquad (2.29)$$

which is the main result of BTK theory. $f'(E)$ refers to the derivative of Fermi–Dirac distribution function $f(E)$ with respect to energy. However, this model does not include spin polarization. Later, Strijker *et al.* [GJST01a] proposed a very straightforward model to include the spin polarization in the theory. They related the polarized and the non-polarized currents in a linear combination to obtain the total current,

$$I = (1-P)I_n + PI_p \qquad (2.30)$$

where I_n and I_p are the non-polarized and polarized currents The non-polarized current can be calculated using the standard BTK theory while the polarized current needs to be calculated with modified expressions for refection probabilities $\tilde{A}$ and $\tilde{B}$. The conductance ratio for the spin polarized system is hence given by,

$$\frac{G_{NS}}{G_{NN}} = -P(1+Z^2)\int[1+\tilde{A}(E)-\tilde{B}(E)]f'(\mathrm{E}-\mathrm{eV})dE - (1-P)(1+Z^2)\int[1+A(E)-B(E)]f'(\mathrm{E}-\mathrm{eV})dE \qquad (2.31)$$

Normalized conductance (open circles) as a function of V recorded for a spin polarized Heusler alloy along with fit to modified BTK model (solid line) is shown in Figure 2.12. A least squares fitting procedure adopted to estimate the spin polarization uses dimensionless interfacial scattering parameter Z, superconducting gap Δ and spin polarization as variable parameters. The parameters estimated from best fit to the data are shown in the figure. ntrinsic spin polarization P of the half-metallics alloy corresponds to the spin polarization value obtained at $Z = 0$.

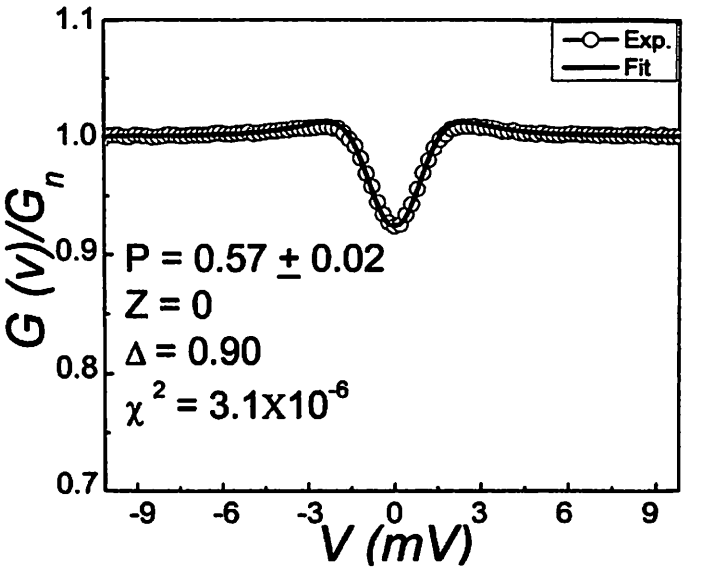

Figure 2.12: Typical normalized conductance curve with low Z obtained from PCAR measurements

2.5. *AB INITIO* CALCULATIONS

In the last few decades, density functional theory (DFT) has turned out to be a popular quantum mechanical approach to the study of matter [DSHO09a]. DFT offers a powerful way to calculate the ground state properties for many body systems with interacting electrons. It is extensively applied for calculating the band structure of solids, binding energy of molecules, etc. DFT has been widely used in different areas of solid state physics. It has been immensely successful in explaining the magnetic properties of transition metals and transition metal based alloys [DSHO09a].

According to Born-Oppenheimer approximation, the nuclei of the many body system in electronic structure calculations are assumed as fixed, *i.e.*, the nuclear kinetic energy is zero and the potential energy is merely a constant. Thus, the electronic part of the Schrodinger equation can be written as,

$$H\Psi(r_1, r_2, \ldots . r_N) = [T + V_{ext} + U_{ee}]\Psi(r_1, r_2, \ldots . r_N)$$

$$= \left[-\frac{\hbar^2}{2m}\sum_i^N \nabla_i^2 + \sum_i^N V(r_i) + \sum_{i\neq j}^N U(r_i, r_j)\right]\Psi(r_1, r_2, \ldots . r_N)$$

$$= E\Psi(r_1, r_2, \ldots . r_N) \tag{2.32}$$

where $\Psi(r_1, r_2, \ldots . r_N)$ is the wave function of stationary electronic state, N is the number of electrons and U_{ee} is the electron-electron interaction. The operators T and U_{ee} which are common for similar systems, are called universal operators. V is system dependent and so non-universal. DFT provides a way to systematically map the many-body problem with U_{ee} onto a single particle problem without U by using the key variable,

$$n(r) = N \int dr_2 \int dr_3 \int dr_4 \ldots . \int dr_N |\Psi(r, r_2, \ldots . r_N)|^2 \tag{2.33}$$

Historically, DFT has its conceptual roots in the Thomas-Fermi model [LHTH27a]. However, exchange and correlation effects are neglected in this model, which seriously limits its accuracy. Hohenberg and Kohn started from Thomas-Fermi theory and established the connection between the electron density $n(r)$ and the many-electron Schrodinger equation [PHOH64a]. The first and second Hohenberg and Kohn theorems can be stated as

1. The ground state density $n_0(\mathbf{r})$ of interacting electrons in some external potential $v_{ext}(\mathbf{r})$ determines this potential uniquely.
2. For any given density $n(\mathbf{r})$ associated to an N electron system with external potential $v_{ext}(\mathbf{r})$, the minimum of the energy function is obtained with the ground state density.

Therefore, the ground state energy E_0 can be written as,

$$E_0 \leq E[n] = T[n] + V[n] + U[n] \tag{2.34}$$

E_0 can be obtained by minimizing the function $E[n]$ with respect to $n(\mathbf{r})$ if the functions $T[n]$ and $U_{ee}[n]$ are known. A successful minimization of the energy function will yield the ground state density $n_0(\mathbf{r})$ and hence all other ground state properties of interest. In 1965, Kohn and Sham showed that the variational problem of minimizing the energy function can be

solved by applying the Lagrangian method of undetermined multipliers [WKOH65a]. The derived set of equations known as Kohn-Sham equations can be expressed as,

$$\left[-\frac{\hbar^2}{2m}\nabla^2 + v_{eff}(r)\right]\psi_i(r) = \varepsilon_i\psi_i(r) \tag{2.35}$$

which are single particle Schrodinger equations, where the external potential has been replaced by an effective potential given by,

$$v_{eff}(r) = v_{ext}(r) + e^2\int\frac{n(r')}{|r-r'|}dr' + v_{xc}(r) \tag{2.36}$$

where the exchange correlation potential is given by

$$v_{xc}(r) = \frac{\delta(E_{xc}[n])}{\delta n(r)} \tag{2.37}$$

The Kohn-Sham equation has to be solved self-consistently. Usually, one starts with an initial guess for the density $n(\mathbf{r})$, calculates the corresponding effective potential $v_{\text{eff}}(\mathbf{r})$ and then solves the Kohn-Sham equations for ψ_i. From these, one calculates a new density and repeats the above steps again. This procedure is repeated until convergence is reached. Once this is done, the ground state energy can be expressed by the Kohn-Sham formula given by,

$$E_0 = \sum_{i\ occ}\varepsilon_i - \frac{e^2}{2}\int drdr'\frac{n(r)n(r')}{|r-r'|} + E_{xc}[n(r)] - \int v_{xc}(r)n(r)dr \tag{2.38}$$

The spin density functional formalism is obtained by introducing two spin densities $n^{\uparrow}(r)$ and $n^{\downarrow}(r)$. So, the spin dependent exchange correlation potential can be written as,

$$v_{xc}(n^{\uparrow}, n^{\downarrow}r) = \frac{\delta(E_{xc}[n^{\uparrow},n^{\downarrow}])}{\delta n^{\sigma}(r)} \tag{2.39}$$

where σ ($\uparrow$ or $\downarrow$) depends on both the spin densities.

Though Kohn-Sham formalism reduces the many-particle interacting electron problem to an effective single particle Schrodinger equation, the solution of Eq. (2.35)

requires certain approximations. The major problem with DFT is that the exact functions for exchange and correlation are not known except for the free electron gas. However, approximations exist which permit the calculation of certain physical quantities quite accurately. The most widely used approximations are the Local Density Approximation (LDA) [WKOH65a] and the Generalized Gradient Approximation (GGA) [JPPE86a, JPPE89a]. Within LDA, exchange correlation energy depends only on the density at the coordinate where the function is evaluated and expressed as,

$$E_{xc}[n] = \int n(r)\epsilon_{xc}[n(r)]dr \tag{2.40}$$

where $\epsilon_{xc}[n(r)]$ is the exchange and correlation energy per particle of a uniform electron gas of density $n(\mathbf{r})$. The first attempt to go beyond the LDA involved the use of not only the information about the density $n(\mathbf{r})$ at a particular point $\mathbf{r}$ but also the information about the density gradient $\nabla n(\mathbf{r})$ in order to account for the non-homogeneity of the true electron density. The resulting GGA is given by the expression,

$$E_{xc}[n] = \int n(r)\epsilon_{xc}[n(r), \nabla n(r)]dr \tag{2.41}$$

Ab initio calculations have been carried out on Co_2-alloys in Chapter 3 of this thesis with spin-polarized DFT based plane wave pseudopotential method as implemented in Vienna Ab-initio Simulation Package (VASP) [GKRE96a, GKRE99a]. The crucial exchange-correlation part was approximated through PBE-Generalized Gradient Approximation (PBE-GGA) [JPPE96a]. To include electron-electron correlations for selected alloys, we used the GGA+U approximation as implemented by Dudarev *et al.* [SLDU98a]. In this implementation, strong electron-electron correlation is modeled by an effective parameter $U_{eff} = U - J$, where U stands for the onsite Coulomb interaction and J is Hund's rule coupling parameter. The self-consistent Kohn-Sham equations were solved with a plane

wave cut off of 500 eV and 15 × 15 × 15 Monkhorst-Pack (M-P) *k*-point mesh [HJMO76a]. For density of states (DOS) calculations, we have used tetrahedron method with M-P *k*-point mesh of 27 × 27 × 27. A 16 atom conventional cell composed of 8 X atoms, 4 Y atoms and 4 Z/Z′ atoms was considered to represent $Co_2Fe(Z_{1-x}Z'_x)$ alloys.

The electronic structure of $Ru_2Fe(Si_{1-x}Ge_x)$ alloys presented in Chapter 4 has been calculated using full-potential based Spin-polarized Relativistic Korringa-Kohn-Rostoker (SPR-KKR) Green's function method. GGA was used as the exchange-correlation part to solve the Kohn-Sham equation. The angular moment cut-off to the plane wave was taken to be $l_{max} = 3$. The Brillouin zone integrations have been carried out on a uniform 24 × 24 × 24 *k*-mesh. The Green's function was calculated for 30 complex energy points distributed exponentially on a semi-circular contour. The energy convergence criterion was set to 10^{-6} Ry for the self-consistent cycles. The Coherent Potential Approximation (CPA) was used to incorporate the effect of disorder. B2 disorder was achieved by assigning 50% occupancy of Y and 50% occupancy of Z to both 4a and 4b Wyckoff positions. Magnetic properties of the Ru_2FeZ Heusler compounds can be well described by the classical Heisenberg Hamiltonian, $H = -\sum_{<i,j>} J_{ij} \boldsymbol{e}_i \boldsymbol{e}_j$ where the sum runs over all the different Fe-Fe pairs and $\boldsymbol{e}_i$ represents the unit vector pointing along the magnetic moment of the i^{th} Fe site. Heisenberg exchange integral (J_{ij}) was calculated as a function of interatomic distance between Fe atoms to study the magnetic ordering in the alloys. In the case of chemical disorder between Fe and Z sub-lattices, the sum in Hamiltonian equation also includes sites on the Z sub-lattice occupied by Fe atoms.

Chapter 3

INVESTIGATIONS ON $Co_2Fe(Ge_{1-x}Si_x)$ AND $Co_2Fe(Ga_{1-x}Si_x)$ ALLOYS

Since the discovery of half-metallicity in full Heusler alloy Co_2MnSi by Ishida *et al.* [SISH95a], Co_2-based Heusler alloys have attracted immense attention mainly due to their high Curie temperature (T_C), large saturation magnetization (M_s) and theoretically predicted half-metallic nature [IGAL02a, JKUB07a, HCKA07b, JCTU13a]. Half-metallicity in a wide variety of Co_2-based full Heusler alloys has been explored by experimental [DBOM13a, LMAK13a, SOKI12a, ZGER06a, SVKA07a, KHAM12a, SVKA07b, IMIM12a, YWU13a, BSDC12a] as well as theoretical [IGAL02a, JKUB07a, HCKA07b, JCTU13a, LMAK13a] methods. PCAR studies show that ternary Heusler alloys invariably exhibit $P \leq 0.60$ [LJSI04a, MJHA04a, ARAJ07a, ARAJ07b, BSDC09a, BSDC10a], although TMR measurements on Co_2MnSi show a higher tunneling spin polarization (P_t) of 0.89 [YSAK06a]. TMR of 570% observed at 2 K in Co_2MnSi/Al–O/Co_2MnSi MTJ reduces to 67% at room temperature, indicating the drastic deterioration of half-metallic character of Co_2MnSi alloy at room temperature. Galanakis [IGAL04a] proposed Fermi level engineering by substituting a fourth element in the ternary Heusler compound as a means to overcome this drawback. Substitution of a fourth element in Co-based alloys has yielded several highly spin polarized ferromagnetic full Heusler quaternary alloys [BSDC09a, BSDC10a, SVKA06a] such as $Co_2Fe(Ga_{0.5}Ge_{0.5})$ [BSDC12a]. As discussed in the first chapter, Co_2-based Heusler alloys show promising results in magneto-resistance devices. High MR ratio of 36.4% was obtained at room temperature in epitaxial CPP-GMR device with Co_2MnSi electrodes [YSAK10a]. Since then, CPP-GMR structures with ferromagnetic $Co_2Fe_{0.4}Mn_{0.6}Si$, $Co_2Fe(Ga_{0.5}Ge_{0.5})$ and $Co_2Mn(Ga_{0.25}Ge_{0.75})$ electrodes have demonstrated higher MR ratios of 74.8% [JSAT11a], 45.8% [HSGO13a], and 40.2% [YKTA13a], respectively, at room temperature. Giant TMR of up to 1995% at 4.2 K and up to 354% at 290 K have been reported for epitaxial Co_2MnSi /MgO/Co_2MnSi magnetic tunnel junctions

(MTJs) [HLIU12a]. Enhancement in TMR up to 2610% at 4.2 K and 429% at 290 K has been achieved in MTJs with $Co_2Mn_{1.24}Fe_{0.16}Si_{0.84}$ ferromagnetic electrodes [HLIU15a]. Among these alloys, Co_2FeSi has the advantage of high T_C (~1100 K) and high M_S ($6\mu_B$) [SWUR05a]. Considering the advantage of quaternary alloys, it is worthwhile to explore the influence of substituting Si with elements such as Ge and Ga in Co_2FeSi.

3.1. Preparation of alloys

Polycrystalline $Co_2Fe(Ge_{1-x}Si_x)$ and $Co_2Fe(Ga_{1-x}Si_x)$ ($0 \leq x \leq 1$) alloy ingots were prepared by arc melting method followed by homogenization at 1173 K for 24 h and quenching in ice + water mixture as described in the previous chapter. The overall composition of the alloys as determined by EDS analysis was found to be close to the nominal (starting) composition of the respective alloys (*cf.* Table 3.1 and Table 3.5).

3.2. $Co_2Fe(Ge_{1-x}Si_x)$; ($0 \leq x \leq 1$) alloys

3.2.1. Crystal structures

Figure 3.1 shows X-ray diffraction (XRD) patterns of $Co_2Fe(Ge_{1-x}Si_x)$ alloys recorded at ambient temperature. As discussed in section 2.2.1 in the previous chapter, Bragg reflections with non-zero structure factor corresponding to a fully ordered $L2_1$ structure is obtained only when all indices are either even or odd. The alloys with $x = 0.75$ and $x = 1.0$ exhibit a single phase $L2_1$ structure with the characteristic (111) and (200) super-lattice reflections in their XRD patterns. However, these super-lattice peaks could not be observed in the XRD patterns of the alloys containing high Ge concentrations. Though these XRD patterns suggest a disordered A2 structure at a first glance, one should bear in mind that nearly equal X-ray scattering factors of Co, Fe and Ge, could also yield the same pattern [BBAL07a]. XRD patterns simulated for $Co_2Fe(Ge_{1-x}Si_x)$ alloys with $L2_1$ unit cell using CaRIne^{TM} software shown in Figure 3.2 mimic the experimental patterns confirming this claim.

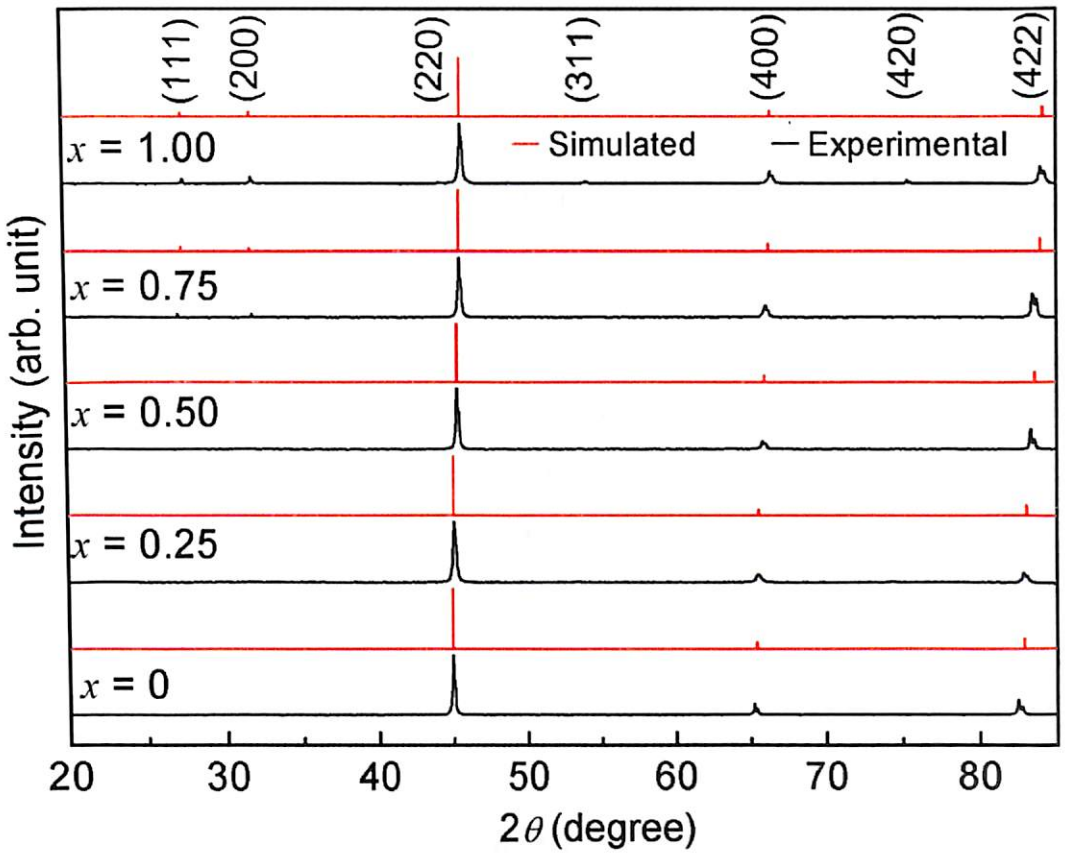

Figure 3.1: Room temperature XRD patterns of $Co_2Fe(Ge_{1-x}Si_x)$ ($0 \leq x \leq 1$) alloys. Simulated XRD patterns for the alloys with $L2_1$ structure are also shown for comparison.

The experimental XRD patterns were refined by Rietveld method using FullProf 2.00 software. The lattice constant *a* obtained from the Rietveld analysis of the cubic samples with $x = 0$, 0.25, 0.50, 0.75 and 1.00 are 5.70 Å, 5.69 Å, 5.66 Å, 5.64 Å and 5.63 Å, respectively. Table 3.1 summarizes the lattice parameters and unit cell volume estimated from the XRD patterns. Lattice constant and unit cell volume decrease with an increase in x because the atomic radius of Si (= 1.46 Å) is smaller than that of Ge (= 1.52 Å). The lattice constant of Co_2FeGe and Co_2FeSi are found to be 5.70 Å and 5.63 Å respectively, which are in agreement with reports in the literature [KRKU09a, SWUR06a].

Table 3.1: Nominal composition, measured composition, lattice parameter, unit-cell volume and Bragg factor R_B of Rietveld refinement of $Co_2FeGe_{1-x}Si_x$ ($0 \leq x \leq 1$) alloys.

Alloy ID	Nominal Composition	Measured Composition	a (Å)	Unit-cell volume (Å^3)	R_B
$x = 0$	Co_2FeGe	$Co_{1.99}Fe_{1.01}Ge$	5.70	185.19	7.5
$x = 0.25$	$Co_2FeGe_{0.75}Si_{0.25}$	$Co_2Fe_{0.99}Ge_{0.76}Si_{0.25}$	5.69	184.22	8.8
$x = 0.50$	$Co_2FeGe_{0.50}Si_{0.50}$	$Co_2FeGe_{0.50}Si_{0.50}$	5.66	181.32	9.2
$x = 0.75$	$Co_2FeGe_{0.25}Si_{0.75}$	$Co_{2.01}Fe_{0.99}Ge_{0.25}Si_{0.75}$	5.64	179.41	6.4
$x = 1.00$	Co_2FeSi	$Co_2Fe_{0.99}Si_{1.01}$	5.63	178.45	8.8

3.2.2. Magnetic properties

Room temperature initial magnetization and M-H curves of $Co_2Fe(Ge_{1-x}Si_x)$ alloys are shown in Figure 3.2(a,b). The curves exhibit typical ferromagnetic characteristics with magnetic saturation within 15 kOe. Saturation magnetization M_s for the alloys was determined at the magnetization value at 15 kOe. M_s of the alloys with x = 0, 0.25, 0.50, 0.75 and 1.00 are 5.99μ_B, 5.92μ_B, 5.72μ_B, 5.53μ_B and 5.42μ_B, respectively. Since the total number of valence electrons (Z_t) is 30 for all the alloy compositions in this series, these alloys are expected to possess a total magnetic moment (M_t) of 6.00μ_B as per the S-P rule (Eq. 1.5). Predicted M_t can be compared with the M_s determined for various alloy compositions from VSM studies. The alloy with x = 0 follows the S-P rule with M_s = 5.99μ_B. However, as Si content is increased, M_s deviates from the value of 6.0μ_B predicted by the S-P rule as illustrated by Table 3.2. S-P rule prediction is based on the nominal composition of the alloy. Tables 3.1 and 3.2 show that even if one takes the actual (measured using EDS) composition into consideration, the observed deviation in the measured M_s of the alloys with $x > 0$ from the predicted M_t values

cannot be accounted for. *Ab initio* studies presented in section 2.5 will attempt to reconcile this difference between the theoretical and experimental results.

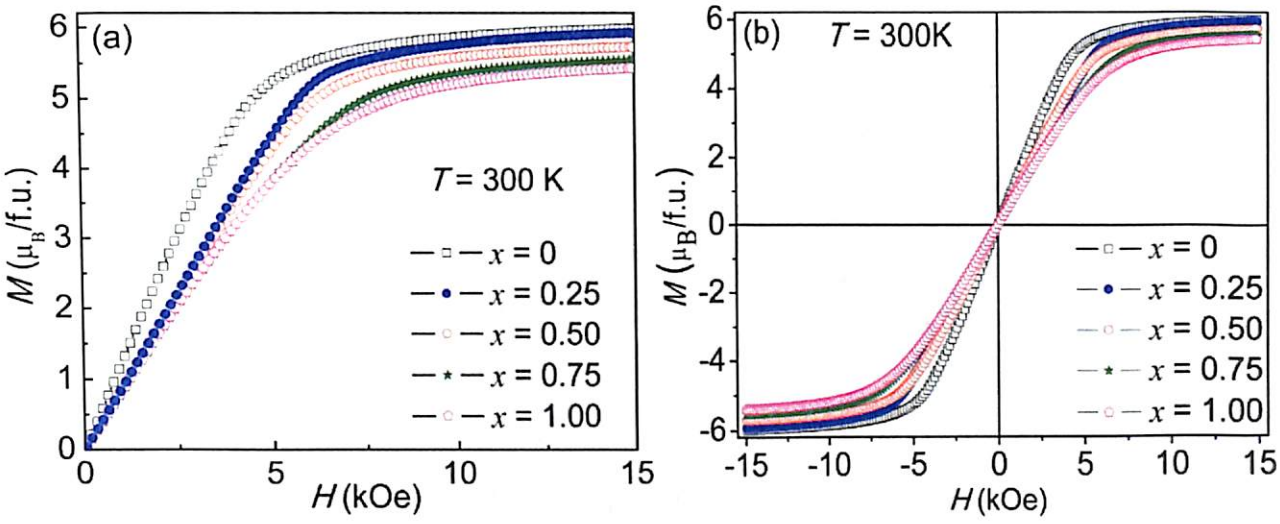

Figure 3.2: (a) Variation of room temperature initial magnetization (M) with applied magnetic field (H) and (b) M-H loops of $Co_2FeGe_{1-x}Si_x$ alloys.

K_{eff} values for the alloys were calculated from the M-H data depicted in Figure 3.2(a) using the law of approach to saturation (Eq. 2.23 and Eq. 2.24) and summarized in Table 3.2. K_{eff} increases from 7.12×10^5 Jm^{-3} to 11.17×10^5 Jm^{-3} as x is increased from 0 to 1.00. Thus, K_{eff} varies by nearly half and order as x is varied from 0 to 1.00 in $Co_2FeGe_{1-x}Si_x$ alloys.

Figure 3.3 shows the thermo-magnetization curves for the alloys at an applied magnetic field of 100 Oe. High T_C is obtained for all the compositions as expected for these alloys. T_C obtained for the alloys with $x = 0$ and 1 are 980 K and 1015 K, respectively, in close agreement with earlier reports [SWUR06a, RYUM12a]. T_C increases with increasing x (980 K, 987 K, 999 K, 1008 K and 1015 K for $x = 0$, 0.25, 0.5, 0.75 and 1.00, respectively) indicting improved ferromagnetic ordering with increasing Si content.

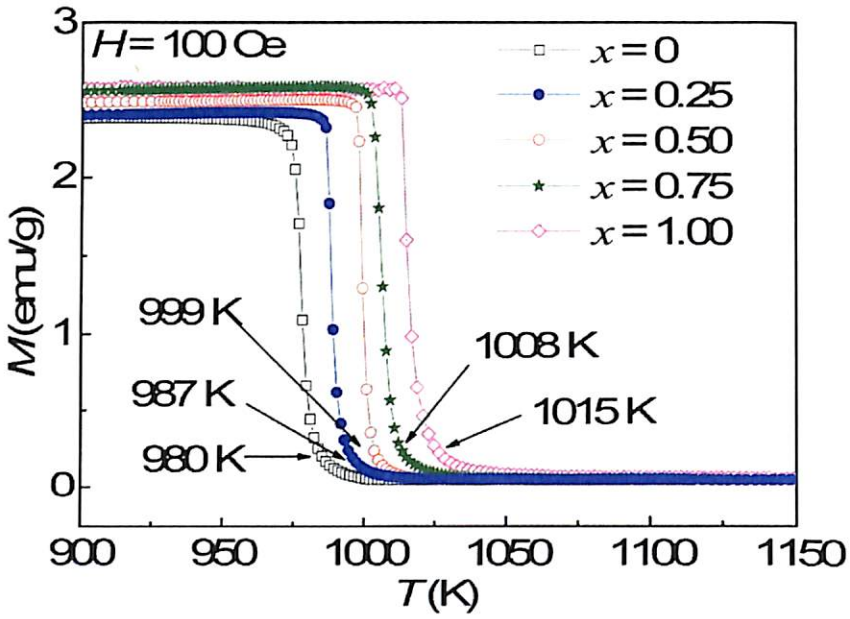

Figure 3.3: Thermo-magnetization curves of $Co_2Fe(Ge_{1-x}Si_x)$ alloys recorded at 100 Oe.

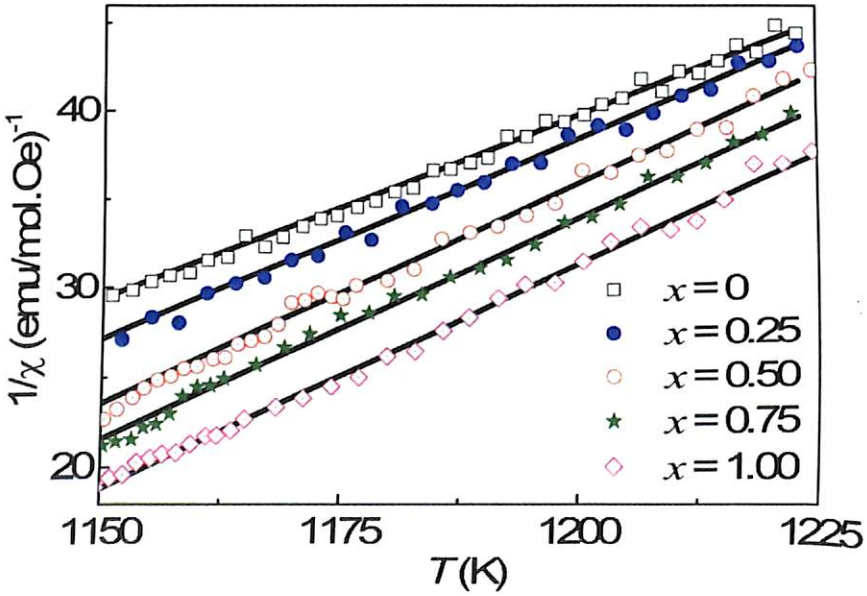

Figure 3.4 Inverse magnetic susceptibility (χ^{-1}) as a function of temperature (T) of $Co_2Fe(Ge_{1-x}Si_x)$ alloys for $T > T_C$.

Figure 3.4 shows the Curie-Weiss plots depicting the variation of magnetic susceptibility (χ^{-1}) for $T > T_C$. Saturation magnetic moment p_s of the alloys was estimated

from these plots, which was used to determine the Rhodes-Wohlfarth ratio (p_c/p_s) of the alloys displayed in Table 3.2 by the procedure outlined in section 2.3.1. It can be seen from the table that $p_c/p_s < 1$ for all the alloy compositions, indicating all the alloys to be half-metallic. Since Rhodes-Wohlfarth ratio is determined from experimentally determined parameters, it is also considered as an experimental method for identifying ferromagnetic half-metals. Therefore, $Co_2Fe(Ge_{1-x}Si_x)$ alloys with $0 \leq x \leq 1$ can be presumed to possess half-metallic character. So, one would expect $Co_2Fe(Ge_{1-x}Si_x)$ alloys to have a total magnetic moment (or M_s) of $6\mu_B$, predicted by the S-P rule. In order to explain this deviation in M_s of some of the alloys with respect to the S-P rule and to verify the half-metallic character of $Co_2Fe(Ge_{1-x}Si_x)$ indicated for all the alloys by the Rhodes-Wohlfarth ratio, we take recourse to the DFT based *ab initio* calculations.

Table 3.2: Experimentally determined saturation magnetic moment (M_s), M_t calculated using nominal composition (M_{Nom}) and EDS measured composition (M_{EDS}), effective anisotropy constant (K_{eff}), effective moment per magnetic atom (p_c) and p_c/p_s for $Co_2Fe(Ge_{1-x}Si_x)$ alloys. Total magnetic moment (M_{th}) obtained for $L2_1$ (using GGA and GGA+U) and DO_3 disordered structures from *ab initio* calculations are given for comparison.

x	M_s (μ_B)	M_{Nom} / M_{EDS} (μ_B)	K_{eff} ($\times 10^5$ Jm^{-3})	p_c (μ_B)	p_c/p_s	$M_{th(GGA)}$ ($L2_1$) μ_B	$M_{th(GGA+U)}$ ($L2_1$) μ_B	M_{th} (DO_3) μ_B
0	5.99	6.00 / 5.99	7.12	5.27	0.88	5.60	6.00	5.99
0.25	5.92	6.00 / 5.96	8.92	5.01	0.78	5.59	6.00	5.50
0.50	5.72	6.00 / 6.00	9.87	4.8	0.78	5.54	6.00	5.50
0.75	5.53	6.00 / 6.01	9.98	4.80	0.83	5.50	6.00	5.50
1.00	5.42	6.00 / 5.96	11.17	4.74	0.86	5.49	6.00	5.35

It is worthy to point out here that M_s of Co_2FeSi (*i.e.*, $x = 1$) alloy reported in the literature are also lower that the value of $6.0\mu_B$ predicted by the S-P rule (*e.g.*, $5.91\mu_B$

[VNIC77a], 5.18μ_B [KHJ83a], 5.73μ_B [TMNA07a] and 5.87μ_B [RYUM12a]). This disparity in the experimental results can be attributed to atomic disorders and deviations in composition from stoichiometry in the reported Co_2FeSi alloy. Chemical composition of our samples has been verified by EDS to be within 1% of the nominal composition. Apart from this, the presence of (111) and (200) super-lattice peaks in its XRD pattern establishes an ordered $L2_1$ structure of our Co_2FeSi alloy. These eliminate the commonly observed B2 and A2 type atomic disorders in this alloy and deviation from stoichiometry as possible reasons for the lower M_s. Theoretically, it has been shown that small amount of B2 disorder does not affect the M_s as well as half-metallicity of the alloy [RMOHA15a]. However, presence of DO_3 disorder, which can arise due to intermixing of X (Co) and Y (Fe) atoms, can reduce the moment due to different environment experienced by the magnetic atoms Co and Fe [ZGER07a]. Thus, DO_3 disorder is a possible source for the observed M_s. Experimentally, it is very difficult to estimate the exact amount of DO_3 disorder from XRD studies due to nearly equal scattering factors of Co and Fe [BBAL07a]. Hence, DO_3 disorder is considered in our DFT calculations.

3.2.3. *Ab initio* calculations

As discussed in the previous chapter, *ab initio* calculations were performed using GGA within the Vienna Ab initio Simulation Package (VASP). A 16 atom conventional cell composed of 8 Co atoms, 4 Fe atoms and 4 Si/Ge atoms was used to represent $Co_2Fe(Ge_{1-x}Si_x)$ alloys. The Ge and Si admixture was modeled by replacing each Ge by a Si atom. Lattice constant value obtained from X-ray diffraction studies was used throughout the calculations. 12.5% DO_3 disorder was incorporated by swapping one Co atom with one Fe atom. This is the minimum possible amount of disorder that can be incorporated, given the

size of the unit cell used. In what follows, all calculations are done with such DO_3 disordered unit cell configurations.

Total magnetic moment obtained from calculations using GGA is given in Table 3.2. We can see that these values are less than those predicted by S-P rule as well as those determined from experiments. This shows that the electron-electron correlations in these alloys are inadequately described by GGA. Hence, we used the GGA+U approximation as implemented by Dudarev et. al [SLDU98a]. In this implementation, the strong electron-electron correlation is modeled by an effective parameter $U_{eff} = U - J$, where U stands for the onsite Coulomb interaction and J is Hund's rule coupling parameter. The choice of U_{eff} is crucial to address the physics of these systems properly. We have studied the variation in the magnetic moments as a function of U_{eff} before arriving at a single U_{eff} for use in all calculations. We found that variation in U_{eff} had no significant effect on magnetization for any of the alloy compositions when $L2_1$ order was considered. However, upon introduction of DO_3 disorder, the effect on the magnetic moment was significant. This is due to changes in environments associated with magnetic atoms at both tetrahedral and octahedral sites. It is expected that U_{eff} will change with variation in the composition of the alloys and U_{eff} for the same atom would be different when the atoms would occupy sites with different symmetry. Since computation of U_{eff} for each atom at different sites and different x would be very demanding and the choice of a single U_{eff} enables us to understand the role of other factors in analyzing the trends in properties, we chose a fixed U_{eff} (= 3 eV) after several trials.

We first compare the calculated magnetic moments tabulated in Table 3.2 with the experimental M_s of the corresponding alloy compositions. The total magnetic moment calculated using GGA+U for $L2_1$ structure is $6\mu_B$ for all alloys which is in accordance with S-P rule and consistent with other theoretical results [ZGER07a, LGUA10a]. Upon

introduction of DO_3 disorder, the magnetic moment decreases for all alloys except for $x = 0$, as observed in the magnetization measurements. Thus, the DFT calculations yield results which have excellent qualitative agreement with the measured M_s values. However unlike M_s values, the calculated moments remain constant for $x = 0.25, 0.5, 0.75$. There can be more than one reason for this, such as a variation in the percentage of DO_3 disorder, a combination of disorders, or choice of a constant U_{eff}.

Table 3.3: Calculated magnetic moments of $Co_2Fe(Ge_{1-x}Si_x)$ alloys with DO_3 disorder. The corresponding magnetic moments of alloys with $L2_1$ structure are given in parentheses.

x (μ_B)	Ge (μ_B)	Si (μ_B)	Fe@TS (μ_B)	Fe (μ_B)	Co@OS (μ_B)	Co (μ_B)	*Total* (μ_B)
0	-0.052	---	2.558	3.155	2.200	1.149	6.00
	(-0.047)	---	(0.0)	(3.196)	(0.0)	(1.491)	(6.00)
0.25	-0.090	-0.041	2.310	3.096	1.936	1.356	5.50
	(-0.047)	(-0.012)	(0.0)	(3.201)	(0.0)	(1.491)	(6.00)
0.50	-0.088	-0.041	2.286	3.094	1.947	1.356	5.50
	(-0.045)	(-0.011)	(0.0)	(3.202)	(0.0)	(1.488)	(6.00)
0.75	-0.089	-0.041	2.250	3.101	1.942	1.360	5.50
	(-0.043)	(-0.010)	(0.0)	(3.204)	(0.0)	(1.486)	(6.00)
1.0	---	-0.041	2.174	3.092	1.910	1.350	5.35
	---	(-0.010)	(0.0)	(3.208)	(0.0)	(1.487)	(6.00)

Upon achieving a qualitative understanding of the variation of M_s with x through the introduction of DO_3 disorder in the system, we now proceed to analyze the results further. To this end, we first look at the partial magnetic moments in $L2_1$ and DO_3 structures given in Table 3.3. For the $L2_1$ structure, the constant magnetic moment across the compositions is the outcome of the uniform Fe moments of ~3.2μ_B and uniform Co moment of ~1.48μ_B. Introduction of DO_3 disorder breaks such uniformity. While the Co atom at its original tetrahedral site (TS) and the Fe at its original octahedral site (OS) in $L2_1$ structures lose their

moments only slightly when subjected to DO_3 disorder, Fe at the TS loses substantially while Co at the OS gains significantly. The overall result is a reduction in the net moment as x increases. For the alloy with $x = 0$, various gains and loses cancel each other maintaining the total moment at $6\mu_B$. With an increase in x, the Fe moment loss at TS increases substantially, bringing in a reduction of net magnetic moment.

In order to understand the origin of such variations in the partial magnetic moments and to connect it to the half-metallicity observed, we now inspect the electronic structure of $Co_2Fe(Ge_{1-x}Si_x)$ alloys. In Figure 3.5 and Figure 3.6, we present the total and atom projected densities of states of $L2_1$ and DO_3 structures, respectively. In order to understand the trends, we have shown the results for $x = 0$, 0.5 (0.75) and 1.0 of $L2_1$ (DO_3) structures. As expected, for $L2_1$ structure, DOS of each alloy composition exhibit a half-metallic gap. The bottom of the conduction band is due to the Fe t_{2g} states and the top of the valence band is due to Co t_{2g} states for all compositions. This is in contrast to the picture that half-metallic gap in Co_2YZ full Heusler alloy originates from non-bonding Co e_u and t_{1u} states near the Fermi level as exemplified by the electronic structure of Co_2MnSi/Ge [SKHO09a, SWUR05a]. For all compositions, the majority band is completely full, while minority band is partially filled. For these alloys, there are 18 completely occupied majority states and 12 occupied minority states giving rise to a moment of $6\mu_B$. Among the 12 electrons in minority bands, 4 are accommodated in unfilled *p* orbitals of Si/Ge and rest 8 in Co/Fe *d* orbitals. As there are altogether 15 *d* states due to 3 magnetic atoms, 7 *d* states are empty in the minority band. This can be made out from the significant densities of states in the unoccupied parts of the minority bands. This interpretation is consistent with the generalized picture of band filling in full Heusler half-metals [IGAL02a].

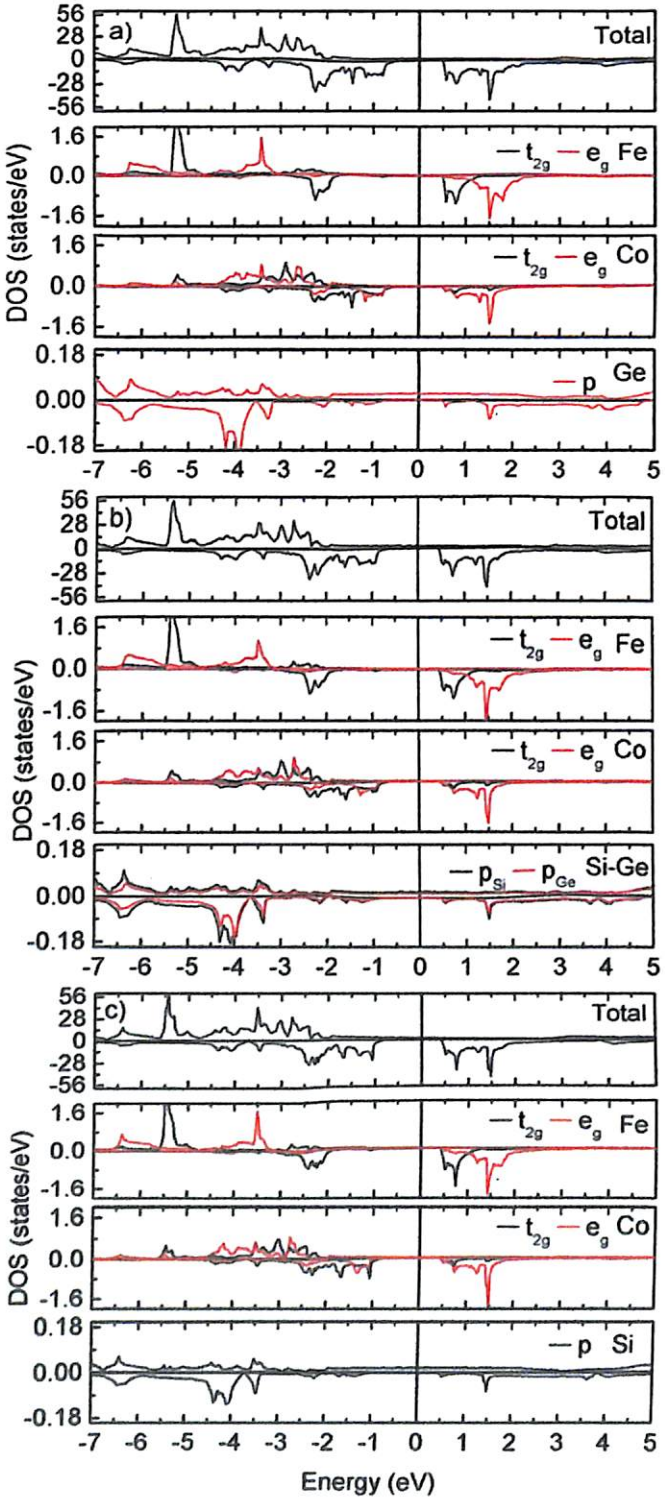

Figure 3.5: Total density of states (DOS) and atom projected density of states (PDOS) for $L2_1$ structure of $Co_2Fe(Ge_{1-x}Si_x)$ alloys with (a) $x = 0.0$, (b) $x = 0.5$ and (c) $x = 1.0$.

We now try to understand the effect of atomic substitution at the non-magnetic sub-lattice. With increase in Ge concentration, we see that the minority spin bands of both Fe

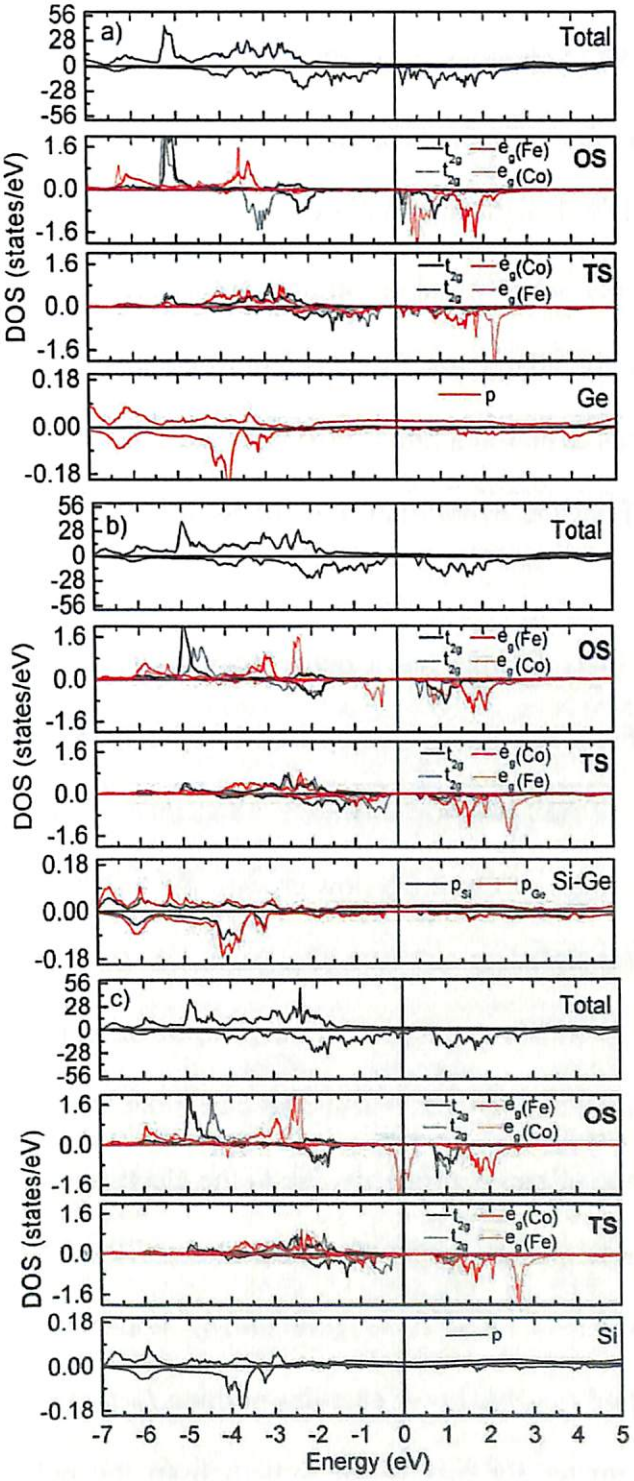

Figure 3.6: Total density of states (DOS) and atom projected density of states (PDOS) for DO_3 disordered $Co_2Fe(Ge_{1-x}Si_x)$ alloys with (a) $x = 0.0$, (b) $x = 0.75$ and (c) $x = 1.0$. (OS and TS denotes octahedral sites and tetrahedral sites, respectively)

and Co start moving towards E_F. We see that the p peaks of Ge atoms start appearing at lower energies. Since Ge $4p$ orbitals are bigger in size, they easily hybridize with Co atoms,

thus filling the states up to higher energies. The effect can be seen in the broadening of the Co e_g states near E_F as Ge content increases. That the introduction of Ge enhances *p-d* hybridization of Co and Ge is indicated in the variation in the number of electrons gained or lost by these two atoms with variation in the compositions (*c.f.* Table 3.4). As Ge concentration increases, the charge lost by Fe is almost equally shared by Co and Ge. Thus, substitution certainly has a non-negligible effect on the electronic structure of this alloy, though this does not affect the overall half-metallicity and the S-P rule prediction of total magnetic moment.

Introduction of DO_3 disorder has a rather dramatic effect on the electronic structure and half-metallicity. This is maximally demonstrated in the DOS of Co_2FeSi (Figure 3.6(c)). Hence, we see a loss of half-metallic character altogether for this alloy. The top of the valence band due to e_g states of Co at OS now crosses E_F. This feature can be understood in the following way: Upon replacing one Fe with a Co at OS, the average number of electrons at OS increases and so E_F falls into the peak of the DOS of Co at OS, which carries this extra electron. With replacement of Si by Ge, half-metallicity is restored.

The re-emergence of gap is primarily due to the electronic states of Co at OS. The e_g states of Co at OS are now pushed inside the valence band. Thus, the top of the valence band is now due to the t_{2g} states of Fe at TS (Figure 3.6(b)). When the Ge content is 100%, the minority states are pushed towards lower energies pushing E_F to the bottom of the conduction band, thus providing greater stability to the system from the point of view of spintronic applications. That the presence of Ge stabilizes the half-metallic states can be further understood in the following way: Re-emergence of half-metallicity with replacement of Si by Ge is due to the emergence of significant vacant e_g states of Co at OS and their positioning at relatively higher energies. According to crystal field theory, in an octahedral environment, e_g

states are easily destabilized as they point directly towards surrounding ions. A look at the DOS at OS and recalling the number of t_{2g} and e_g electrons in minority bands (not shown here) tells us that with Ge substitution, the e_g states of Co at OS decreases substantially and remain more or less constant as long as Si is present in the system. When Si is completely substituted with Ge, the Co e_g levels associated with OS deplete rapidly and t_{2g} levels get populated. So, the addition of Ge stabilizes the t_{2g} orbitals by populating them at the expense of e_g electrons. This must be happening due to the stronger crystal field of Ge in comparison to that of Si.

Table 3.4: Number of electrons in units of charge, lost (-) or gained (+) by an atom in the alloy with respect to the free atom for various $Co_2Fe(Ge_{1-x}Si_x)$ alloys with DO_3 disorder. The corresponding charge lost (-) or gained (+) by an atom in the alloy with respect to the free atom in $L2_1$ structure is given in parentheses.

x	Ge	Si	Fe@TS	Fe	Co@OS	Co
0	0.184	---	-0.164	-0.464	-0.261	0.154
	(0.158)	---	(0.0)	(-0.493)	(0.0)	(0.169)
0.25	0.118	0.054	-0.098	-0.466	-0.168	0.180
	(0.163)	(0.070)	(0.0)	(-0.497)	(0.0)	(0.178)
0.50	0.118	0.031	-0.066	-0.476	-0.209	0.201
	(0.162)	(0.058)	(0.0)	(-0.507)	(0.0)	(0.198)
0.75	0.082	0.035	-0.038	-0.490	-0.202	0.218
	(0.156)	(0.056)	(0.0)	(-0.516)	(0.0)	(0.217)
1.0	---	0.010	0.013	-0.495	-0.124	0.230
	---	(0.054)	(0.0)	(-0.523)	(0.0)	(0.234)

Variations in the site projected magnetic moments and total magnetic moments in the alloys with DO_3 disorder can now be explained in the light of the electronic structures. Here, we see that the Fe moment at OS remains more or less constant throughout the composition range and remains close to its value in $L2_1$ structure. On the other hand, the magnetic moment of Fe at TS reduces considerably. Such reduction is due to the redistribution of electronic

states among majority and minority bands. From the DOS of Fe at TS, one can see that majority bands are full and the e_g minority bands are half-filled, allowing a weaker magnetic exchange splitting in comparison to the Fe at OS. The numbers quoted in Table 3.4 also show that this Fe atom almost neither gains nor loses any electron in the alloy environment and thus its moment is like that of atomic Fe for most of the compositions. However, as Ge content increases, we start noticing an increase in the charge transfer at this Fe site which becomes comparable to that of Co at this site when the composition is Si free. Accordingly, the magnetic moment of this Fe at this composition (*i.e.*, $x = 1$) is substantially larger than those at other compositions. This must be happening because of the stronger crystal field of Ge which enhances *p-d* hybridization at TS. The densities of states of Fe at OS and Co at TS are not very different from their counterparts which explain the small differences in their magnetic moments as compared to the ones in $L2_1$ structure. Like the Fe moment at the TS, the Co moment at the OS too changes substantially in comparison to the Co moment at TS. The Co moment at the OS increases to nearly $2\mu_B$ due to redistribution of electrons among e_g and t_{2g} states introducing a stronger exchange field. In the Si free sample, where the e_g minority states are completely vacant at the Co OS, the exchange splitting is the strongest, leading to a Co magnetic moment of $2.2\mu_B$. Since the loss of magnetic moment in Fe at TS is the maximum, the total moment in the sample with DO_3 disorder decreases as Si content is increased. For all compositions except $x = 1$ (*i.e.*, Co_2FeSi alloy), we have found a half-metallic state from DFT calculations in agreement with the experimental results. This discrepancy can be attributed to the amount of DO_3 disorder considered in our calculations. To verify our presumption, we have computed the electronic structure of the unit cell with 6.25% DO_3 disorder using a larger cell of 32 atoms. We found that there is a clear evidence of a half-metallic gap with the total magnetic moment being $5.5\mu_B$ (Figure 3.7). This

qualitatively agrees with the experimental observation and previous theoretical calculation [LGUA10a]. Thus, we are led to believe that half-metallicity can be obtained in all samples even with DO_3 disorder.

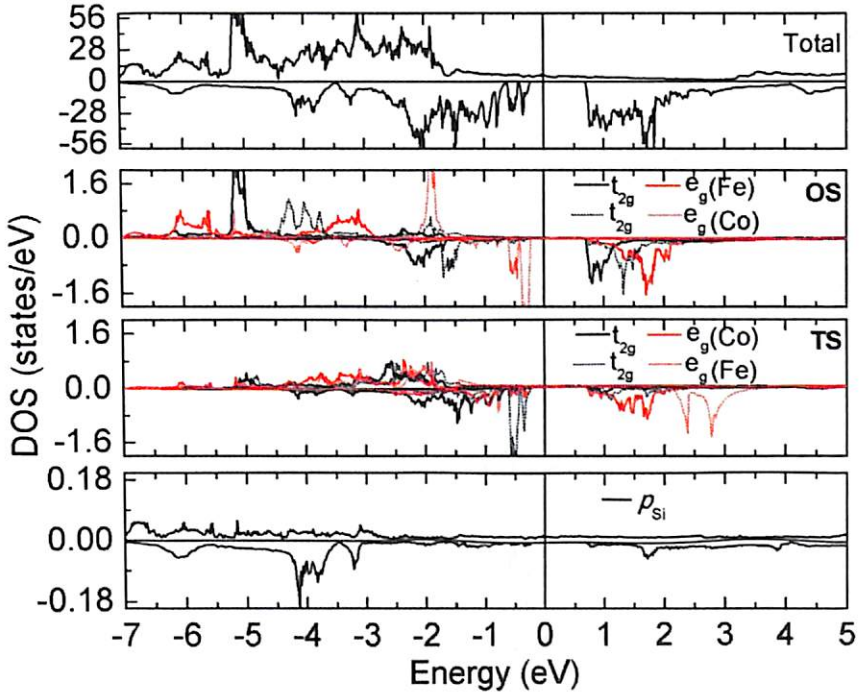

Figure 3.7: Total density of states (DOS) and atom projected density of states (PDOS) calculated for Co_2FeSi with 6.25% DO_3 disorder using GGA+U.

3.3. $Co_2Fe(Ga_{1-x}Si_x)$; $(0 \leq x \leq 1)$ alloys

3.3.1. Crystal structure

Room temperature XRD patterns of $Co_2FeGa_{1-x}Si_x$ are shown in Figure 3.8. They show similar behavior as in the previous series of alloys discussed above. (111) and (200) peaks are absent for the alloys with high Ga concentration. As pointed out earlier, this may be a consequence of similar scattering factors of Co, Fe and Ga. XRD patterns simulated using CaRIne™ software for the corresponding alloy compositions with $L2_1$ structure are also shown in Figure 3.8. The lattice constant *a* obtained from the Rietveld analysis of the alloy compositions with x = 0, 0.25, 0.50, 0.75 and 1.00 are 5.74 Å, 5.71 Å, 5.68 Å, 5.66 Å and

5.63 Å, respectively. The unit cell volume deduced from the lattice constant of each alloy composition is tabulated in Table 3.5. A continuous contraction of lattice and hence the unit cell volume occurs with an increase in x because the atomic radius of Si (= 1.46 Å) is smaller than that of Ga (= 1.81 Å).

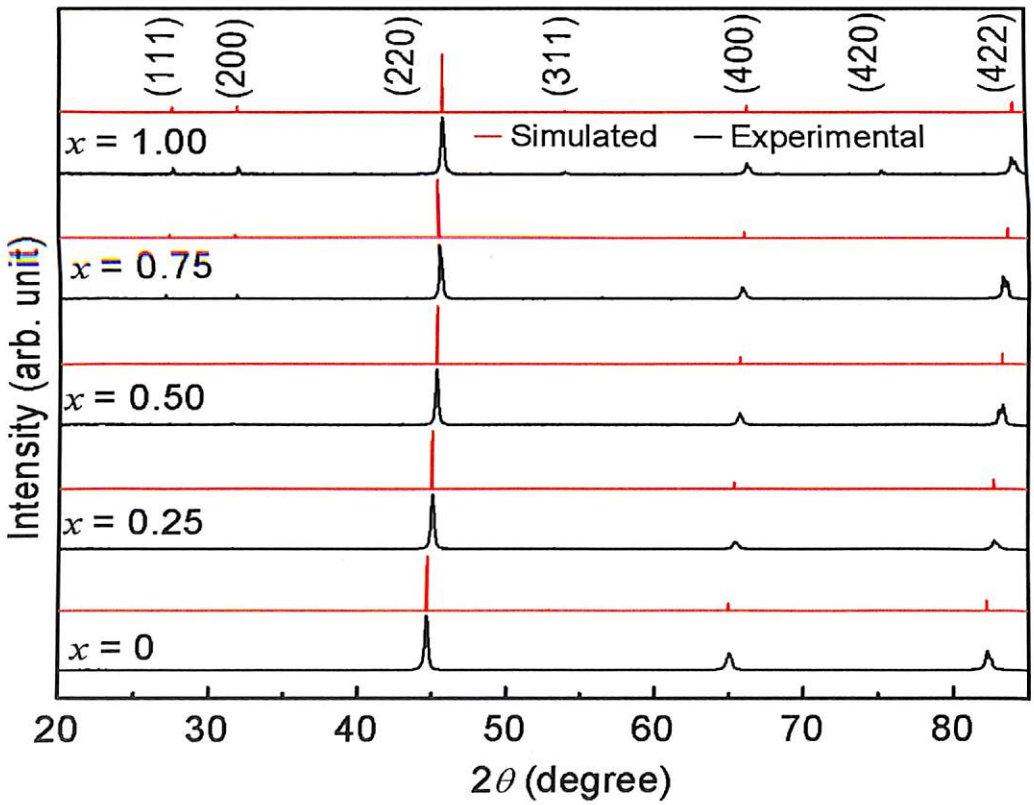

Figure 3.8: Room temperature XRD patterns of $Co_2Fe(Ga_{1-x}Si_x)$ ($0 \leq x \leq 1$) alloys. Simulated XRD patterns for the alloys with $L2_1$ structure are also shown for comparison.

3.3.2. Magnetic properties

Saturation magnetization (M_s) obtained from room temperature initial magnetization (M-H) curves shown in Figure 3.9(a) for the alloys with x = 0, 0.25, 0.50, 0.75 and 1.00 are 5.05μ_B, 5.23μ_B, 5.49μ_B, 5.44μ_B and 5.42μ_B, respectively. Comparison with data in Table 3.6 shows

that the alloys with $x = 0$, 0.25 and 0.50 follow the S-P rule. However, M_s of the alloys with $x = 0.75$ and $x = 1.00$ are lower than the value predicted by the S-P rule. Figure 3.9 (b) depicts the full M-H loops of the alloys recorded at 300 K.

Table 3.5: Nominal composition, measured composition, lattice parameter, unit-cell volume and Bragg factor R_B of Rietveld refinement of $Co_2FeGa_{1-x}Si_x$ $(0 \leq x \leq 1)$ alloys.

Alloy ID	Nominal Composition	Measured Composition	a (Å)	Unit-cell volume (Å^3)	R_B
$x = 0$	Co_2FeGa	$Co_{2.01}Fe_{0.99}Ga$	5.74	189.12	8.1
$x = 0.25$	$Co_2FeGa_{0.75}Si_{0.25}$	$Co_2FeGa_{0.75}Si_{0.25}$	5.71	186.17	7.6
$x = 0.50$	$Co_2FeGa_{0.50}Si_{0.50}$	$Co_2FeGa_{0.51}Si_{0.49}$	5.68	183.25	6.3
$x = 0.75$	$Co_2FeGa_{0.25}Si_{0.75}$	$Co_{1.98}FeGa_{0.26}Si_{0.76}$	5.66	181.32	7.2
$x = 1.00$	Co_2FeSi	$Co_2Fe_{0.99}Si_{1.01}$	5.63	178.45	8.8

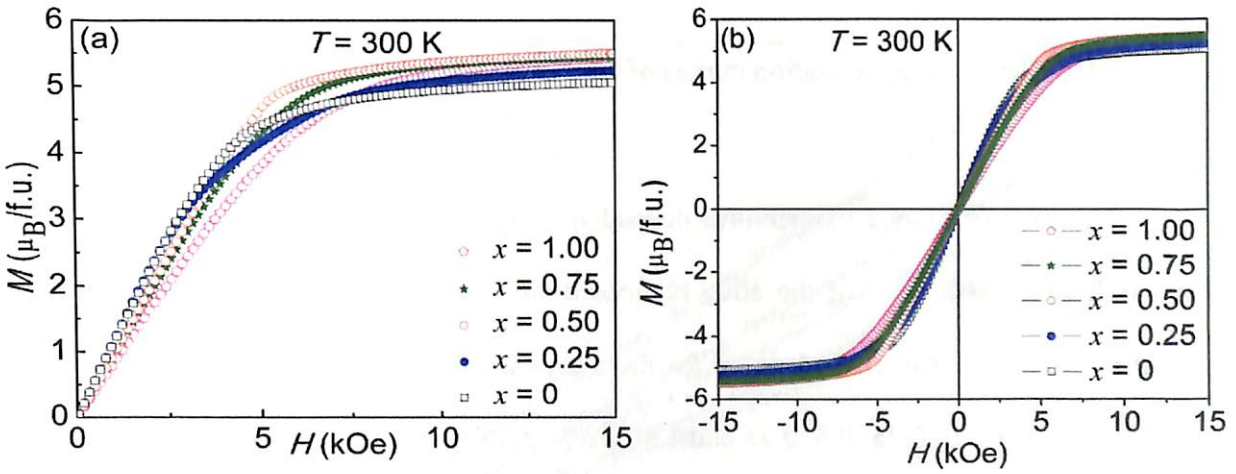

Figure 3.9: (a) Variation of room temperature initial magnetization (M) with applied magnetic field (H) and (b) M-H loops of $Co_2FeGa_{1-x}Si_x$ alloys.

Ab initio studies would be performed to understand why the M_s of alloys with $x > 0.5$ does not follow the S-P despite the high $L2_1$ order exhibited by all the alloys. K_{eff} value for

the alloys was calculated from the *M-H* data depicted in Figure 3.9(a) and summarized in Table 3.6. K_{eff} increases from 6.54×10^5 Jm^{-3} to 11.17×10^5 Jm^{-3} as x is increased from 0 to 1.00. In this series too, an increase in K_{eff} is observed as x is increased from 0 to 1.0 which shows that the magnetic anisotropy increases with Si substitution in this Heusler compound.

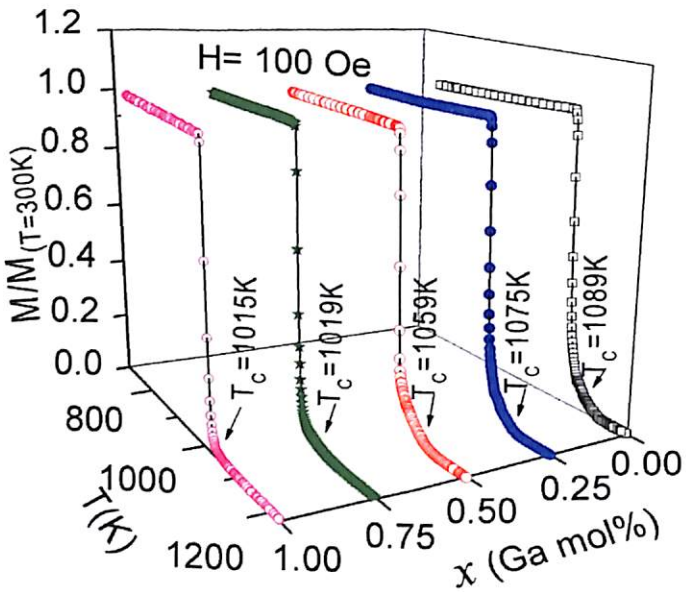

Figure 3.10: Thermo-magnetization curves of $Co_2Fe(Ga_{1-x}Si_x)$ alloys recorded at 100 Oe.

Figure 3.10 shows temperature dependent magnetization measurements made at an applied field of 100 Oe. All the alloy compositions show high Curie temperature (T_C) as expected for these alloys. T_C obtained for the alloys was 1089 K, 1075 K, 1059 K, 1019 K and 1015 K for $x = 0$, 0.25, 0.5, 0.75 and 1.00, respectively. The observed decrease in T_C with Si substitution for Ga in Co_2FeGa compound shows that ferromagnetic ordering decreases with Si substitution. However, high T_C obtained for all the samples shows that all the alloys are strongly ferromagnetic.

A plot of inverse magnetic susceptibility (χ^{-1}) versus temperature for $T > T_C$ for all the alloys are presented in Figure 3.11. Rhodes-Wohlfarth (R-W) ratio (p_c/p_s) calculated for the

alloys are less than unity as depicted in Table 3.6 which indicate that all $Co_2Fe(Ga_{1-x}Si_x)$ alloy compositions are half-metallic. DOS near E_F would be examined in order to ascertain the half-metallic nature of these alloys.

Table 3.6: Saturation magnetic moment (M_s), M_t calculated using nominal composition (M_{Nom}) and EDS measured composition (M_{EDS}), effective anisotropy constant (K_{eff}) and effective moment per magnetic atom (p_c) and p_c/p_s of $Co_2Fe(Ga_{1-x}Si_x)$ alloys. Total magnetic moment (M_{th}) obtained for $L2_1$ structure from *ab initio* calculations (using GGA and GGA+U) are also mentioned.

x	M_s (μ_B)	M_{Nom} / M_{EDS} (μ_B)	K_{eff} ($\times 10^5$ Jm^{-3})	p_c (μ_B)	p_c/p_s	M_{th} (GGA) μ_B	M_{th} (GGA+U) μ_B
0	5.05	5.00 / 5.01	6.54	3.69	0.73	**5.02**	5.32
0.25	5.23	5.25 / 5.25	7.92	4.07	0.78	**5.24**	5.29
0.50	5.49	5.50 / 5.49	9.63	4.30	0.78	5.41	**5.50**
0.75	5.44	5.75 / 5.64	10.06	4.53	0.83	5.50	**5.75**
1.00	5.42	6.00 / 5.96	11.17	4.74	0.86	5.49	**6.00**

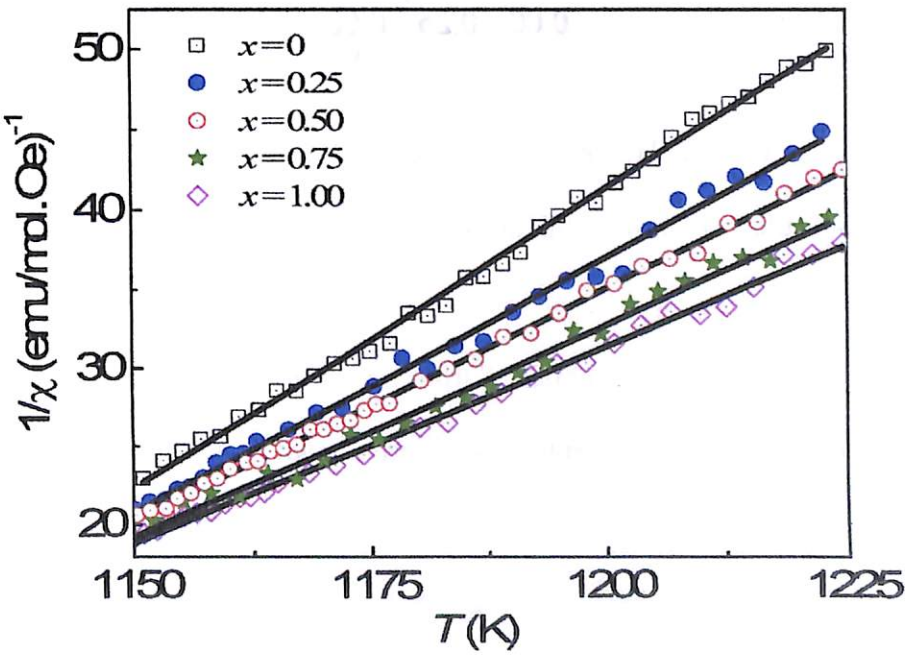

Figure 3.11: Inverse magnetic susceptibility (χ^{-1}) as a function of temperature (T) of $Co_2Fe(Ga_{1-x}Si_x)$ alloys for $T > T_C$.

3.3.3. *Ab initio* calculations

Ab initio calculations using both GGA and GGA+*U* as discussed in the previous section, would also be carried out for the $Co_2Fe(Ga_{1-x}Si_x)$ alloys to investigate their half-metallic behavior and deviation of magnetic moments from S-P rule. Since *ab initio* studies presented in section 3.2.3 show that DO_3 disorder in Co_2FeSi can induce the observed deviation of M_s from the value predicted by S-P rule, the effect of DO_3 disorder on the magnetic moment and half-metallic character of $Co_2Fe(Ga_{1-x}Si_x)$ alloys has also been investigated.

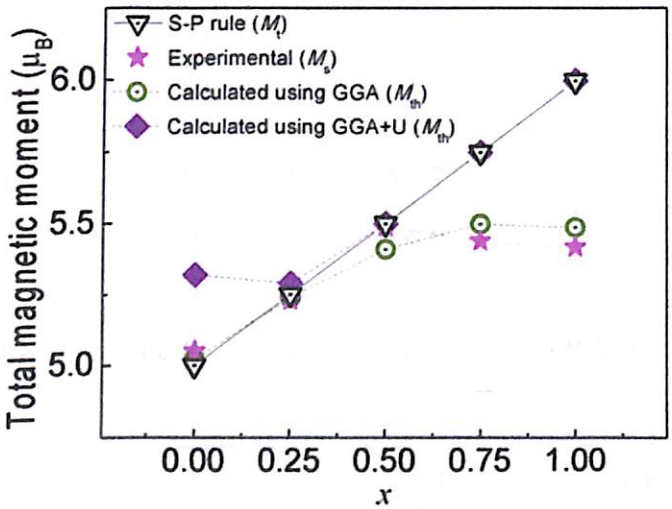

Figure 3.12: M_s, M_t and M_{th} obtained for $Co_2FeGa_{1-x}Si_x$ alloys as a function of x from experiment, S-P rule, *ab initio* calculations using GGA and GGA+U.

Total magnetic moment obtained from *ab initio* calculation with GGA and GGA+*U* along with the reported experimental results are shown in Figure 3.12 and Table 3.6. The values predicted by S-P rule are also shown in the figure. It can be seen from the figure that the total moment calculated using GGA agrees well with both experiment and S-P rule values for alloy compositions with $x < 0.5$ whereas, and the moments of these alloys get overestimated with the inclusion of *U*. However for alloys with $x \geq 0.5$, the moment obtained

using GGA is lower than the one predicted by the S-P rule which get corrected by the inclusion of on-site Coulomb exchange parameter. Therefore, unlike the previous series of alloys, the electron-electron correlation changes drastically with increase in x in $Co_2Fe(Ga_{1-x}Si_x)$ alloys. Effect of U on magnetic moment as well as half-metallic properties with increase in x has been studied in detail for this series of alloys.

In Figures 3.13 and 3.14, we have depicted the total and atom resolved density of states (DOS) obtained using GGA (black curves) and GGA+U (red curves) for Co_2FeZ compound with Z = Ga and Si, respectively. It is evident that for Z = Ga, the Fermi level touches the top of the valence band for Co t_{2g} state, but still retains a high degree of spin polarization as indicated by the total DOS calculated using GGA. PCAR studies performed on this alloy revealed an intrinsic spin polarization of 59%, which shows its half-metallic character [MZHA04a]. In the case of Co_2FeSi with 30 valance electrons, the extra electrons occupy majority states. This leads to a larger exchange splitting between occupied majority and unoccupied minority states resulting in larger gap width for the compound with Z = Si as compared to Z = Ga. However, half-metallicity is destroyed in Co_2FeSi mainly because of Co and Fe e_g states. The occupied majority Fe states lies very deep in energy which in turn shifts the unoccupied Fe states to lower energies and making it to cross the Fermi level. Hence, the deviation in the calculated value from the S-P rule for this alloy can be correlated with the loss of half-metallic character as the gap lies below E_F. Wurmehl *et al.* [SWUR05a] have suggested that if we take into account onsite correlation between the *d* electrons, this discrepancy can be resolved. Accordingly, the total magnetic moment was found out to be $6.0\mu_B$ (Figure 3.12)using GGA+U approximation and the presence of a half-metallic gap could be clearly seen in the calculated DOS (Figure 3.14). So, it appears that this integer value of the moment is related to the minority gap. Since the number of filled minority states

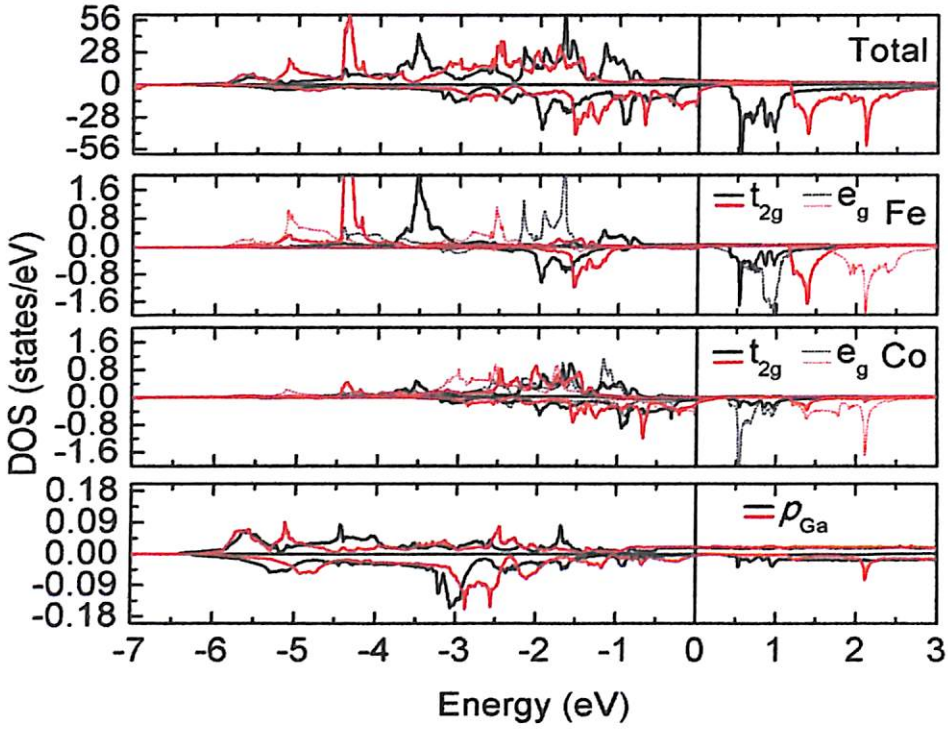

Figure 3.13: Total DOS and atom PDOS calculated using GGA (black curves) and GGA+U (red curves) for Co_2FeGa with $L2_1$ structure.

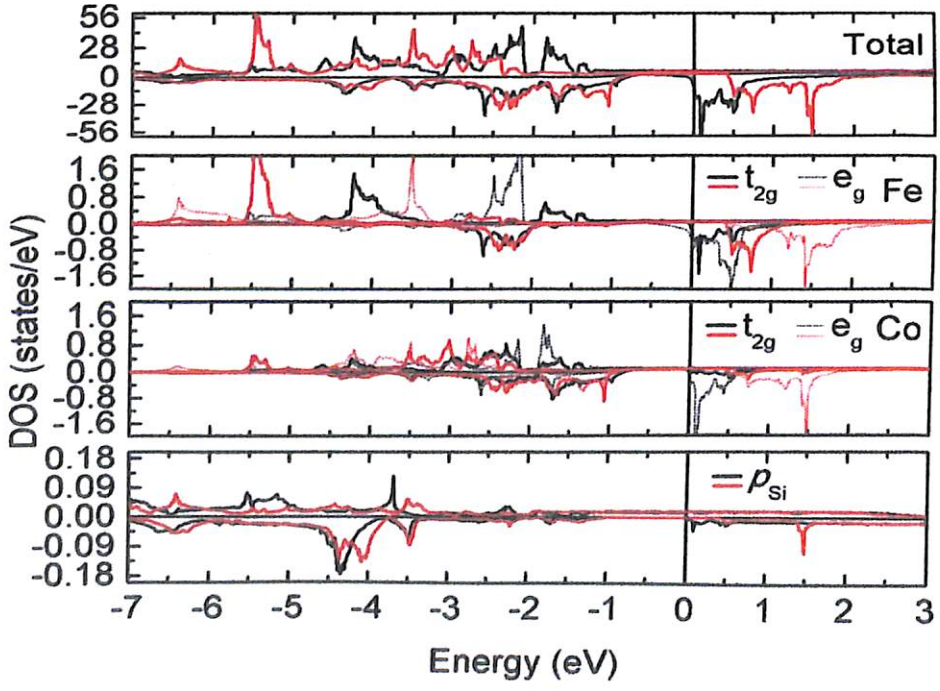

Figure 3.14: Total DOS and atom PDOS calculated using GGA (black curves) and GGA+U (red curves) for Co_2FeSi with $L2_1$ structure.

is an integer, it also ensures the magnetic moment to be an integer. With the introduction of *U*, both Co and Fe moments increase, thereby increasing the total moment as illustrated in Table 3.7. Co moment interacts more strongly than Fe moment as indicated by the larger increase in Co moment ($0.166\mu_B$) as compared to $0.016\mu_B$ increase in Fe moment. From the DOS shown in Figure 3.14, it is evident that the majority states arising from t_{2g} states around -4 eV get shifted to -6 eV below Fermi level on introduction of *U*. The unoccupied minority e_g states exhibit a larger shift of 1.5 eV above Fermi level as compared to t_{2g} states (0.5 eV above Fermi level). Similarly, the occupied states of the minority DOS move towards the Fermi level. As a consequence, the minority gap becomes considerably larger with Fermi energy lying inside the gap. On the other hand, when GGA+*U* approximation was used for Co_2FeGa with same U_{eff} value, the total moment was found to be $5.35\mu_B$ accompanied by the destruction of the half-metallic gap as depicted by the DOS (Figure 3.13). The occupied states of the minority DOS arising from the Co atom crosses E_F, shifting the gap above the E_F and forcing the alloy to lose its half-metallic character.

Table 3.7 Calculated magnetic moments of $Co_2Fe(Ga_{1-x}Si_x)$ alloys with $L2_1$ structure using GGA (corresponding magnetic moments obtained using GGA+U are given in parentheses).

x	Ga	Si	Fe	Co	*Total*
	(μ_B)	(μ_B)	(μ_B)	(μ_B)	(μ_B)
0	-0.072	---	2.781	1.179	5.02
	(-0.156)	---	(3.079)	(1.312)	(5.32)
0.25	-0.061	-0.010	2.818	1.251	5.24
	(-0.152)	(-0.060)	(3.085)	(1.281)	(5.29)
0.50	-0.049	-0.010	2.834	1.306	5.41
	(-0.136	(-0.045)	(3.118)	(1.341)	(5.50)
0.75	-0.041	-0.007	2.834	1.341	5.50
	(-0.116)	(-0.028)	(3.162)	(1.416)	(5.75)
1.0	---	-0.010	2.797	1.345	5.49
	---	(-0.010)	(3.208)	(1.487)	(6.00)

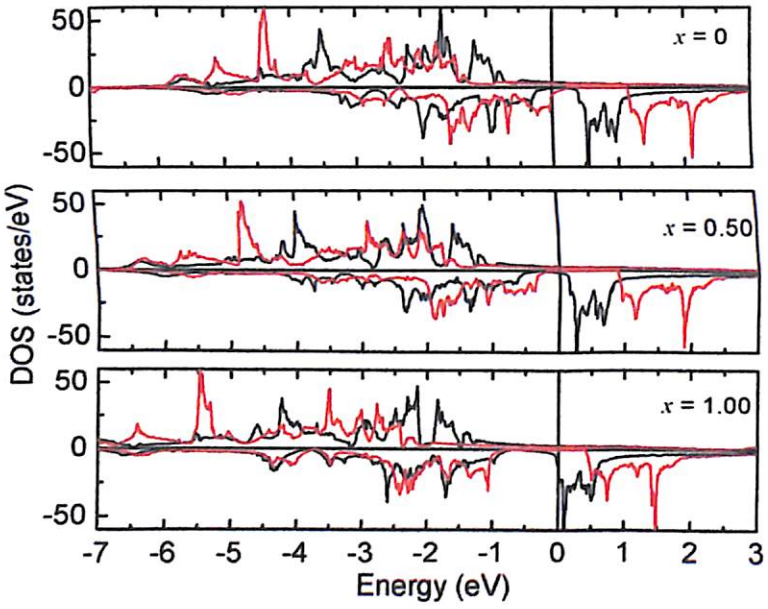

Figure 3.15: Total density of states (DOS) calculated for $L2_1$ structured $Co_2FeGa_{1-x}Si_x$ alloys using GGA (black curves) and GGA+U (red curves) for $x = 0$, 0.50 and 1.00.

Figure 3.15 shows the total DOS of $Co_2FeGa_{1-x}Si_x$ ($x = 0$, 0.50, 1.00) calculated using GGA (black curves) and GGA+U (red curves), respectively. Substitution of Si for Ga provides extra electrons which push the majority states to lower energies accompanied by similar movement in minority states as well. For the alloys with high Si concentration, the unoccupied states just above E_F cannot absorb the extra charge and the system prefers to absorb electron in minority states as well and therefore ends up losing half-metallicity. Similar to the trend observed for the magnetic moments, inclusion of U restores the gap at E_F making the alloys with $x = 0.50$, 0.75 and 1.00 half-metallic. This shows that due to the lesser number of electrons in alloys with high Ga concentration (*i.e.*, $x = 0$ and 0.25), the electron correlation is insignificantly lower and does not contribute much to the total magnetic moment. However, for the rest of the alloys (*i.e.*, $x \geq 0.5$), an increase in the total number of

electrons tends to increase the correlation between them. This forces the use of U factor to correctly describe the magnetic properties of these alloys.

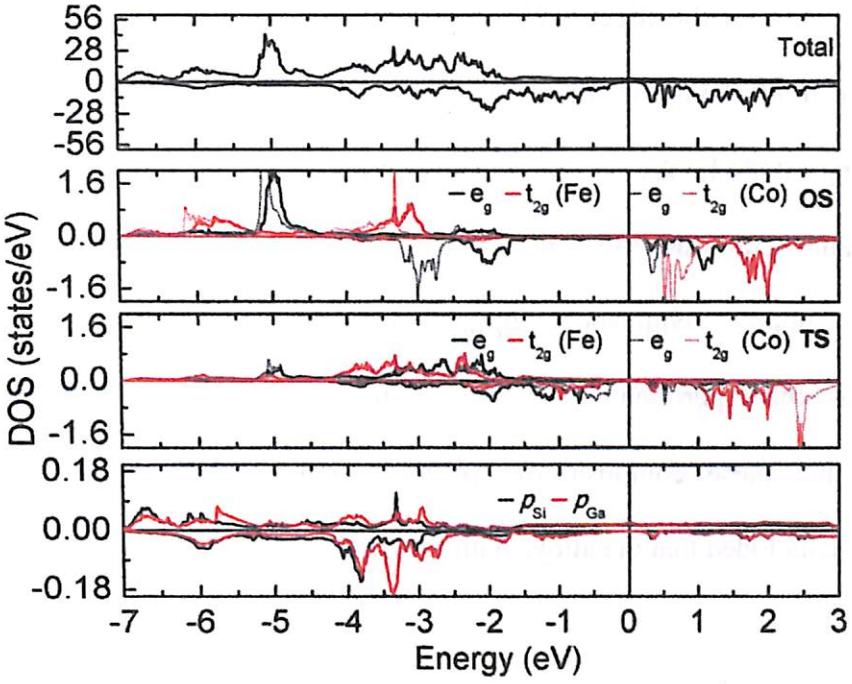

Figure 3.16: Total DOS and atom PDOS of $Co_2Fe(Ga_{0.25}Si_{0.75})$ alloy with 12.5% DO_3 disorder (OS and TS denotes octahedral and tetrahedral sites, respectively) using GGA+U.

Experimentally deduced M_s of alloy with $x = 0.50$ agrees well with the value calculated using GGA+U. But M_s of $x = 0.75$ and $x = 1.00$ alloys deviate from the theoretical results and the prediction of S-P rule. The deviation of M_s for $x = 1$ alloy is attributed to small amount of DO_3 disorder as already discussed in section 3.2.3. However, the scenario is quite different for the alloy with $x = 0.75$ (*cf.* Figure 3.16). In this case, both occupied Co minority and majority states are pushed to a lower energy as compared to $x = 1.0$ alloy. The unoccupied Co minority states are shifted towards E_F. If we compare with the $L2_1$ structure, Fe at TS introduces t_{2g} electronic states in the valance band near E_F. Because of this, the width of the gap decreases without affecting half-metallicity. But, the total magnetic moment remains unchanged from that one expected for a perfect $L2_1$ structure (*i.e.*, $5.75\mu_B$) which is

higher than the experimentally obtained value. There can be more than one reason for this. There can be a combination of disorders or it could be due to our choice of a constant U_{eff} for atoms at both OS and TS. To see the effect of DO_3 disorder with composition (x), 12.5% DO_3 disorder was introduced in all the alloys. Figure 3.17 shows the total DOS of $Co_2FeGa_{1-x}Si_x$ with DO_3 disorder using GGA+U. As can be seen from the figure, the gap in the minority states for x = 0, 0.25 and 0.50 is destroyed in all cases with total magnetic moment of the alloys turning out be 5.66μ_B, 5.69μ_B and 5.56μ_B, respectively. These magnetic moment values are different from the experimentally obtained values. Moreover, R-W ratio of these alloys has indicated that these compositions are half-metallic. Taking all these into consideration, it can be concluded that the alloys with $x \leq 0.50$ are free from DO_3 disorder.

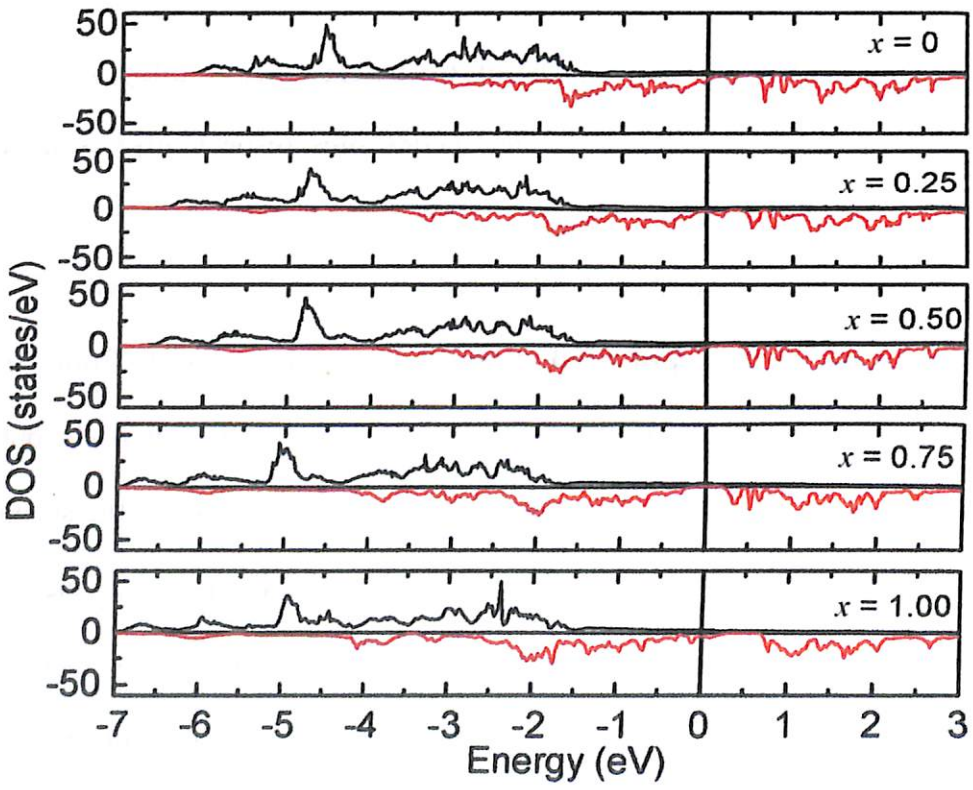

Figure 3.17: Total DOS for $Co_2FeGa_{1-x}Si_x$ alloys with 12.5% DO_3 disorder using GGA+U.

3.4 Summary

In this chapter, structural, magnetic and half-metallic properties of bulk $Co_2Fe(Ge_{1-x}Si_x)$ and $Co_2Fe(Ga_{1-x}Si_x)$ alloys have been investigated. Extensive DFT based *ab initio* calculations have been performed on both alloy systems to evaluate effect of composition, degree of structural order and electron-electron correlations on the total magnetic moment as well as half-metallic character of the alloys. Salient features of these studies are as follows:

1. Co_2FeSi alloy crystallize in $L2_1$ structure but super-lattice peaks are absent in the XRD patterns of the quaternary alloys with high Ge and Ga concentrations.
2. All alloys shows ferromagnetic behavior with very high T_C and high M_s. In the paramagnetic state, temperature dependence of inverse magnetic susceptibility follows the Curie-Weiss law.
3. R-W ratio for $Co_2FeZ_{1-x}Si_x$ (Z = Ge, Ga) alloys reported for the first time, indicates half-metallic character in all the compositions.
4. *Ab initio* calculations reveal the influence of atomic ordering on the properties of the alloys.
5. As Si concentration increases, M_s of the alloys deviate from values predicted by S-P rule. This deviation from the S-P rule can be attributed to the presence of DO_3 disorder in the alloys as revealed by *ab initio* studies.
6. Half-metallicity can be retained in $Co_2FeGe_{1-x}Si_x$ alloys despite the DO_3 disorder and that presence of Ge has a strong stabilization effect in these alloys.
7. $Co_2Fe(Ga_{1-x}Si_x)$ alloys with high Ga concentration can be described well with only GGA. However, with increase in x, on-site Coulomb interactions increase significantly, demanding the need for GGA+U to correctly describe the total magnetic moment and electronic structure of these alloys.

Chapter 4

INVESTIGATIONS ON $Ru_2FeSi_{1-x}Ge_x$ AND $(Ru_{1-x}Co_x)_2FeSi$ ALLOYS

A survey of the literature shows that full Heusler alloys based on 4*d* or 5*d* transition metals have not received as much attention as the alloys containing 3d transition metals. Among these, Ru_2YZ alloys are especially interesting because of the diverse magnetic behavior exhibited by them. For example, Ru_2VGe is paramagnetic [SMIZ10a], Ru_2FeZ (Z = Ge, Sn) [SMIZ09a, VSPA83a] are ferromagnetic, whereas Ru_2MnZ (Z = Si, Ge, Sn, Sb) [SMIZ10a, TKAN06a], Ru_2FeSi [SNMI85a, ASZY89a] and Ru_2CrGe [HOKA08a] exhibit antiferromagnetic nature. Among the quaternary alloys investigated so far, $Ru_{2-x}Fe_xCrGe$ [YKUS07a], $Ru_{2-x}Fe_xCrSi$ [KMAT05a, MHIR07a], $Ru_2Mn_{1-x}Fe_xGe$ [SMIZ09a] and $Ru_2Mn_{1-x}V_xGe$ [SMIZ10a] show ferromagnetic behavior in the composition range of $0.25 \leq x \leq 1.5$, $0.3 \leq x \leq 1.8$, $x = 0.5$, and $0.3 \leq x \leq 0.8$, respectively. $Ru_{2-x}Fe_xCrSi$ alloys with $x \leq 0.2$ show antiferromagnetic transition with a spin wave like behavior and $Ru_2Mn_{0.8}V_{0.2}Ge$ exhibits antiferromagnetic nature.

As discussed in the first chapter, discovery of half-metallicity and the realization of high spin polarization in Co_2MnSi and other full Heusler alloys has induced interest in the development of spin valve based GMR devices using Heusler alloy based electrode layers. However, such spin valves invariably use an Ir-Mn antiferromagnetic layer to pin one of the ferromagnetic layers [KNIK09a, TNNA12a]. Relatively few antiferromagnetic Heusler alloys are known to have sufficiently high Néel temperature (T_N). In the Ru_2MnZ (Z = Sn, Sb, Ge, Si) the Mn moments couple ferromagnetically within the (111) layers and antiferromagnetically with the adjacent (111) layers forming a so-called 2nd kind of antiferromagnetic structure. T_N of Ru_2MnSi and Ru_2MnGe compounds are slightly above room temperature (313 K [TKAN06a] and 316 K [TKAN06a], respectively). Ru_2MnSn has somewhat lower ordering temperature (T_N =296 K) [TKAN06a], which is just above room

temperature. Similarly, Ru_2FeSi is also antiferromagnetic near room temperature with T_N of 280 K [SNMI85a].

Therefore, it is possible to obtain alloy compositions exhibiting ferromagnetic or antiferromagnetic properties in $Ru_2Y(Z_{1-x}Z'_x)$ and $(Ru_{1-x}X'_x)_2YZ$ alloys by properly choosing the fourth element (X′ or Z′) and its quantity. This could possibly lead to the realization of an all Heusler spin valve with superior interfacial properties using alloys from these quaternary systems. An understanding of the crystallographic and magnetic properties of quaternary $Ru_2Y(Z_{1-x}Z'_x)$ and $(Ru_{1-x}X'_x)_2YZ$ alloys is the first step in this direction. In this chapter, crystallographic and magnetic properties of quaternary $Ru_2Fe(Si_{1-x}Ge_x)$ and $(Ru_{1-x}Co_x)_2FeSi$ alloys with $0 \leq x \leq 1$ are reported.

4.1. Preparation of alloys

Polycrystalline $Ru_2FeSi_{1-x}Ge_x$ and $(Ru_{1-x}Co_x)_2FeSi$ ($0 \leq x \leq 1$) alloy ingots were prepared by arc melting high purity elements followed by homogenization at 1173 K for 24 h and quenching in ice + water mixture as described in the second chapter. The overall composition of the two series of alloys was determined by EDS analysis to be within 1% of the nominal composition. Table 4.1 and Table 4.3 present the nominal and measured overall compositions of the processed $Ru_2FeSi_{1-x}Ge_x$ and $(Ru_{1-x}Co_x)_2FeSi$ ($0 \leq x \leq 1$) alloy, respectively.

4.2. $Ru_2FeSi_{1-x}Ge_x$ ($0 \leq x \leq 1$) alloys

4.2.1. Crystal Structure

Room temperature XRD patterns of $Ru_2Fe(Si_{1-x}Ge_x)$ alloys are shown in Figure 4.1. Absence of peaks with all odd indices in the XRD patterns indicates a transition of the $L2_1$ structure into B2 structure due to intermixing of Y and Z elements in all the alloys. However, since Fe and Ge are from the same period with nearly equal scattering factors, the

(111) peak is absent even in the theoretically generated XRD pattern for alloys with high Ge. Although simulated XRD pattern for the alloy with $x = 0.25$ shows the (111) peak, its intensity is very small. Experimental XRD patterns were refined by Rietveld method using FullProf 2.00 software. The lattice constant a obtained from the Rietveld analysis of the cubic samples with $x = 0$, 0.25, 0.50, 0.75 and 1.00 are 5.88 Å, 5.90 Å, 5.93 Å, 5.94 Å and 5.97Å, respectively. Lattice constant increases with an increase in x because the atomic radius of Si (= 1.46 Å) is smaller than that of Ge (= 1.52 Å).

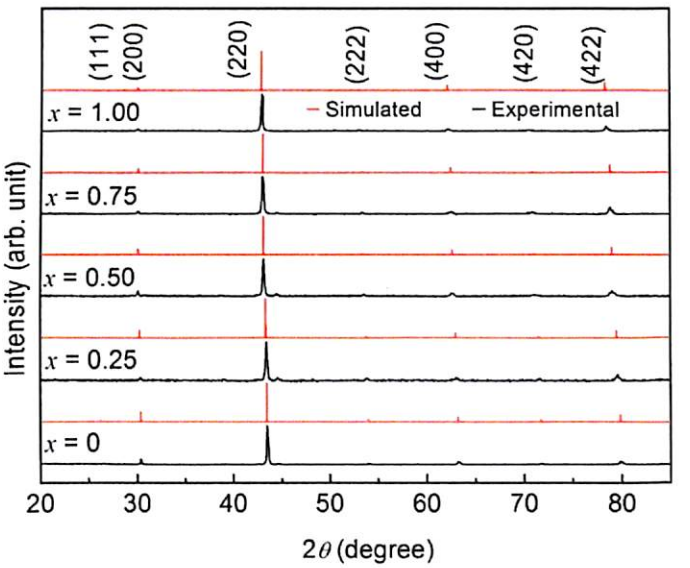

Figure 4.1: Room temperature XRD patterns of $Ru_2Fe(Si_{1-x}Ge_x)$ $(0 \leq x \leq 1)$ alloys. Simulated XRD patterns for the alloys with $L2_1$ structure are also shown for comparison.

Table 4.1: Nominal composition, measured composition, lattice parameter, unit-cell volume, Bragg factor R_B of Rietveld refinement, of $Ru_2FeSi_{1-x}Ge_x$ $(0 \leq x \leq 1)$ alloys.

Alloy ID	Nominal Composition	Measured Composition	a (Å)	Unit-cell volume (Å^3)	R_B
$x = 0$	Ru_2FeSi	$Ru_{1.99}FeSi_{1.01}$	5.88	203.30	7.0
$x = 0.25$	$Ru_2FeSi_{0.75}Ge_{0.25}$	$Ru_2FeSi_{0.75}Ge_{0.25}$	5.90	205.38	8.1
$x = 0.50$	$Ru_2FeSi_{0.50}Ge_{0.50}$	$Ru_{1.98}FeSi_{0.52}Ge_{0.50}$	5.93	208.53	9.2
$x = 0.75$	$Ru_2FeSi_{0.25}Ge_{0.75}$	$Ru_{1.99}FeSi_{0.25}Ge_{0.76}$	5.94	209.58	6.9
$x = 1.00$	Ru_2FeGe	$Ru_{1.97}Fe_{0.98}Ge_{1.05}$	5.97	212.78	9.1

4.2.2. Magnetic properties

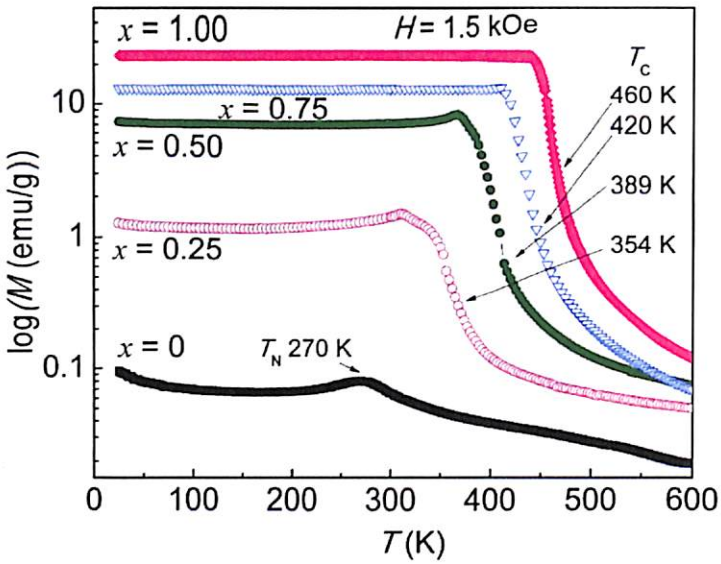

Figure 4.2: Thermo-magnetization curves of $Ru_2Fe(Si_{1-x}Ge_x)$ alloys recorded under 1.5 kOe.

Figure 4.2 shows the thermo-magnetization (M-T) curves for $Ru_2Fe(Si_{1-x}Ge_x)$ alloys recorded under an applied field of 1.5 kOe. The alloy with $x = 0$ (Ru_2FeSi) shows antiferromagnetic behavior with a peak at 270 K which can be identified as its T_N. This value is in close agreement with the value of 280 K in the literature [SNMI85a]. As Ge concentration is increased from $x = 0.25$ to $x = 1.00$, magnetization value starts increasing due to development of ferromagnetic interactions. *Ab initio* studies presented in section 4.2.3 will attempt to describe the appearance of ferromagnetism with Ge substitution in these alloys. The strength of ferromagnnetic interaction increases with increase in x as depicted by the increase in T_C from 354 K to 460 K as x is increased from 0.25 to 1.00 mol%. This is a consequence of the requirement of more thermal energy to nullify the magnetic interaction in the alloys with higher x. Thus, the ferromagnetic state becomes dominant as x is increased in this series of alloys. Variations of T_N and T_C with x are depicted in Figure 4.3. It can also be seen that T_C varies linearly with x from $x = 0.25$ to $x = 1.00$.

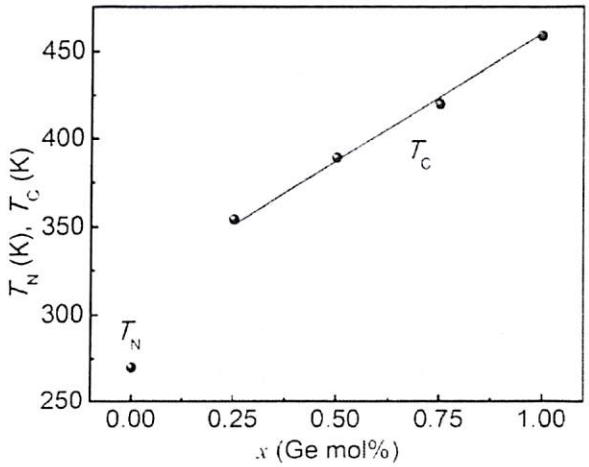

Figure 4.3: Variation of T_N and T_C as a function of Ge (x) content in the quaternary alloys.

Paramagnetic Curie temperature, θ_p was estimated from the inverse susceptibility (χ^{-1}) versus temperature (T) plots (Figure 4.4) as explained in the previous chapters. θ_p for Ru_2FeSi is negative (-32.8 K), which depicts its antiferromagnetic nature. With increased substitution of Ge, θ_p becomes increasingly positive, which indicates the onset and stabilization of ferromagnetism in the samples with increasing x. Rhodes-Wohlfarth (R-W) ratio (p_c/p_s) was estimated from Figure 4.4 using the procedure as described in section 2.3.1. The calculated R-W ratio for all the alloys have value greater than unity as shown in Table 4.2 which indicates that all the alloys lack half-metallicity.

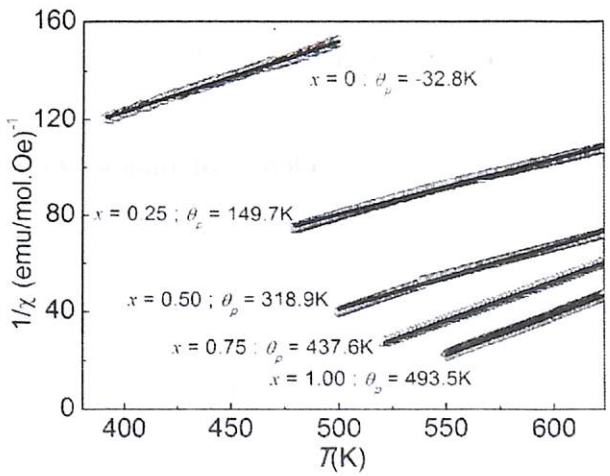

Figure 4.4 Inverse susceptibility (χ^{-1}) versus temperature (T) plots for $Ru_2Fe(Si_{1-x}Ge_x)$ alloys.

Table 4.2. Magnetic moment at an applied field of 10 kOe, effective moment per magnetic atom (p_c), R-W ratio p_c/p_s, and M_t calculated using nominal composition (M_{Nom}) and EDS measured composition (M_{EDS}) for $Ru_2Fe(Si_{1-x}Ge_x)$ alloys. Total magnetic moment (M_{th}) of the alloys with $L2_1$ and B2 structures obtained from *ab initio* calculations are also shown.

x	$M_{10\,kOe}$ (μ_B)	p_c (μ_B)	p_c/p_s	M_{Nom} / M_{EDS} (μ_B)	M_{th} ($L2_1$) (μ_B)	M_{th} (B2) (μ_B)
0	0.03	4.4	-	4.00 / 3.96	3.81	3.60
0.25	0.40	4.8	12	4.00 / 4.00	3.84	3.64
0.50	1.21	4.9	4.04	4.00 / 3.92	3.89	3.69
0.75	2.04	3.7	1.81	4.00 / 3.96	3.88	3.71
1.00	2.69	3.7	1.38	4.00 / 3.80	3.91	3.75

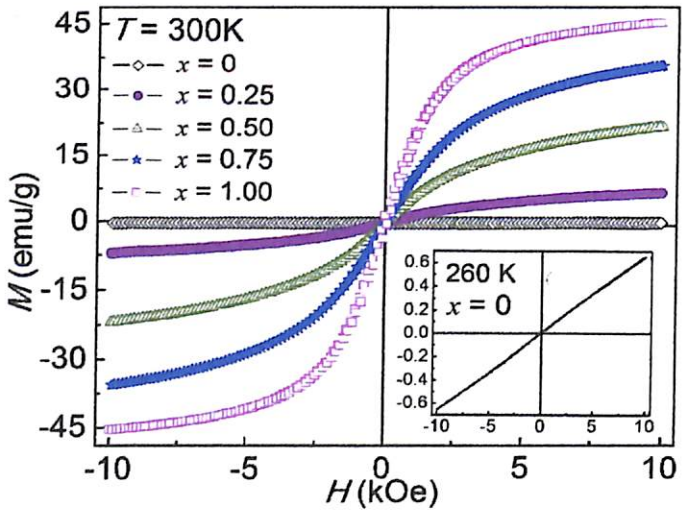

Figure 4.5 Field dependence of magnetization (M-H) of $Ru_2Fe(Si_{1-x}Ge_x)$ alloys at 300 K. Inset shows the M-H curve of the alloy with $x = 0$ below its T_N.

Figure 4.5 shows the field dependence of magnetization (M-H curves) recorded at room temperature for all the alloys. Since $T_N = 270$ K for Ru_2FeSi, M-H loop recorded at 260 K is shown in the inset to illustrate the weak magnetic response exhibited by this alloy in the antiferromagnetic state below T_N. Antiferromagnets are known [TKAN06a] to exhibit a linear response to low applied magnetic fields as depicted in the inset of Figure 4.5. With increase in x, spontaneous magnetization appears in the samples. Magnetization recorded at an applied

field of 10 kOe increases from 0.65 emu/g to 45.43 emu/g as x is increased from 0 to 1.00. Alloys with x = 0.25 to 1.00 show very narrow hysteresis loops typical of soft magnetic materials. Measured coercivity (H_c) was 19.8, 33.3, 65.8, 69.5 Oe, whereas, remanent magnetization (M_r) was 0.03, 0.18, 0.66, 1.43 emu/g for alloys with x = 0.25, 0.5, 0.75 and 1.00, respectively.

4.2.3. *Ab initio* calculations

To investigate the change in magnetic interaction with Ge substitution and the effect of B2 disorder on those interactions, *ab initio* calculations were carried out on $Ru_2Fe(Si_{1-x}Ge_x)$ alloys using GGA. Figure 4.6 shows the variation of the Heisenberg exchange integral (J_{ij}) representing the magnetic interaction between Fe atoms as a function of interatomic distance in units of lattice parameter (a) for $Ru_2Fe(Si_{1-x}Ge_x)$ alloys with fully ordered $L2_1$ structure. Magnetic interaction that was ferromagnetic at 0.71a (*i.e.* $a/\sqrt{2}$), turned antiferromagnetic at 1.0a and the interactions died out at large ($\geq$ 2.25a) interatomic distances.

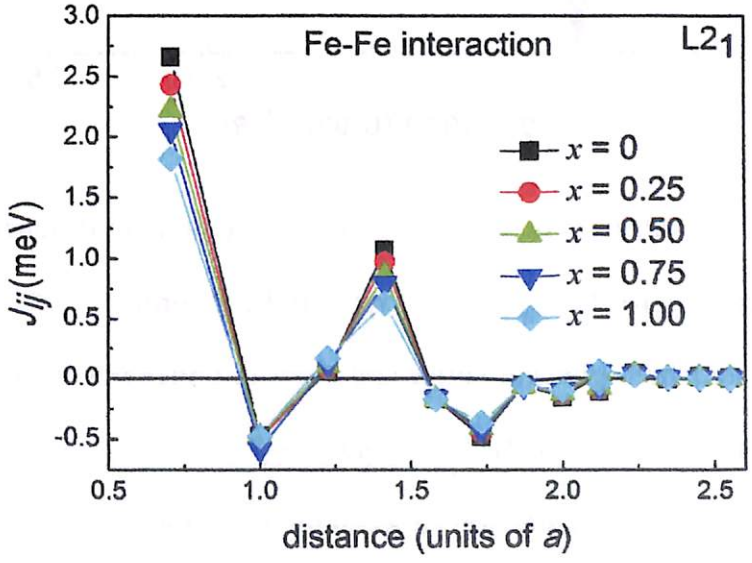

Figure 4.6 Heisenberg exchange integral versus Fe-Fe interatomic distance plots depicting the magnetic interaction in $Ru_2Fe(Si_{1-x}Ge_x)$ alloys with $L2_1$ structure.

This damped oscillatory behavior exhibited by $J_{ij}(a)$ in Figure 4.6 is similar to RKKY type of interaction mediated by *sp* atoms. It can be observed from Figure 4.6 that the first nearest neighbor (NN) magnetic interactions between these atoms is strongly ferromagnetic, leading to ferromagnetism in all the alloys including $x = 0$ alloy. Since this contradicts our experimental results depicted in Figure 4.2 - 4.5 and the B2 structure shown by the XRD pattern of this compound, *ab initio* calculations were carried out on all these alloy compositons by introducing B2 disorder in the $L2_1$ unit cell.

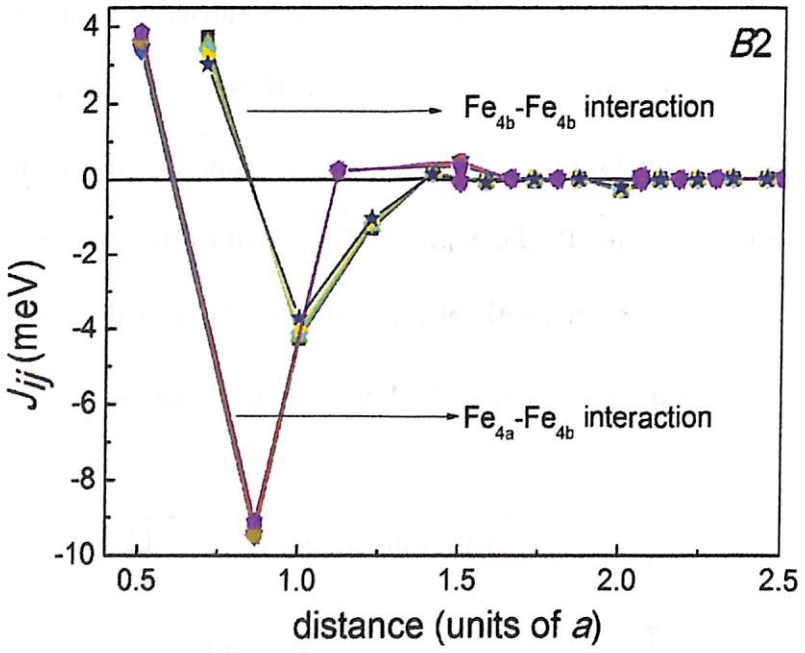

Figure 4.7 Heisenberg exchange integral versus Fe-Fe interatomic distance plots depicting the magnetic interaction in $Ru_2Fe(Si_{1-x}Ge_x)$ alloys with B2 disorder.

Figure 4.7 shows both intrasub-lattice and intersub-lattice interaction between the Fe atoms with interatomic distance for B2 disordered $Ru_2Fe(Si_{1-x}Ge_x)$ alloys. As we can see, the second NN intersub-lattice interaction between the Fe_{4b} atom in the proper (4b) position and the Fe_{4a} atom in the improper position (4a) becomes antiferromagnetic due to decrease in the distance between Fe atoms. Hence, in alloys with considerable amount of B2 disorder,

antiferromagnetism would dominate. XRD pattern of Ru_2FeSi alloy reveals a disordered B2 structure and so this alloy is expected to be an antiferromagnet as confirmed by magnetization measurements (*c.f.* Figure 4.2-4.5). However, magnetic measurements show that alloys with x = 0.25, 0.50, 0.75 and 1.00 are ferromagnetic despite the absence of the characteristic (111) reflection of $L2_1$ structure in their XRD patterns. As explained in section 4.2.1, intensity of (111) reflection is reduced below the detectable limit for the alloys with $x > 0$, despite their $L2_1$ structure.

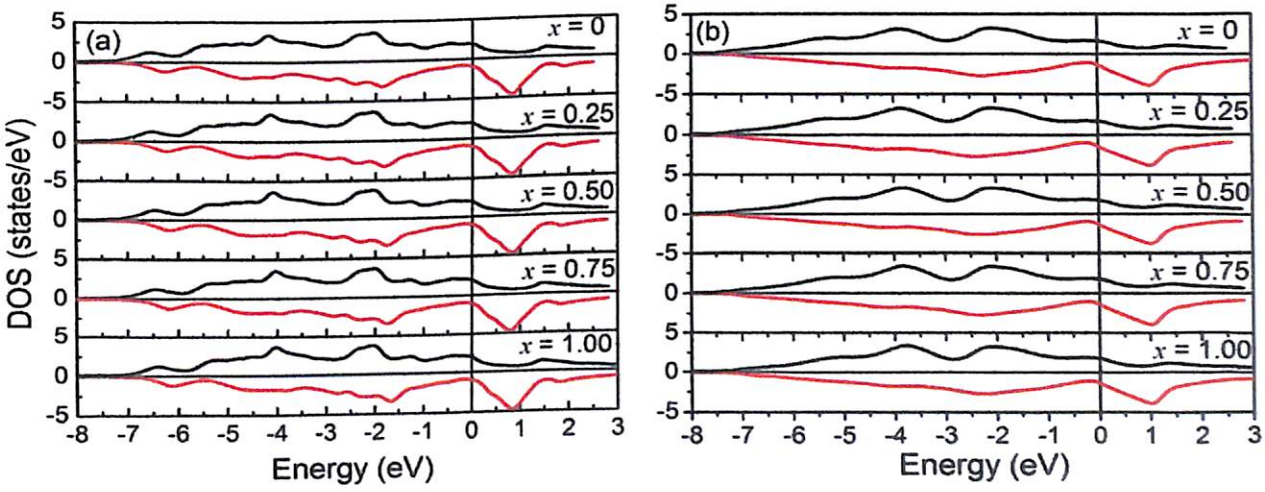

Figure 4.8 Total DOS for $Ru_2Fe(Si_{1-x}Ge_x)$ alloys with (a) $L2_1$, and (b) B2 structures.

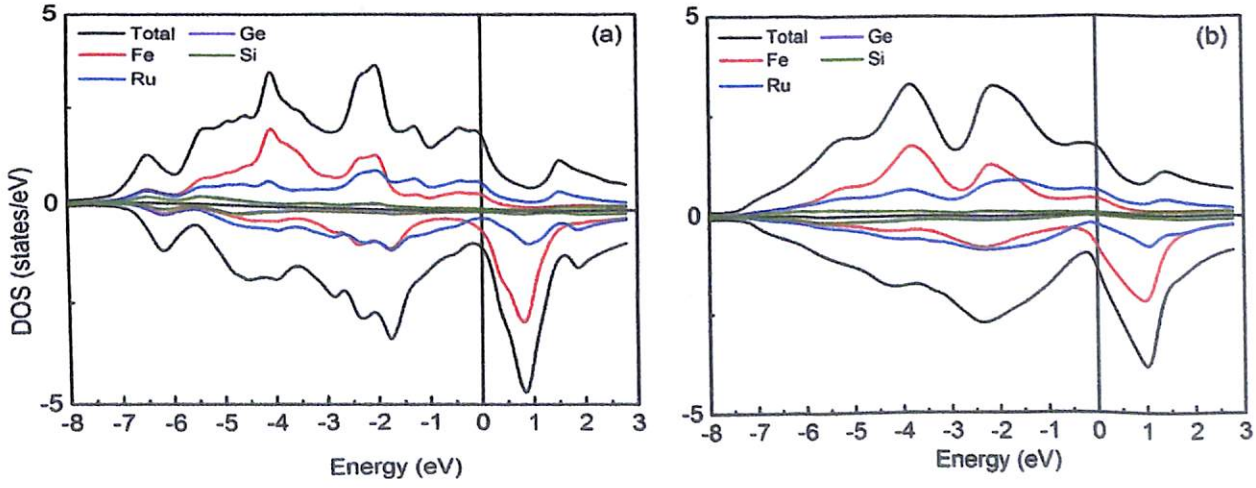

Figure 4.9: Total and atom resolved DOS for the alloys with (a) $L2_1$ and (b) B2 structures.

In order to examine the electronic structure of these alloys with both $L2_1$ and B2 structures close to E_F, their DOS was calculated and shown in Figure 4.8(a) and Figure 4.8(b), respectively. It is immediately evident from these figures that there is no gap at E_F for either spin direction for both $L2_1$ and B2 phases. So, half-metallicity is not present in any of the $Ru_2Fe(Si_{1-x}Ge_x)$ alloys. It is worthy to point out here that previous theoretical calculation performed on the alloy with $x = 1$ [AHAM15a] yielded similar result. However, a minimum (or a pseudo gap) is observed at E_F for the alloys in the minority bands of the DOS. The position of this minimum shifts to lower energy when B2 disorder is introduced.

Figure 4.9(a) and Figure 4.9(b) show the atom resolved DOS for the alloy with $x = 0.5$ with ordered $L2_1$ and disordered B2 structures, respectively. Fe atom is more affected by the disorder as compared to Ru as shown by the DOS. Similar behavior in DOS has also been observed in the isoelectronic ferromagnetic compound Fe_3Si [RMA14a].

4.3. $(Ru_{1-x}Co_x)_2FeSi$ $(0 \leq x \leq 1)$ alloys

Having observed a transition from antiferromagnetism to ferromagnetism in $Ru_2Fe(Si_{1-x}Ge_x)$ upon substitution of *sp* element with an isovalent *sp* element, effect of 4*d* X element substitution with 3*d* X′ element was attempted in $(Ru_{1-x}Co_x)_2FeSi$ alloy system. The following sections describe the investigations carried on this set of quaternary alloys.

4.3.1 Crystal structure

Room temperature XRD patterns of $(Ru_{1-x}Co_x)_2FeSi$ alloys are shown in Figure 4.10. The alloys with $x = 0.50$, 0.75 and 1.00 crystallized in $L2_1$ structure as revealed by the presence of the super-lattice reflections (111) and (200). However, the (111) reflection was absent in the XRD patterns of Ru rich compositions *i.e.*, in alloys with $x = 0$ and 0.25. Absence of peaks with all odd indices in the XRD patterns indicates a transition from $L2_1$ to B2 structure due to intermixing of Y and Z elements. As x is increased in $(Ru_{1-x}Co_x)_2FeSi$ alloys, the peaks shift

towards higher 2θ values. The lattice constant *a* obtained from the Rietveld analysis of the cubic samples with x = 0, 0.25, 0.50, 0.75 and 1.00 are 5.88 Å, 5.83 Å, 5.76 Å, 5.70 Å and 5.63 Å, respectively. Linear variation in lattice constant with x indicates that Co atoms effectively substitute for Ru atoms in the lattice. A continuous contraction of the lattice occurs with an increase in x because the atomic radius of Co (= 1.67 Å) is smaller than that of Ru (= 1.89 Å). Lattice constant of the end members of this alloy system, *i.e.* Ru_2FeSi and Co_2FeSi are 5.88 Å and 5.63 Å, respectively, which are in close agreement with earlier experimental observations [SWUR06a, SNMI85a]. XRD patterns simulated for $(Ru_{1-x}Co_x)_2FeSi$ alloys with $L2_1$ unit cell using CaRIne™ software is shown in Figure 4.11 for comparison.

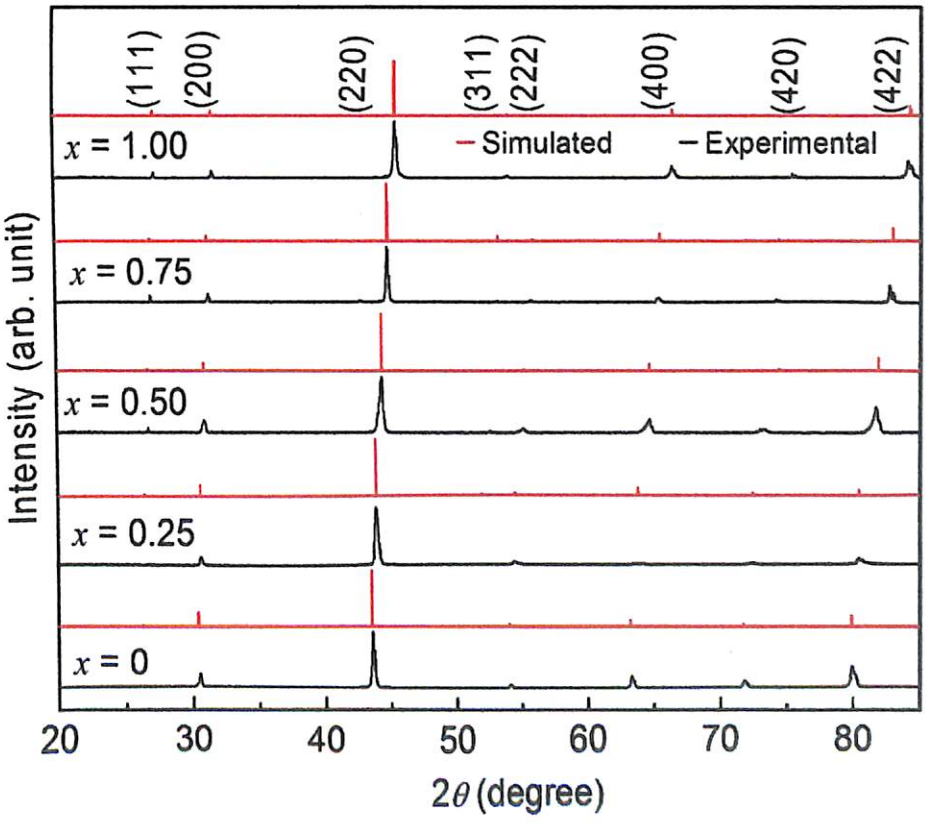

Figure 4.10: Room temperature XRD patterns of $(Ru_{1-x}Co_x)_2FeSi$ $(0 \leq x \leq 1)$ alloys. Simulated XRD patterns for the alloys with $L2_1$ structure are also shown for comparison.

Table 4.3: Nominal composition, measured composition, lattice parameter, unit-cell volume and Bragg factor R_B of Rietveld refinement of $(Ru_{1-x}Co_x)_2FeSi$ $(0 \leq x \leq 1)$ alloys.

Alloy ID	Nominal Composition	Measured Composition	a (Å)	Unit-cell volume (Å^3)	R_B
$x = 0$	Ru_2FeSi	$Ru_{1.99}FeSi_{1.01}$	5.88	203.30	7.0
$x = 0.25$	$Ru_{1.5}Co_{0.5}FeSi$	$Ru_{1.5}Co_{0.49}FeSi_{1.01}$	5.83	198.16	9.6
$x = 0.50$	RuCoFeSi	$RuCo_{1.01}Fe_{0.99}Si$	5.76	191.10	8.2
$x = 0.75$	$Ru_{0.5}Co_{1.5}FeSi$	$Ru_{0.51}Co_{1.49}FeSi$	5.70	185.19	7.3
$x = 1.00$	Co_2FeSi	$Co_2Fe_{0.99}Si_{1.01}$	5.63	178.45	9.1

4.3.2 Magnetic properties

Antiferromagnetic nature of Ru_2FeSi alloy with T_N at 270 K has already been discussed earlier in this chapter. Figure 4.11 shows the thermo-magnetization (M-T) curves for the alloy with $0.25 \leq x \leq 1$ recorded under an applied field of 1.5 kOe. As Co concentration is increased from $x = 0.25$ to $x = 1.00$, magnetization increases due to increased ferromagnetic interaction as indicated by an increase in T_C. Instead of the usual sharp transition at T_C, a wide transition range is observed at T_C for the alloy with $x = 0.25$. This may be due to residual antiferromagnetic interaction present in the alloy. T_C for the alloys with x = 0.25, 0.50, 0.75 and 1.00 are 578 K, 872 K, 968 K and 1021 K, respectively. Thus, the ferromagnetic state becomes dominant as x is increased in these quaternary alloys. T_C for the alloy with $x = 1$ is found to be slightly higher than the value reported in the previous chapter. This may be due to increased applied field in the present case due to which more thermal energy is required for the phase transition.

Figure 4.12 shows the Curie-Weiss plots for $0.25 \leq x \leq 0.75$ depicting the variation of magnetic susceptibility (χ^{-1}) for $T > T_C$. Rhodes-Wohlfarth ratio (p_c/p_s) of the alloys are calculated and displayed in Table 4.4. R-W ratio was found to be greater than unity for all the alloy compositions. This indicates that $(Ru_{1-x}Co_x)_2FeSi$ alloys are not half-metallic.

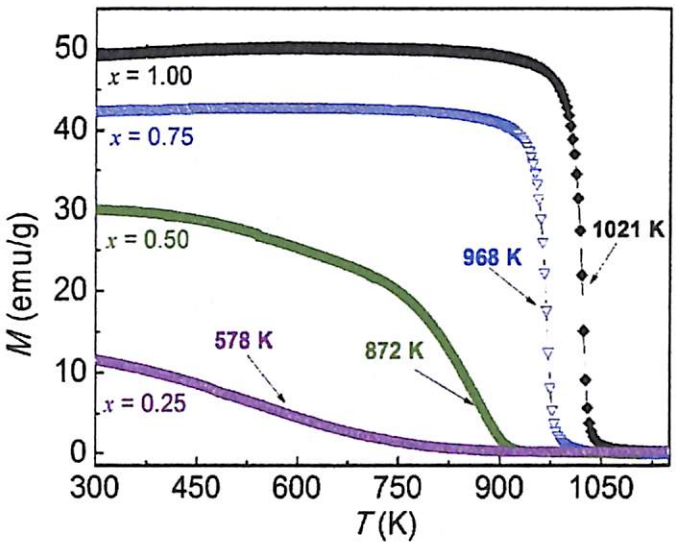

Figure 4.11 Thermo-magnetization curves of $(Ru_{1-x}Co_x)_2FeSi$ alloys recorded under 1.5 kOe.

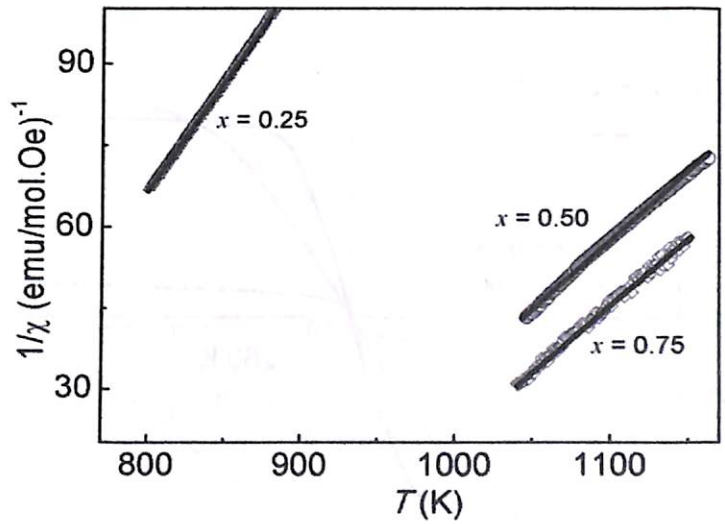

Figure 4.12 χ^{-1} versus T plots for ferromagnetic $(Ru_{1-x}Co_x)_2FeSi$ alloys for $T > T_C$.

Figure 4.13 shows the field dependence of magnetization (*M-H* curves) recorded at room temperature for all the alloys. Magnetization shows linear field dependence for the antiferromagnetic alloy with $x = 0$ as discussed earlier. With increase in x, spontaneous magnetization appears in the alloys. Magnetization at an applied field of 15 kOe increases from 1.02 emu/g to 149.96 emu/g as x is increased from 0 to 1.00. In Ru_2FeSi with B2 structure, the spacing between the (111) layers which contain both Fe and Si atoms is 1.70 Å ($= a/2\sqrt{3}$). Ru atoms occupy (0 0 0) and (½ ½ ½) positions which are placed in between the

(111) layers. Fe atoms occupying lattice points in (111) layers are coupled ferromagnetically within the layer. However, the alloy behaves as a antiferromagnet due to the antiferromagnetic coupling between the adjacent (111) layers [SNMI85a, ASZY89a]. Upon Co substitution for Ru up to 25%, B2 structure is preserved in this alloy system. But, the smaller atomic radius of Co as compared to Ru results in reducing this (111) layer spacing down to 1.68 Å. This leads to a collapse of the antiferromagnetic coupling between the (111) layers and induces ferromagnetic interaction in the alloy. With further increase in Co substitution, $L2_1$ order develops in the alloys.

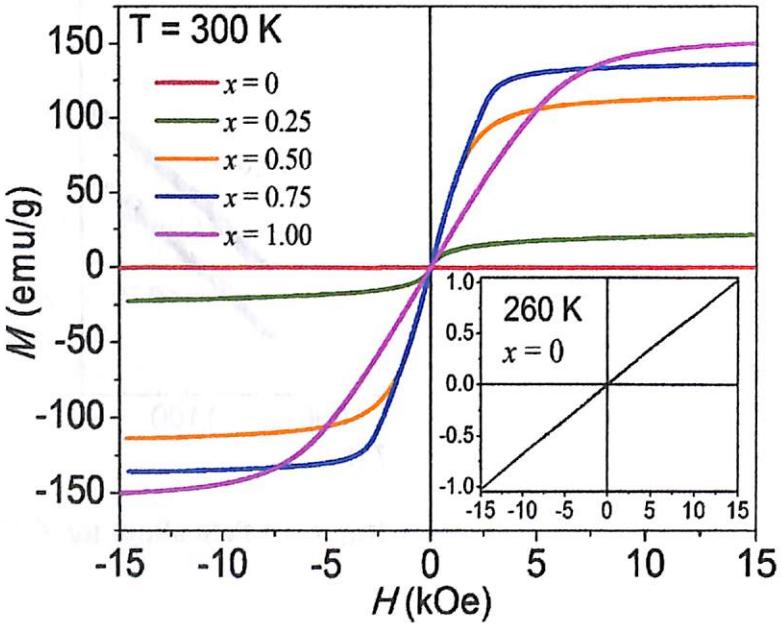

Figure 4.13: *M-H* curves of $(Ru_{1-x}Co_x)_2FeSi$ alloys with $0 \leq x \leq 1$.

It can be seen from Figure 4.13 that the *M-H* curves for the alloys with $x = 0.50$, 0.75 and 1.00 show magnetic saturation for applied fields of 15 kOe. Room temperature initial magnetization (*M-H*) curves obtained for these three alloy compositions are depicted in Figure 4.14. Saturation magnetization (M_s) for the alloys with $x = 0.50$, 0.75 and 1.00 are $4.99\mu_B$ ($5.00\mu_B$), $5.45\mu_B$ ($5.50\mu_B$) and $5.42\mu_B$ ($6.00\mu_B$), respectively, where the values within

brackets are the values predicted by the S-P rule. Thus, the measured M_s values are lower than the predicted values and this deviation from the S-P rule increases with increase in x. The probable reason for the lower M_s could be the presence of small amounts of DO_3 type disorder in the alloy as discussed in the previous chapter. Increase in the deviation of M_S from S-P rule with increasing x indicates an increase of DO_3 type disorder in the alloys with increasing x.

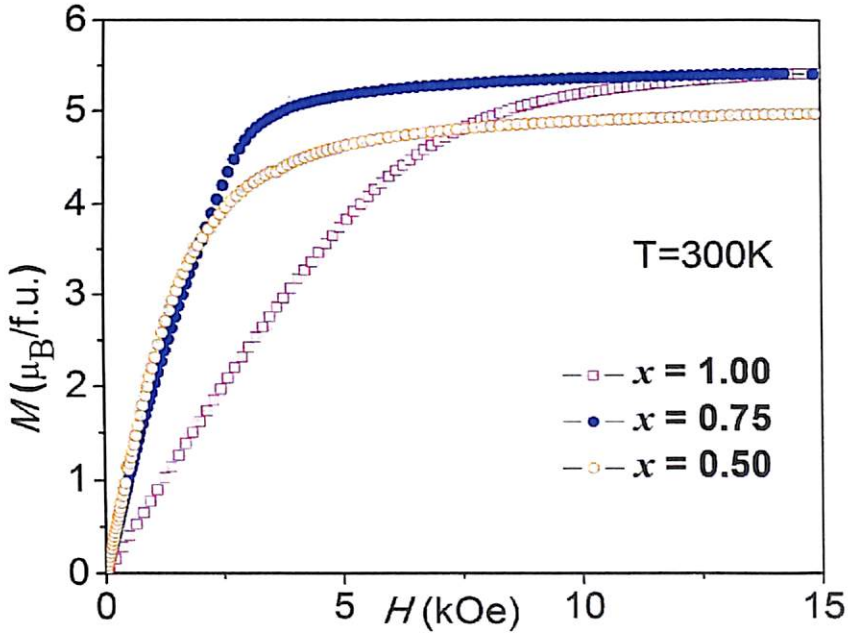

Figure 4.14 Initial magnetization curves of $(Ru_{1-x}Co_x)_2FeSi$ alloys with $0.50 \leq x \leq 1$.

Table 4.4. Magnetic moment at an applied field of 15 kOe, effective moment per magnetic atom (p_c), (p_c/p_s), M_t calculated using nominal composition (M_{Nom}) and EDS measured composition (M_{EDS}) and effective anisotropy constant (K_{eff}) of $(Ru_{1-x}Co_x)_2FeSi$ alloys.

x	$M_{15\,kOe}$ (μ_B)	p_c (μ_B)	p_c/p_s	M_{Nom} / M_{EDS} (μ_B)	K_{eff} [$\times 10^5$ Jm^{-3}]
0	0.04	4.40	-	4.00/3.96	-
0.25	1.10	3.71	3.37	4.50/4.45	-
0.50	4.99	5.11	1.02	5.00/5.01	4.02
0.75	5.45	5.71	1.04	5.50/5.49	6.10
1.00	5.42	4.77	0.86	6.00/5.96	11.17

K_{eff} value for the alloys with $x = 0.50$, 0.75 and 1.00 calculated from the *M-H* data are depicted in Figure 4.14 and listed in Table 4.4. K_{eff} increases with increase in Co concentration indicating larger magnetic anisotropy in Co rich alloys. Magneto-crystalline anisotropy of Co (5.30×10^5 Jm^{-3}) is higher than that of Fe (0.48×10^5 Jm^{-3}) [HPWI91a]. As discussed above, DO_3 type disorder can be present in the alloys with $x > 0.25$. Since this disorder is associated with the distribution of the magnetic Fe and Co atoms in the alloy, an increase in DO_3 disorder with increasing Co substitution can lead to an increase in magnetic anisotropy. Relatively larger percentage of DO_3 disorder in the alloy with $x = 1$ is probably responsible for the unusually large K_{eff} exhibited by this alloy. When compared to other bulk Heusler alloys such as $Ni_{50}Mn_{30}Ga_{20}$ (1.01×10^5 Jm^{-3}) [CJIA04a] and $Co_{43}Ni_{22}Ga_{29}Fe_6$ (2.20×10^5 Jm^{-3}) [SSAR11a], K_{eff} value for this alloy system is relatively higher. The high K_{eff} observed in the bulk samples can increase further in nanogranular state and may find application in magnetic media.

4.4 Summary

Some of the interesting results obtained in the investigations carried out on $Ru_2Fe(Si_{1-x}Ge_x)$ and $(Ru_{1-x}Co_x)_2FeSi$ alloys are summarized below:

1. $Ru_2Fe(Si_{1-x}Ge_x)$ alloys are found to crystallize in disordered B2 structure since the XRD patterns do not show the characteristic (111) reflection. However, the absence of the (111) reflection in alloys with high Ge concentration may be due to nearly equal scattering factor of Fe and Ge.
2. $(Ru_{1-x}Co_x)_2FeSi$ alloys with $x > 0.25$ crystalize in ordered $L2_1$ structure.
3. Antiferromagnetism of the parent compound Ru_2FeSi gets destroyed when Ge and Co is substituted for Si and Ru, respectively.

4. *Ab initio* calculations carried out on $Ru_2Fe(Si_{1-x}Ge_x)$ alloys clarify that antiferromagnetism in Ru_2FeSi stems from the B2 disorder present in this alloy.
5. Ferromagnetism appears in $Ru_2Fe(Si_{1-x}Ge_x)$ alloys because of onset of $L2_1$ ordering in these alloys.
6. These studies show that both antiferromagnetic and ferromagnetic alloys can be obtained in these alloy systems depending on the composition and chemical ordering.
7. R-W ratio of alloys containing Ru is found to be greater than unity indicating the absence of half-metallic character in these alloys. DOS calculations for $Ru_2Fe(Si_{1-x}Ge_x)$ alloys supports this result.

Chapter 5

INVESTIGATIONS ON $(Mn_{1-x}Co_x)_2VAl$ AND $(Mn_{1-x}Co_x)_2VGa$ ALLOYS

Most of the literature on half-metallic Heusler alloys is devoted to ferromagnetic alloys with very less attention to ferrimagnetic alloys. Due to the internal spin compensation, ferrimagnets have a low magnetic moment which gives rise to low stray fields. Such half-metallic ferrimagnets can be used to measure the spin polarization of samples without perturbing their magnetic domain structures [RADE91a, RADE91a]. Half-metallic materials exhibiting high spin polarization and no stray magnetic fields are in demand for fabricating new and efficient spintronic devices [RADE91a, HVAN95a, WEPI96a, FWUS09a]. Figure 1.6(a) shows that Mn_2VZ alloys are ferrimagnets according to S-P rule. Ferrimagnetic Mn_2VZ Heusler compounds have been the subject of a few theoretical studies [ESAI05a, KOZD06a]. *Ab initio* calculations have predicted half-metallic electronic structure with high polarization in compounds with Z = Al, Ga, In, Si, Ge, and Sn with a band gap for majority spin carriers and a ferrimagnetic ground state [KOZD06a]. A gap in the majority spin band in Mn_2VGa based MTJs has been confirmed by their negative TMR at room temperature [CKLE13a]. *Ab initio* calculations have demonstrated that progressively substituting for Mn with Co in ferrimagnetic $Mn_2VAl(Si)$ compound can lead to zero moment or a fully compensated ferrimagnet (FCF) [IGAL07a]. Table 5.1 (cited from reference IGAL07a) shows the effect of Co doping on atomic magnetic moments of Mn_2VAl alloy. For the alloy with $x = 0.5$ *i.e.* MnCoVAl, total number of valence electron is 24 and the total moment M_t vanishes completely. As Co concentration increases, each Co atom can hybridize more strongly with its neighboring Co atoms thereby increasing the Co spin moment while that of Mn atoms decreases slightly. For all compositions of $(Mn_{1-x}Co_x)_2VAl$, Co spin moment aligns parallel to that of V and antiparallel to that of Mn spin moment, thus keeping their ferrimagnetic character intact. The most interesting point is that although M_t of MnCoVAl

vanishes, the compound itself is made up of strongly magnetic components. Therefore this composition is referred to as a fully commentated ferrimagnet.

Table 5.1: Atom-resolved spin magnetic moments in $(Mn_{1-x}Co_x)_2VAl$ alloys [from IGAL07a]

x	Mn	Co	V	Al	Total	S-P
0	-1.573		1.082	0.064	-2.000	−2.0
0.025	-1.573	0.406	1.102	0.074	-1.899	-1.9
0.05	-1.580	0.403	1.090	0.073	-1.799	-1.8
0.1	-1.564	0.398	1.067	0.069	-1.600	-1.6
0.2	-1.522	0.412	1.012	0.059	-1.200	-1.2
0.3	-1.484	0.456	0.953	0.047	-0.804	-0.8
0.4	-1.445	0.520	0.880	0.034	-0.404	-0.4
0.5	-1.388	0.586	0.782	0.019	~ 0	0

Some attempts have been made to search for FCF in ferrimagnetic Mn_3Ga and substituted $Mn_{3-x}Ga$ alloys [HNII96a, BBAL07a, HKUR11a, HKUR11b, MHAK13a, WFER13a]. These attempts have yielded ferrimagnetic thin films with low saturation magnetization (M_s) of $0.65\mu_B$ and intrinsic spin polarization (P) of 0.58 [HKUR11a]. However, these pseudo-ternary alloys exhibit tetragonal DO_{22} structure instead of the stable $L2_1$ structure of a full Heusler alloy. Practical difficulties in maintaining the nominal stoichiometry and preventing oxidation during the preparation of Heusler alloys with high Mn content have been the main deterrents as evidenced by very few experimental reports on bulk and thin films of Mn_2VAl [KHJB81a, MKAW81a, YYOS81a, HITO83a, TAKA83a, CJIA01a, TKUB09a, MMEI11a], Mn_2VGa [KRKU08a, CKLE13a] and $(Mn_{1-x}Co_x)_2VGa$ [KRKU10a] alloys. These studies also reveal a general lack of $L2_1$ order and the presence of significant amounts of V-Z (where Z = Al, Ga) type disorder in most of the reported alloys. It has to be pointed out that no attempt has been made to extract spin polarized currents from

full Heusler based ferrimagnets and FCF to the best of our knowledge. Hence, the nature and the application potential of Heusler based FCFs have not been properly assessed so far. In this chapter, a detailed study of the effect of Co substitution for Mn in Mn_2VAl and Mn_2VGa alloys on their structural and magnetic properties is presented. Spin polarization study on $(Mn_{1-x}Co_x)_2VAl$ alloys has also been performed since nearly zero moment alloy has been obtained in this system.

5.1. Preparation of alloys

Polycrystalline $(Mn_{1-x}Co_x)_2VAl$ and $(Mn_{1-x}Co_x)_2VGa$ ($0 \leq x \leq 0.5$) alloy ingots were prepared by arc melting method followed by homogenization at 1173 K for 24 h and quenching in ice + water mixture as described in the second chapter. The overall composition of the alloys as determined by EDS analysis is presented in Table 5.2 and Table 5.4, respectively.

Table 5.2: Nominal composition, measured composition, lattice parameter, unit-cell volume, Bragg factor R_B of Rietveld refinement of $(Mn_{1-x}Co_x)_2VAl$ ($0 \leq x \leq 0.5$) alloys.

Alloy ID	Nominal Composition	Measured Composition	a (Å)	Unit-cell volume (Å^3)	R_B
$x = 0$	Mn_2VAl	$Mn_{2.05}V_{0.95}Al_{1.00}$	5.84	199.18	6.93
$x = 0.25$	$Mn_{1.5}Co_{0.5}VAl$	$Mn_{1.46}Co_{0.56}V_{1.0}Al_{0.98}$	5.81	196.12	7.01
$x = 0.50$	MnCoVAl	$Mn_{1.0}Co_{0.99}V_{1.0}Al_{1.01}$	5.78	193.10	7.56

5.2 $(Mn_{1-x}Co_x)_2VAl$ ($0 \leq x \leq 0.50$) alloys

5.2.1. Crystal Structure

Figure 5.1 shows the room temperature XRD patterns of $(Mn_{1-x}Co_x)_2VAl$ alloys. Presence of super-lattice reflections (111) and (200) in all the XRD patterns confirms that all

$(Mn_{1-x}Co_x)_2VAl$ alloys prepared in this study exhibit the stable $L2_1$ structure of full Heusler alloys.

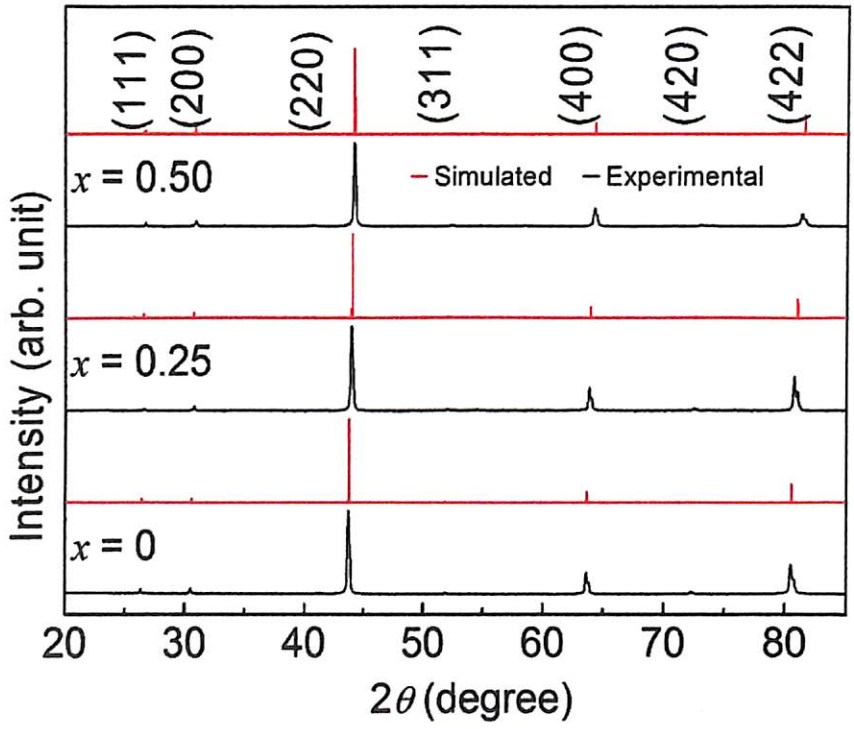

Figure 5.1: Room temperature XRD patterns of $(Mn_{1-x}Co_x)_2VAl$ alloys with $0 \leq x \leq 0.50$. Simulated XRD patterns for the alloys with $L2_1$ structure are also shown for comparison.

Degree of atomic ordering in the alloys was estimated from the ratio of the intensity (I_{hkl}) of the super-lattice reflections from (111) and (200) planes using the relations 2.3 and 2.4 as described in section 2.2.1. $S = 0.95$ and $\alpha = 0.06$ estimated for Mn_2VAl alloy indicates a high degree of $L2_1$ order in this alloy with only about 2.5% of X sites being occupied by improper (i.e. Y and Z) atoms and < 6% of the Y (or Z) site being occupied by Z (or Y) atoms. Similarly, S (α) values of 0.96 (0.06), and 0.94 (0.05) obtained for $(Mn_{1-x}Co_x)_2VAl$ alloys with $x = 0.25$ and $x = 0.5$, respectively, indicate high degree of B2 order in these alloy compositions as well. The lattice constant a of the cubic alloys with $x = 0$, 0.25 and 0.5 are

5.84 Å, 5.81 Å and 5.78 Å, respectively. The contraction in lattice with increase in Co substitution is expected as the atomic size of Co (= 1.67 Å) is smaller than that of Mn (= 1.79 Å). The linear decrease in lattice parameter a with increase in x shows that Co atoms effectively substitute for Mn atoms in the lattice. The lattice constant for Mn_2VAl (or alloy with $x = 0$) can be compared with the values reported in the literature for bulk (5.87 Å [HITO83a] and 5.92 Å [TAKA83a]) and thin films (5.84 Å) [MMEI11a] of Mn_2VAl alloy. Meinert *et al.* found that co-sputtered Mn_2VAl films on MgO (001) substrate exhibit $L2_1$ order with significant V-Al type disorder [MMEI11a]. They also observed that $L2_1$ order disappears in the alloy upon substitution of Co for Mn in $Mn_{2-x}Co_xVAl$ films. An earlier report on bulk Mn_2VAl [CJIA01a] alloys did not show clear evidence of the super-lattice reflections in the XRD patterns. On the other hand, the alloys reported in this work exhibit clear evidence of $L2_1$ order. EDS analysis performed on our samples revealed as much as 2.7 wt.% deviation in composition of the alloys from the nominal value despite the care taken in the preparation (*c.f.* Table 5.2). This final composition of the alloys has to be borne in mind while interpreting the results since the properties of Heusler alloys are extremely sensitive to compositional variations.

5.2.2. Magnetic properties

Figure 5.2 shows the thermo-magnetization (M–T) curves recorded for $(Mn_{1-x}Co_x)_2VAl$ alloys with various Co concentrations (x = 0, 0.25 and 0.5) under an applied field of 100 Oe. T_C was found to decrease with increase in Co substitution. T_C for x = 0, 0.25 and 0.5 are 750 K, 423 K and 105 K, respectively. T_C obtained for the alloy with $x = 0$ is in agreement with the value of 760 K reported in the literature [CJIA01a]. Decrease in T_C with increased substitution of Co for Mn in $(Mn_{1-x}Co_x)_2VAl$ alloys can be attributed to reduction in magnetic moment due to the appearance of antiferromagnetic interaction between Mn and Co

atoms [IGAL07a]. The drastic reduction in T_C with increase in x observed in this series of alloys has resulted in the MnCoVAl alloy to have an unexpectedly low T_C of 105 K. This could have serious implications on the application of this alloy in spintronic devices.

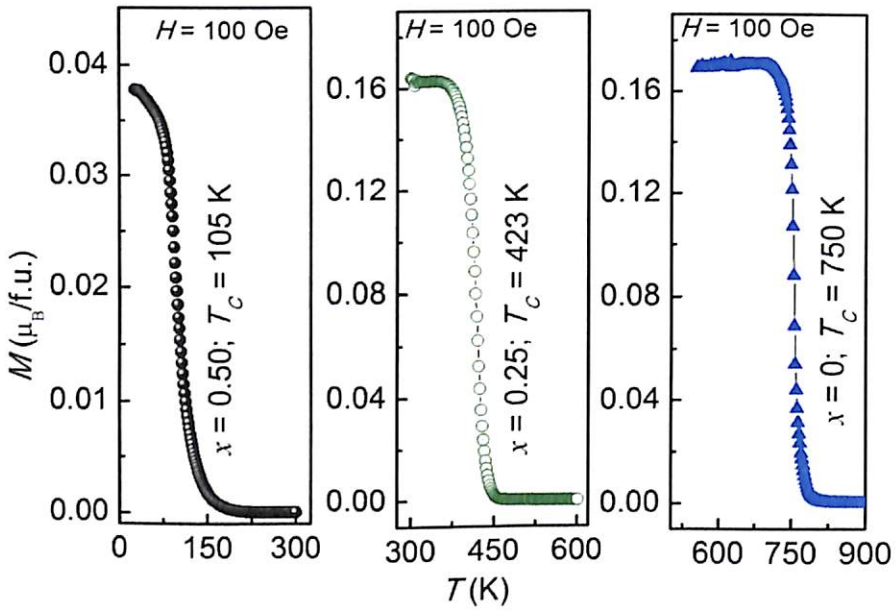

Figure 5.2 Thermo-magnetization (M-T) curves of $(Mn_{1-x}Co_x)_2VAl$ alloys recorded at 100 Oe.

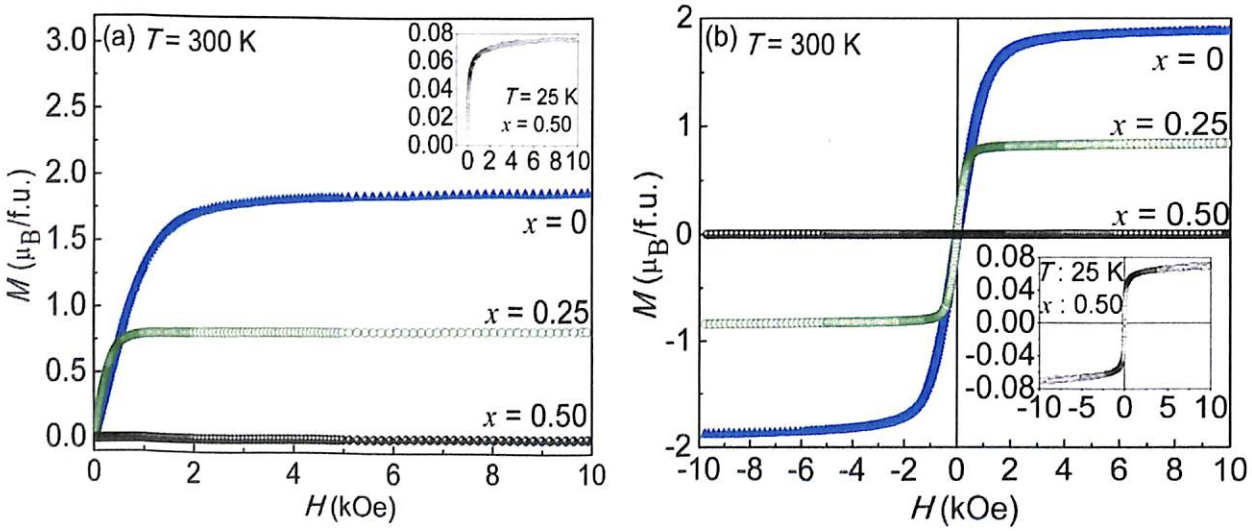

Figure 5.3: (a) Variation of initial magnetization (M) with applied magnetic field (H) and (b) Complete M-H loops for $(Mn_{1-x}Co_x)_2VAl$ alloys. Insets show the corresponding data for MnCoVAl alloy recorded at 25 K.

Initial magnetization (*M-H*) curves and full *M-H* loops recorded for all the alloy compositions at room temperature are shown in Figure 5.3(a) and 5.3(b) respectively. Insets in Figure 5.3 shows the corresponding data recorded at 25 K for MnCoVAl alloy with T_C of 105 K. According to the Slater-Pauling (S-P) rule, the compound Mn_2VAl should have $M_t = -2\mu_B$ as a result of anti-parallel alignment of Mn and V moments [IGAL07a]. Since Co moments prefer parallel alignment with V moments and Mn moments align antiparallel to the V moment, M_t gets reduced with increased Co substitution at Mn sites [IGAL07a]. X-ray magnetic circular dichroism studies on $Mn_{2-x}Co_xVAl$ films show that antiparallel alignment of Mn and V is preserved for Co substitution of up to $x = 0.5$ [MMEI11a].

Table 5.3: Saturation magnetic moment (M_s), M_t calculated using nominal composition (M_{Nom}) and EDS measured composition (M_{EDS}), effective anisotropy constant (K_{eff}), Curie temperature (T_C) and intrinsic spin polarization P of $(Mn_{1-x}Co_x)_2VAl$ alloys.

x	M_s (μ_B)	M_{Nom} / M_{EDS} (μ_B)	K_{eff} ($\times 10^4$ Jm^{-3})	T_C (K)	P
0	1.88	2.00 / 1.90	7.56	750	0.57
0.25	0.84	1.00 / 0.80	1.19	423	0.59
0.50	0.07	0 / 0.06	0.61	105	0.60

M_t values calculated using Eq. 1.5 for the nominal composition of the alloys with $x = 0$, 0.25 and 0.50 are $2.0\mu_B$, $1.0\mu_B$ and $0\mu_B$, respectively. M_s determined from the *M-H* data of the alloys with $x = 0$, 0.25 and 0.50 are $1.88\mu_B$, $0.84\mu_B$ and $0.07\mu_B$, respectively. Comparison of the measured M_s with the corresponding M_t value predicted by S-P rule (*c.f.* Table 5.3) shows a slight deviation in the experimentally measured value from the theoretically predicted value for the nominal composition. This deviation can be explained in terms of small variation in stoichiometry (Table 5.2) and weaker hybridization between Co–V states as compared to that of Mn–V states, resulting in domination of Mn-V antiferromagnetic interaction over Co-V

ferromagnetic one [KRKU10a]. If one takes the above factors into account, it is evident that Co substitution for Mn in $(Mn_{1-x}Co_x)_2VAl$ alloys decreases the M_t and leads to a zero moment FCF when Co and Mn concentrations are equal, *i.e.* in MnCoVAl alloy. It has to be pointed out that the attempts to obtain FCF in Mn_3Ga [HKUR11a] and MnCoVGa [KRKU10a] have so far yielded the lowest M_s of $0.65\mu_B$ and $0.37\mu_B$, respectively. Interestingly, the films of $Mn_{2-x}Co_xVAl$ are claimed to have a high degree of disorder which influences their magnetic properties [MMEI11a]. Because of this disorder, FCF is expected in $Mn_{1.5}Co_{0.5}VAl$ film at a much lower Co substitution as compared to the bulk case. However, the absence of $L2_1$ order as well as the lack of information on the actual composition complicates the interpretations of the results obtained for the films. In order to fully comprehend the nature of FCF, some associated magnetic properties of $(Mn_{1-x}Co_x)_2VAl$ alloys have been investigated.

Assessment of the magnetic anisotropy in a material is important to evaluate its potential for spin torque applications. Effective magnetic anisotropy constant K_{eff} is commonly used to represent this parameter. K_{eff} can be estimated from the initial magnetization (M–H) curves using the law of approach to saturation (Eq. 2.23 and Eq. 2.24). K_{eff} for the alloys with $x = 0$, 0.25 and 0.5 are 7.56×10^4 Jm^{-3}, 1.19×10^4 $Jm^{-3}$and 0.61×10^4 Jm^{-3}, respectively. K_{eff} decreases with increase in Co content in $(Mn_{1-x}Co_x)_2VAl$ alloys and the lowest value was obtained for the FCF with $x = 0.5$. K_{eff} of full Heusler alloys are generally of the order of 10^5 Jm^{-3}. The lower K_{eff} of $(Mn_{1-x}Co_x)_2VAl$ alloys mainly stems from their low M_s. Hence, lower M_s imposes a limitation on the maximum possible K_{eff} in these ferrimagnets which depends mainly on the magneto-crystalline anisotropy term c. However, it has been shown (as in the case of Mn_3Ga [WSYU12a]) that thin films of the same material often exhibit a higher K_{eff} than the bulk. Hence, it may be possible to obtain higher K_{eff} in thin films of $(Mn_{1-x}Co_x)_2VAl$ alloys.

Paramagnetic Curie temperature, θ_p was estimated for $(Mn_{1-x}Co_x)_2VAl$ alloys from the temperature dependence of inverse susceptibility (χ^{-1}) data beyond T_C (*cf.* Figure 5.4) using the Curie-Weiss law (Eq. 2.11). θ_p determined for all the alloys are negative (-69 K, -98 K and -120 K for x = 0, 0.25 and 0.5, respectively) confirming ferrimagnetic ordering in the alloys.

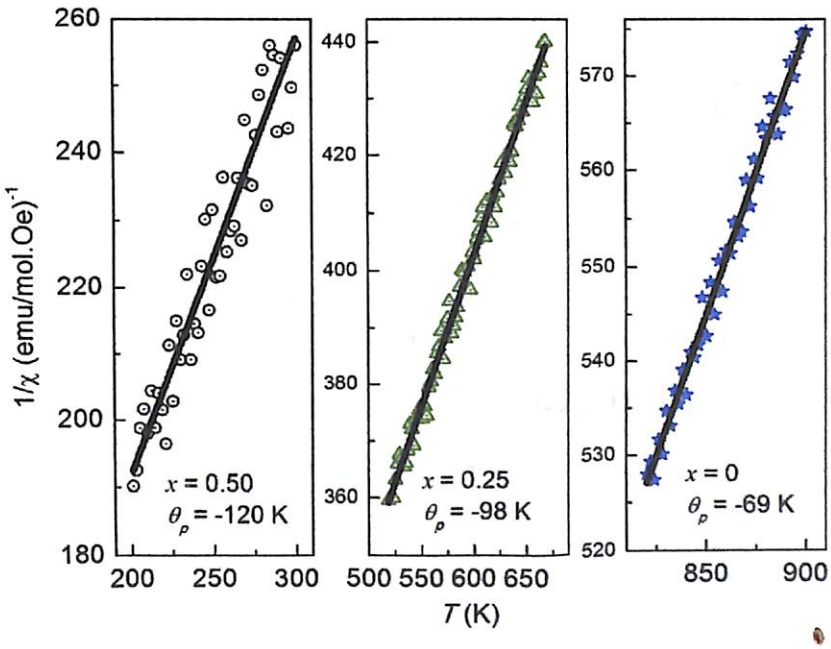

Figure 5.4: Inverse magnetic susceptibility data for $T > T_C$ of $(Mn_{1-x}Co_x)_2VAl$ alloys.

5.2.3. Spin polarization

Figure 5.5 shows selected PCAR conductance curves recorded for $(Mn_{1-x}Co_x)_2VAl$ alloys at 4.2 K with interfacial scattering factor Z = 0. The solid line corresponds to the best fit to the modified BTK model [GJST01a] as discussed in section 2.4.1. The low Z value obtained in these fits shows that the PCAR data could be fit well to the ballistic BTK model. The contact resistance in these measurements can be related to the contact diameter d using quasiclassical transport theory by the relation,

$$R = (1+Z^2)\left(\frac{4\rho l_m}{3\pi d^2} + \gamma\left(\frac{l_m}{d}\right)\frac{\rho}{2d}\right) \tag{5.1}$$

where l_m is mean free path of electron for typical hole conduction in superconductors ($\approx$ 20 nm), ρ is the electrical resistivity at 4.2 K and pre-factor $\gamma \approx 1$ for mechanical point contacts [BNIK99a].

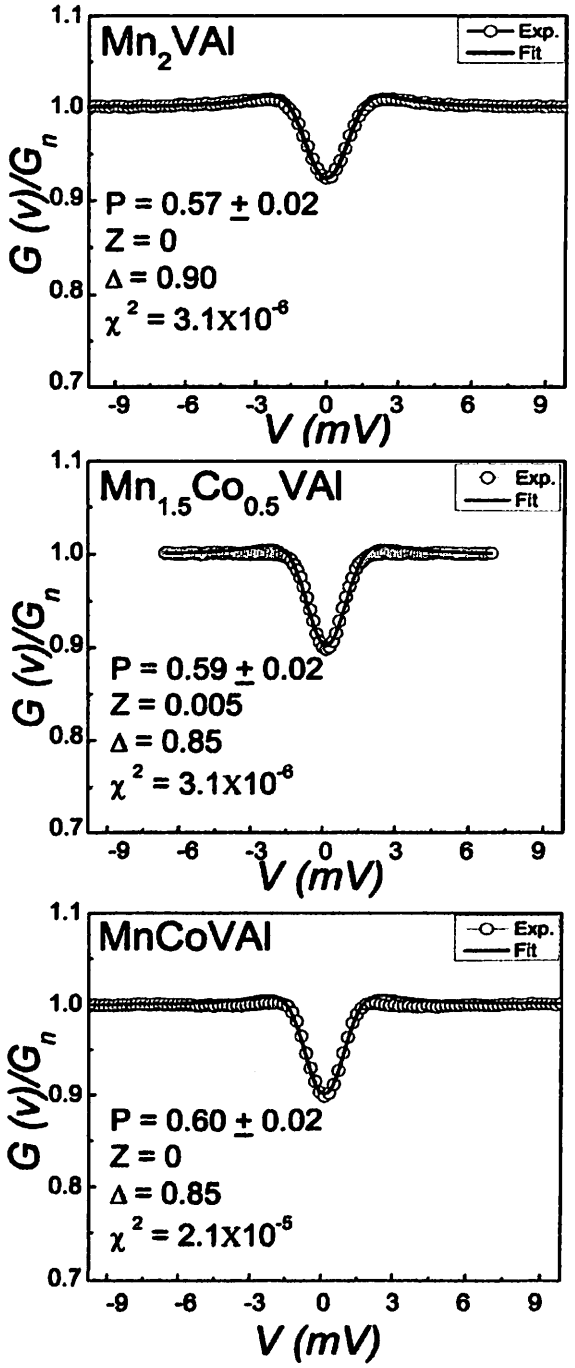

Figure 5.5: Normalized conductance curves recorded for $(Mn_{1-x}Co_x)_2VAl$ alloys with $Z \approx 0$.

$R \approx 25\ \Omega$ obtained for these measurements corresponds to a $d \approx 18$ nm. If d is less than the mean free path of electrons in metals, the contact is ballistic. Since d estimated from Eq. 5.1 is larger than the average mean free path of electrons in metals, a diffusive contact is expected. However, the physical contact in a typical PCAR experiment is much larger than this value. Considering that the low Z conductance curves in the normalized conductance curves shown in Figure 5.5 represent ballistic electron transport, which indicates that the superconducting wire tip makes multiple point contacts with the sample. Superconducting gap (Δ) values estimated from fit to PCAR data were in the range of 0.85-0.95 meV, which are much lower than the bulk superconducting band gap of Nb (~1.5 meV). This also suggests the presence of multiple point contacts in the experiments [BNIK99a, SKCL04a]. Intrinsic spin polarization P was estimated from the curves with Z = 0. P increases with Co substitution from 0.57 for the alloy with $x = 0$ to 0.60 for the $x = 0.5$ alloy. The relatively high P value obtained for the FCF alloy MnCoVAl alloys in this study may be compared with those reported for other ferrimagnetic materials such as Mn_3Ga ($P = 0.58$) [HCUR11a] and $SrLaVMoO_6$ ($P = 0.50$) [HASA10a]. PCAR studies confirm the half-metallic nature of $(Mn_{1-x}Co_x)_2VAl$ alloys.

5.3. $(Mn_{1-x}Co_x)_2VGa$ ($0 \leq x \leq 0.50$) alloys

Structural and magnetic investigations performed on $(Mn_{1-x}Co_x)_2VGa$ alloys are described below.

5.3.1. Crystal Structure

Figure 5.6 shows the XRD patterns of $(Mn_{1-x}Co_x)_2VGa$ alloys recorded at room temperature. For the alloy with $x = 0$, both (111) and (200) super-lattice peaks are present indicating that these alloys crystallized in the stable $L2_1$ structure of full Heusler alloys. However for the alloys with $x = 0.25$ and 0.50, (111) reflection is present but (200) reflection

is absent. Absence of only (200) reflection in the XRD pattern of these alloys is surprising since B2 type disorder would result in the elimination of only the (111) peak and A2 disorder will ensure that both (111) and (200) peak are absent. To understand this result, the XRD patterns

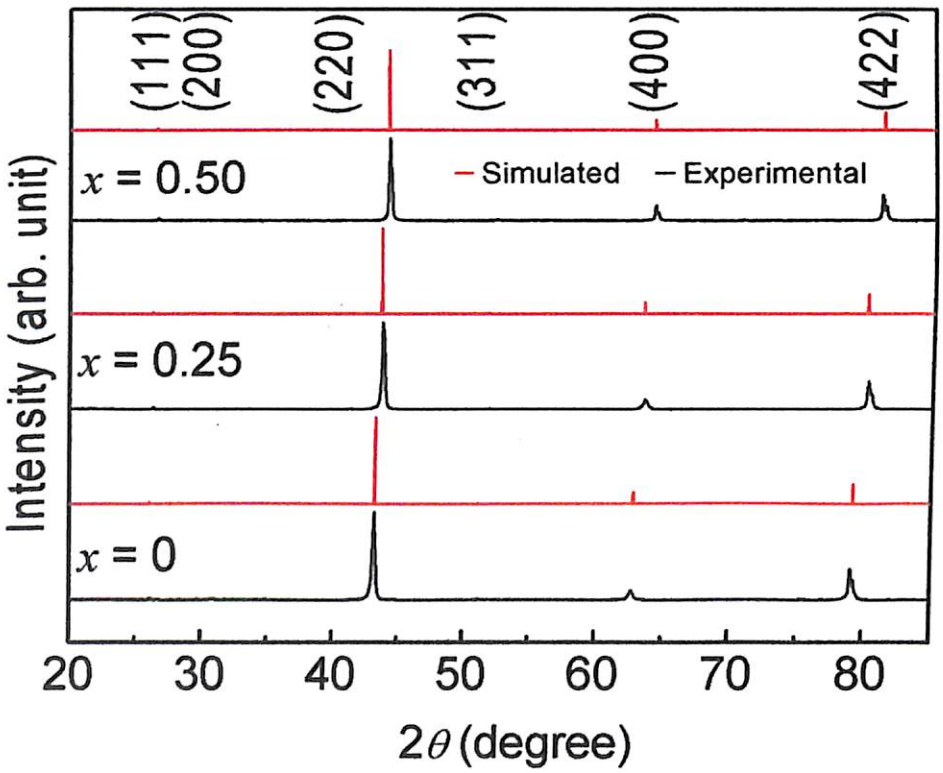

Figure 5.6: Room temperature XRD patterns of $(Mn_{1-x}Co_x)_2VGa$ alloys with $0 \leq x \leq 0.50$. Simulated XRD patterns for the alloys with $L2_1$ structure are also shown for comparison.

for $(Mn_{1-x}Co_x)_2VGa$ alloys with $L2_1$ structure were simulated using CaRIne crystallography 3.1™ software (*cf.* Figure 5.6). One can see that (200) peak is absent even in the simulated pattern for these two alloys with $L2_1$ unit cell. If all the constitute elements are from the same period of the periodic table, their nearly equal scattering amplitudes can lead to the cancellation of both (111) and (200) peaks in the XRD pattern [BBAL07a]. Though all the elements in the present alloys are from the same period, the Y (i.e. V) and Z (i.e. Ga) are far

apart in the period. Hence, the difference in their scattering amplitudes *viz.*, $(f_Y - f_Z)$ is significant enough to be detected, resulting in the observation of the (111) peak in all the XRD patterns. In the case of the (200) peak, the contribution from Mn (X) / Co (X′) scattering amplitudes come into play. Since both these elements appear in between V and Ga, the $(2f_X - (f_Y + f_Z))$ term becomes very small, thereby reducing the intensity of the (200) peak to undetectably small values for the quaternary alloys. The degree of atomic ordering in the alloys was estimated using relations 2.3 and 2.4. $S = 0.95$ and $\alpha = 0.02$ estimated for Mn_2VGa alloy indicates a high degree of $L2_1$ order in this alloy with only about 2.5% of X sites being occupied by improper (*i.e.* Y and Z) atoms and 2% of the Y (or Z) site being occupied by Z (or Y) atoms. Since both the calculated and experimental intensities for (200) peaks are zero for the alloys with $x = 0.25$ and 0.50, this analysis could not extended to these two alloys. However, the ratio $[(I_{111}/I_{220})_E/(I_{111}/I_{220})_T]$ for $x = 0.25$ and 0.50 was found out to be 0.94 and 0.95 which indicate high degree of $L2_1$ ordering for these two alloys as well. The lattice parameter of the samples with $x = 0$, 0.25 and 0.5 was determined to be 5.92 Å, 5.87 Å and 5.80 Å, respectively. Contraction in lattice with increase in Co substitution is expected as the atomic size of Co (1.67 Å) is smaller than that of Mn (1.79 Å). Lattice parameter for $x = 0$ is comparable with the earlier reported value of 5.905 Å [KRKU08a]. The observed reduction in unit cell volume with increase in Co content supports the above argument.

Table 5.4: Nominal composition, measured composition, lattice parameter, unit-cell volume and Bragg factor R_B of Rietveld refinement of $(Mn_{1-x}Co_x)_2VGa$ $(0 \leq x \leq 0.5)$ alloys.

Alloy ID	Nominal Composition	Measured Composition	a (Å)	Unit-cell volume (Å^3)	R_B
$x = 0$	Mn_2VGa	$Mn_{2.06}V_{0.95}Ga_{0.99}$	5.92	207.47	8.93
$x = 0.25$	$Mn_{1.5}Co_{0.5}VGa$	$Mn_{1.39}Co_{0.54}V_{1.14}Ga_{0.93}$	5.87	202.26	9.01
$x = 0.50$	MnCoVGa	$Mn_{0.98}Co_{0.95}V_{1.08}Ga_{0.99}$	5.80	195.11	6.23

5.3.2. Magnetic properties

Figure 5.7 shows the thermo-magnetization (*M–T*) curves for various Co concentrations (x = 0, 0.25 and 0.5) recorded under an applied field of 100 Oe. T_C was found to decrease with increase in Co substitution. T_C for the alloys with x = 0, 0.25 and 0.5 are 763 K, 478 K and 367 K, respectively. These values may be compared with the values of 783 K [KRKU08a], 538 K [KRKU10a] and 141 K [KRKU10a] reported for the respective alloy compositions in the literature. The decrease in magnetic ordering temperature with increase in Co substitution can be attributed to the reduction in magnetic moment as theoretically predicted due to the appearance of antiferromagnetic interaction between Mn and Co atoms [QFLI12a].

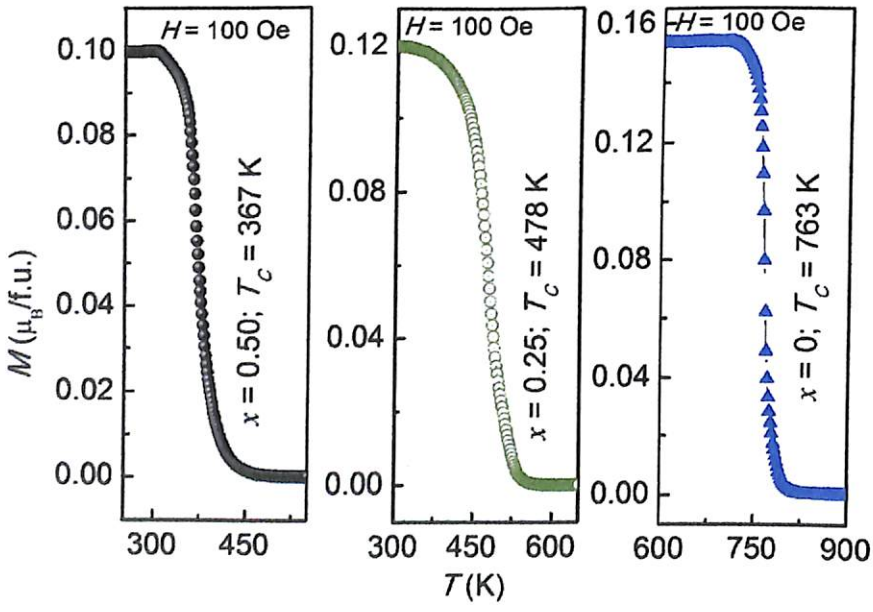

Figure 5.7: Thermo-magnetization (*M-T*) curves of $(Mn_{1-x}Co_x)_2VGa$ alloys recorded at an applied field of 100 Oe.

Paramagnetic Curie temperature, θ_p was estimated from the inverse susceptibility (χ^{-1}) versus temperature (T) plots (Figure 5.8) obtained using the Curie-Weiss law. For all the alloys θ_p was found to be negative (*i.e.*, -64 K, -83 K and -99 K for x = 0, 0.25 and 0.5, respectively)

confirming ferrimagnetic ordering in all the alloys. *Ab initio* calculations performed on Mn_2VGa [KOZD06a] and $(Mn_{1-x}Co_x)_2VGa$ ($x < 0.5$) [QFLI12a] alloys with $L2_1$ structure show that all these alloy compositions have a ferrimagnetic ground state in agreement with the S-P rule. Neutron diffraction studies on the isostructural and isoelectronic compound Mn_2VAl [HITO83a] and X-ray magnetic circular dichroism measurements on Mn_2VGa [CKLE13a] and $(Mn_{1-x}Co_x)_2VAl$ alloys [MMEI11a] also provide evidence for a ferrimagnetic coupling between Mn and V atoms in these alloys.

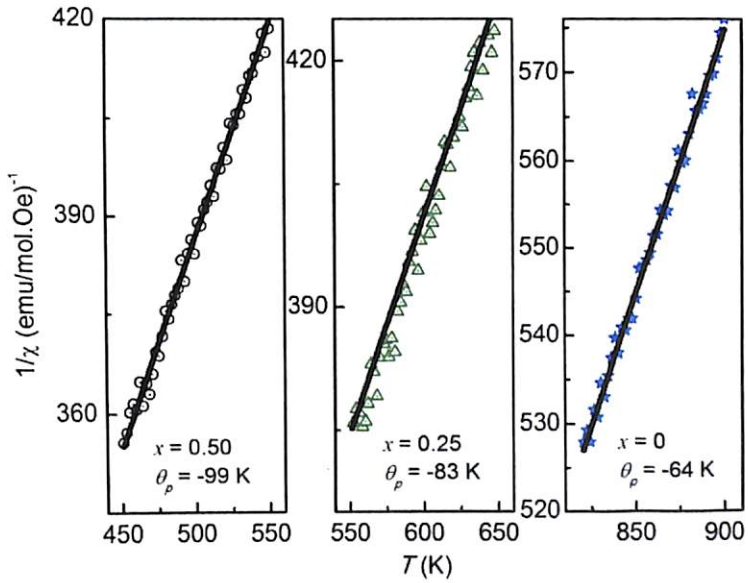

Figure 5.8: Inverse magnetic susceptibility of $(Mn_{1-x}Co_x)_2VGa$ alloys $T > T_C$.

Table 5.5: Saturation magnetic moment (M_s), M_t calculated using nominal composition (M_{Nom}) and EDS measured composition (M_{EDS}), effective anisotropy constant (K_{eff}), Curie temperature (T_C) of $(Mn_{1-x}Co_x)_2VGa$ alloys.

x	M_s (μ_B)	M_{Nom} / M_{EDS} (μ_B)	K_{eff} ($\times 10^4$ Jm^{-3})	T_C (K)
0	1.84	2.00 / 1.86	7.41	768
0.25	0.85	1.00 / 0.92	2.50	478
0.50	0.30	0 / 0.22	0.82	367

Room temperature initial magnetization and *M-H* loops obtained for all the alloy compositions are shown in Figure 5.9(a,b). According to the S-P rule, Mn_2VGa alloy should have M_t = -2μ_B due to anti-parallel alignment of the Mn and V moments. Since the Co moments prefer parallel alignment with V moments and Mn moment align antiparallel with the V moment, M_t gets reduced with Co substitution [QFLI12a]. M_s recorded for the alloys

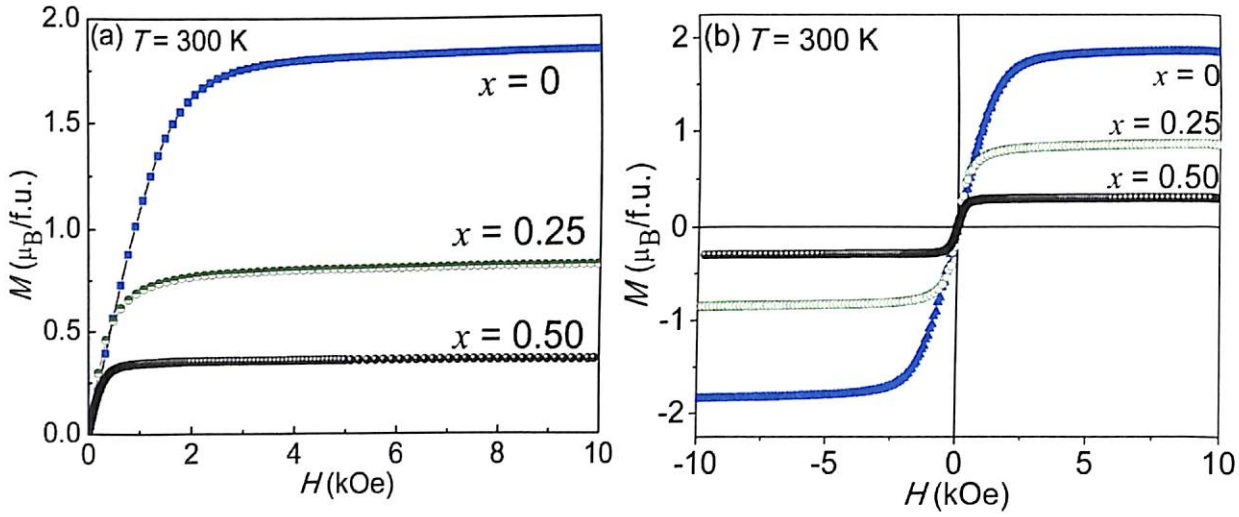

Figure 5.9: (a) Variation of initial magnetization (*M*) with applied magnetic field (*H*) and (b) Complete *M-H* curves for $(Mn_{1-x}Co_x)_2VGa$ alloys.

with x = 0, 0.25 and 0.50 are 1.84μ_B, 0.85μ_B and 0.30μ_B, respectively, while their corresponding value predicted by S-P rule are 2.00μ_B, 1.00μ_B and 0μ_B, respectively. The S-P rule merely considers the total number of valence electrons in the full Heusler alloy to predict the M_t values mentioned above. The limitation of this simple rule is evident when one compares the M_t values of 1.97μ_B, 0.97μ_B and 0.12μ_B, respectively, predicted for the respective alloy compositions by *ab initio* calculations based on GGA[QFLI12a]. The other factor one has to bear in mind is the actual composition of the alloy for which the saturation magnetization has been measured would be different from the nominal composition on which

the S-P and *ab initio* predictions are based on. This report also indicates high spin polarization (P) of 95% and 94% for the alloys with $x = 0$ and 0.25, respectively. For $x = 0$ and $x = 0.25$ alloys, the deviation in measured M_s from both the S-P rule and *ab initio* prediction can be explained on the basis of small variations in stoichiometry (*cf.* Table 5.4) and the possible presence of small amount of X-Z disorder as reported in case of Mn_2VGa [CKLE13a] and Mn_2VAl [MMEI11a] compounds, which reduces the Mn moment because of antiferromagnetic coupling between the Mn antisites. For the alloy with $x = 0.5$, the S-P rule predicts $M_t = 0\mu_B$ since the alloy has $Z_t = 24$. However, *ab initio* calculation [QFLI12a] performed on MnCoVGa alloy with the nominal $L2_1$ unit cell with appropriate elements in their Wycoff positions predicts a M_t of $0.12\mu_B$ with Fermi level lying in the deep region of valence bands with reduced spin polarization of $P = 34\%$. Additionally, the *ab initio* studies reveal a change in the sign of M_t from negative (characteristic of ferrimagnetic Heusler alloys) to positive (characteristic of ferromagnetic Heusler alloys) values for alloys with $x \geq 0.5$. But, Z_t estimated from the EDS data for this alloy composition in our studies, *viz.*, $Mn_{0.98}Co_{0.95}V_{1.08}Ga_{0.99}$ is 23.78 with corresponding M_t of $-0.22\mu_B$ as per S-P rule. We prepared a few more alloys with same nominal composition which resulted in alloys with actual compositions of $Mn_{0.97}Co_{0.92}V_{1.09}Ga_{1.02}$ ($Z_t \approx 23.6$) and $Mn_{0.98}Co_{0.93}V_{1.09}Ga_{1.0}$ ($Z_t \approx 23.7$) as indicated by EDS analysis. M_s value obtained for these ferromagnetic alloys from M-H measurements are $0.48\mu_B$ and $0.40\mu_B$, respectively. Thus, Z_t variation from 23.6 to 23.8 decreases M_s by $0.18\mu_B$. Figure 5.10 shows the variation of M_s values predicted by the *ab initio* calculations (open circles) [QFLI12a] and those obtained experimentally with different Z_t's (filled squares). It is evident from the figure that the experimental M_s values between $Z_t = 23$ and $Z_t = 24$, deviate from the theoretical prediction. This deviation could be attributed to the presence of Mn(Co)-Ga type intersite disorder in the synthesized alloys as observed

earlier [CKLE13a]. Linear fit to the experimental M_s versus Z_t data for $Z_t \geq 23$ shows that $M_s = 0\mu_B$ for an alloy composition with $Z_t = 24.1$. Though, it is extremely difficult to synthesize an alloy with such precise Z_t value, the above reasoning confirms the possibility of obtaining a FCF in alloys with $Z_t = 24.1$. 100% spin polarization predicted for $(Mn_{1-x}Co_x)_2VGa$ alloys with $x > 0.5$ indicate that this alloy composition can exhibit high spin polarization.

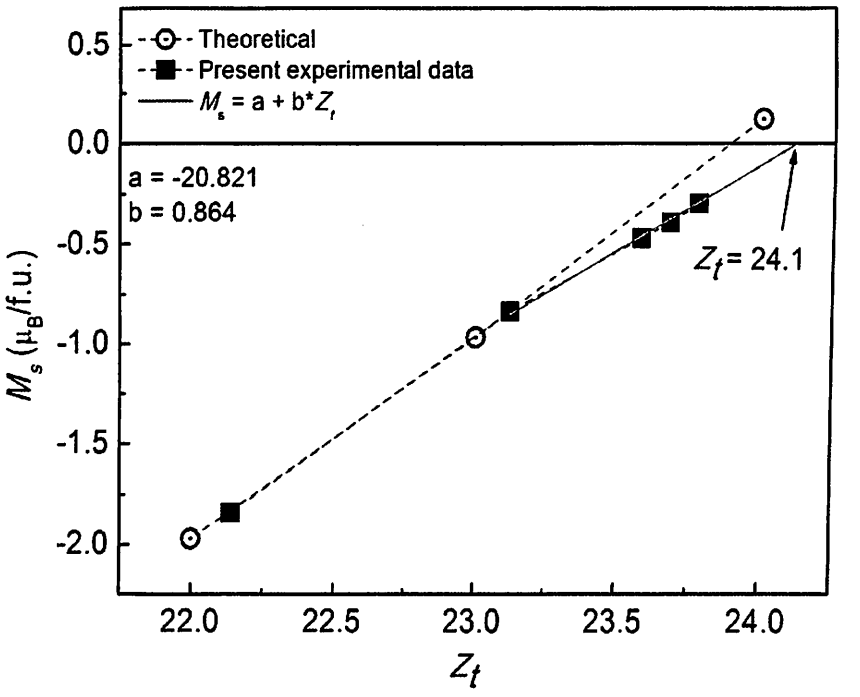

Figure 5.10 Saturation magnetization (M_s) values predicted by *ab initio* calculations [QFLI12a] and those obtained experimentally for alloys with different Z_t's.

K_{eff} values for the alloys were calculated from the *M-H* data depicted in Figure 5.9. K_{eff} was found to decrease with increase in x. K_{eff} value for $x = 0$, 0.25 and 0.5 are 7.41×10^4 Jm^{-3}, 2.50×10^4 Jm^{-3} and 0.82×10^4 Jm^{-3}, respectively. These alloys too exhibit relatively low K_{eff} as compared to typical Heusler alloys, in line with $(Mn_{1-x}Co_x)_2VAl$ alloys.

5.4 Summary

In this chapter, structural, magnetic and half-metallic properties of bulk $(Mn_{1-x}Co_x)_2VAl$ and $(Mn_{1-x}Co_x)_2VGa$ alloys have been investigated. Some of the important results obtained from these studies are as follows:

1. All alloys exhibit the stable $L2_1$ structure of full Heusler alloys.
2. T_C decreases with increase in x because of appearance of antiferromagnetic interaction between Mn and Co atoms in both the series of alloys.
3. Analysis of temperature dependent inverse susceptibility data above T_C confirms ferrimagnetic nature of all the samples.
4. Measured M_s of the alloys shows some deviation from M_t value predicted by S-P rule and *ab initio* calculations. Variation in sample stoichiometry from the nominal composition and the presence of small amount of Mn(Co)-Z disorder in the alloys could account for this deviation in M_s from the theoretically predicted value.
5. Intrinsic spin polarization and magnetic properties of $(Mn_{1-x}Co_x)_2VAl$ alloys show that MnCoVAl alloy composition is a half metallic FCF. Co substitution for Mn in Mn_2VAl increases the instrinsic spin polarization (*i.e.*, half-metallic character).
6. For $(Mn_{1-x}Co_x)_2VGa$ alloys, the lowest magnetic moment value of $0.3\mu_B$ was obtained for the alloy with composition $Mn_{0.98}Co_{0.95}V_{1.08}Ga_{0.99}$ with $Z_t \approx 23.8$.
7. Analysis of M_s versus Z_t data shows that a FCF with zero moment could be expected in $(Mn_{1-x}Co_x)_2VGa$ system for an alloy with $Z_t = 24.1$.

Chapter 6

CONCLUSION AND SCOPE FOR FUTURE WORK

6.1. Conclusion

In this thesis, selected ternary and quaternary full Heusler alloys based on 3d and 4d transition metals have been investigated. Ferromagnetic $Co_2FeGe_{1-x}Si_x$ and $Co_2FeGa_{1-x}Si_x$ were chosen based on reports in the literature on the use of cobalt based alloys in magneto-resistive devices. $Ru_2FeSi_{1-x}Ge_x$ and $(Ru_{1-x}Co_x)_2FeSi$ alloy were investigated due to the possibility of obtaining both antiferromagnet and ferromagnet in the same system which can lead to an all Heusler alloy based spin valve. $(Mn_{1-x}Co_x)_2VAl$ and $(Mn_{1-x}Co_x)_2VGa$ alloys were studied due to the growing demand for Heusler alloys with low or no stray fields. Most of the results presented through these investigations are new which would be of interest not only from the fundamental view point of understanding the effect of structure, disorder and compositional dependence of magnetic and half-metallic properties of these alloys but also from the application aspect. Some of the salient results obtained and conclusions drawn from the current thesis work are mentioned below:

In $Co_2FeZ_{1-x}Si_x$, (Z = Ge, Ga and $0 \leq x \leq 1$) series of alloys, Co_2FeSi alloy crystallizes in $L2_1$ structure but super-lattice reflections are absent in the XRD patterns of the alloys with high Ge and Ga concentrations due to nearly equal scattering factors of Co, Fe, Ge and Ga. The Rhodes-Wohlfarth (R-W) ratio for all the alloys is less than unity indicating half-metallic character in these alloys. In the alloy series with Z = Ge, M_s of the alloy with $x = 0$ follows the S-P rule. However with increase in Si content, M_s deviates from the value predicted by the S-P rule. For the alloy series with Z = Ga, M_s of alloys with $x = 0$, 0.25 and 0.50 follow the predictions of S-P rule, but M_s of alloys with $x = 0.75$ and 1.00 deviate from this rule. This deviation from the S-P rule can be attributed to the presence of DO_3 disorder in the alloys as revealed by *ab initio* studies. For the

series with Z = Ge, on-site Coulomb exchange parameter U need to be considered in the calculation to get the moment predicted by S-P rule. When DO_3 disorder is introduced, the magnetic moment decreases for all alloys except the alloy with $x = 0$, as observed experimentally. DOS calculations show that half-metallicity can be retained in $Co_2FeGe_{1-x}Si_x$ alloys despite the presence of DO_3 disorder and the presence of Ge has a strong stabilizing effect on the electronic structure at the Fermi level and hence the half-metallicity of these alloys. For the series with Z = Ga, total magnetization is accurately predicted by the GGA and gets overestimated by the inclusion of U for alloys with $x \leq 0.25$, which indicates that the electron repulsion is less dominant in alloys with high Ga concentration. Contrary to the alloys with ordered $L2_1$ structure, half-metallicity was destroyed in all the alloys except the alloy with $x = 0.75$ when 12.5% DO_3 disorder was introduced in the $L2_1$ unit cell. Half-metallic character and high degree of $L2_1$ order in these alloys were ascertained by using both *ab initio* and magnetization studies. High effective anisotropy constant ($K_{eff} = 1.12 \times 10^6$ Jm^{-3}) observed in bulk Co_2FeSi alloy points towards possible application of the thin film form of this alloy in magnetic media development.

Though $Ru_2FeSi_{1-x}Ge_x$ alloys do not exhibit the (111) super-lattice reflection due to the nearly equal scattering factors of Fe and Ge atoms, *ab initio* studies show that ferromagnetism exhibited by the alloys with $x > 0$ cannot be possible without these alloys possessing a highly ordered $L2_1$ structure. Ru_2FeSi alloy shows antiferromagnetic behavior with T_N = 270 K. As Ge concentration is increased, the strength of ferromagnetic interactions increases as depicted by an increase in T_C. Variation of Heisenberg exchange integral with interatomic distance for the alloys shows strong

ferromagnetic first nearest neighbor (NN) interaction between the Fe atoms in the ordered $L2_1$ structure resulting in ferromagnetic behavior in the alloys for $x > 0$. However for B2 disordered Ru_2FeSi alloy, second NN interaction between the Fe atoms sitting in the 4a and 4b positions interact antiferromagnetically, resulting in antiferromagnetism in this alloy. When Co was substituted for Ru in $(Ru_{1-x}Co_x)_2FeSi$ system, Ru rich compositions i.e., $x = 0$ and $x = 0.25$ exhibited disordered B2 structure, but with increase in Co concentration $L2_1$ ordering appeared in the alloys. M_s for the alloys with $x = 0.50$, 0.75 and 1.00 are lower than the predicted values, possibly due to DO_3 disorder present in the alloys. Possibility of obtaining alloys with antiferromagnetic as well as ferromagnetic interactions of different strengths is shown by these studies on the two series of alloys. R-W ratio for the alloys containing Ru is found to be greater than unity, indicating the absence of half-metallic character in these alloys.

$(Mn_{1-x}Co_x)_2VZ$ (Z = Al, Ga and $x = 0$, 0.25 and 0.50) alloys crystalize in highly ordered $L2_1$ structure. Due to appearance of antiferromagnetic interaction between Mn and Co atoms, T_C of the alloys was found to decrease with increase in x. M_s of the alloys deviates from the values predicted by S-P rule because of weaker hybridization between Co–V states as compared to that of Mn–V states. Co substitution for Mn in Mn_2VZ decreases M_s and leads to a FCF for the composition with equal amounts (mol%) of Co and Mn i.e. in MnCoVAl/Ga alloy. Spin polarization studies carried on this alloy system for the first time, identify the FCF composition to be half-metallic with an intrinsic spin polarization of 0.60.

6.2. Scope for future work

The present investigations on ternary and quaternary Heusler alloys show how the structural, magnetic and half-metallic properties of these alloys could be tailored by atomic substitution and variation in atomic disorder. There is still a lot of scope for exploring the effect of various other substituents in these full Heusler compounds.

Ge stabilizes half-metallicity in $Co_2FeGe_{1-x}Si_x$ alloys and hence thin films of these alloys are potential materials for fabricating GMR and TMR devices. Bulk Co_2-based alloys have high K_{eff} values which can improve further in their nano-granular form. Hence, studies on thin films of these alloys would help in harnessing their properties for device applications.

Recently, T_N as high as 353 K [NFUK13a] has been reported in antiferromagnetic epitaxial thin films of Ru_2MnGe. In this context, it would be interesting to study thin films of Ru based alloys to develop films with high T_N. Similarly, Mn based ferrimagnetic alloys can be further studied in thin film form to realize ferrimagnets and FCF.

Neutron diffraction and X-ray magnetic circular dichroism measurements on the Ru-based and Mn-based alloys would throw more light on our understanding of the antiferromagnetic and ferrimagnetic ordering in these alloys. Nearly equal X-ray structure factors of elements from the same period can reduce the intensity of the super-lattice peaks and hence it is not easy to infer the presence of chemical disorder in such cases. These ambiguities can be resolved if neutron diffraction experiments can be performed on these alloys.

REFERENCES

[AAHA01a] A. Aharoni, Introduction to the theory of ferromagnetism, Oxford (2001).
[AFAN64a] A. F. Andreev, Sov. Phys. JETP 19 (1964) 1228.
[AHAM15a] A. Hamri, Z. Dridi, B. Hamri, A. Hallouche, Int. J. Modern Phys. B 29 (2015) 1550057.
[AJBR34a] A. J. Bradley, J. W. Rodgers, Proc. Royal Soc. A 144 (1934) 340.
[AMAT02a] A. Matsushita, T. Naka, Y. Takanao, T. Takeuchi, T. Shishido, Y. Yamada, Phys. Rev. B 65 (2002) 075204.
[ANIN01a] An introduction to the program fullprof 2000 (Version July 2001).
[ANUR12a] A. Nurbawono, C. Zhang, Sensors 12 (2012) 6049.
[ANVA99a] A. N. Vasilev, A. D. Bozhko, V. V. Khovailo, I. E. Dikshtein, V. G. Shavrov, D. Buchelnikov, M. Matzumoto, S. Suzuki, T. Takagi, J. Tani, Phys. Rev. B 59 (1999) 1113.
[APMA85a] A. P. Malozemoff, Phys. Rev. B 32 (1985) 6080.
[ARAJ07a] A. Rajanikanth, Y. K. Takahashi, K. Hono, J. Appl. Phys. 101 (2007) 023901.
[ARAJ07b] A. Rajanikanth, D. Kande, Y. K. Takahashi, K. Hono, J. Appl. Phys. 101 (2007) 09J508.
[ASZY89a] A. Szytula, H. Ptasiewicz-Bak, J. Leciejewicz, J. Magn. Magn. Mater. 80 (1989) 195.
[BBAL07a] B. Balke, S. Wurmehl, G. H. Fecher, C. Felser, C. Maria, M. Alves, F. Bernardi, J. Morais, Appl. Phy. Lett. 90 (2007) 172501.
[BBAL07b] B. Balke, G.H. Fecher, J. Winterlik, C. Felser, Appl. Phys. Lett. 90 (2007) 152504.
[BDCU01a] B. D. Cullity, S. R. Stock, Elements of X-ray diffraction, 3rd Edition, Pearson Education, Boston (2001).
[BDCU08a] B. D. Cullity, C. D. Graham, Introduction to Magnetic Materials, Wiley-IEEE Press, New Jersey (2008).
[BNIK99a] B. Nikolic, P. B. Allen, Phys. Rev B 60 (1999) 3963.
[BSDC09a] B. S. D. Ch. S. Varaprasad, A. Rajanikanth, Y. K. Takahashi, K. Hono, Acta Mater. 57 (2009) 2702.
[BSDC10a] B.S.D.Ch.S. Varaprasad, A. Rajanikanth, Y.K. Takahashi, K. Hono, Appl. Phys. Exp. 3 (2010) 23002.
[BSDC12a] B.S.D.Ch.S. Varaprasad, A. Srinivasan, Y.K. Takahashi, M. Hayashi, A. Rajanikanth, K. Hono, Acta Mater. 60 (2012) 6257.
[CHOR06a] C. Horst, T. Saito, L. Smith, Springer Handbook of materials measurement methods, Springer, Germany (2006).
[CJIA01a] C. Jiang, M. Venkatesan, J. M. D. Coey, Solid State Commun. 118 (2001) 513.
[CJIA04a] C. Jiang, Y. Muhammad, L. Deng, W. Wu, H. Xu, Acta Materialia 52 (2004) 2779.
[CJIA04a] C. Jiang, Y. Muhammad, L. Deng, W. Wu, H. Xu, Acta Mater. 52 (2004) 2779.
[CKLE13a] C. Klewe, M. Meinert, J. Schmalhorst, G. Reiss, J. Phys.: Condens. Matter 25 (2013) 076001.
[CSTE13a] C. Sterwerf, M. Meinert, J. Schmalhorst, G. Reiss, IEEE Trans. Magn. 49 (2013) 4386.
[CZEN53a] C. Zener, R. Heikes, Rev. Mod. Phys. 25 (1953) 191.
[DBOM13a] D. Bombor, C. G. F. Blum, O. Volkonskiy, S. Rodan, S. Wurmehl, C. Hess, B. Buchner, Phys. Rev. Lett. 110 (2013) 066601.

[DJGR95a] D. J. Griffith, Introduction to Electrodynamics, 2nd ed., Prentice hall, New Delhi (1995).

[DLOU98a] D. Louer, Acta Cryst. A 54 (1998) 922.

[DSHO09a] D. Sholl, J. A. Steckel, Density Functional Theory: A Practical Introduction, John Wiley and sons, Inc., New Jersey (2009)

[EPWO78a] E. P. Wohlfarth, J. Magn. Magn. Mater. 7 (1978) 113.

[ESAI05a] E. Sasioglu, L. M. Sandratskii, P. Bruno J. Phys.: Condens. Matter 17 (2005) 995.

[ESAS05a] E. Sasioglu, L. M. Sandratskii, P. Bruno, J. Phys. Condens. Mat. 17 (2005) 995.

[FCAR00a] F. Cardarelli, Materials Handbook (Springer, London, 2000).

[FGJI99a] F. Gejima, Y. Sutou, R. Kainuma, K. Ishida, Metall. Mater. Trans. A 30 (1999) 2721.

[FHEU03a] F. Heusler, Verh. Dtsch. Phys. Ges. 5 (1903) 219.

[FJJE01a] F. J. Jedema, A. T. Filip, B. J. van Wees, Nature, 410 (2001) 345.

[FJYA12a] F.J. Yang, Y. Sakuraba, S. Kokado, Y. Kota, A. Sakuma, K. Takanashi, Phys. Rev. B 86 (2012) 020409.

[FJYA13a] F. J. Yang, C. Wei, X. Q. Chen, Appl. Phys. Lett. 102 (2013) 172403.

[FWU09a] F. Wu, S. Mizukami, D. Watanabe, H. Naganuma, M. Oogane, Y. Ando, T. Miyazaki, Appl. Phys. Lett. 94 (2009) 122503.

[FWUS09a] F. Wu, S. Mizukami, D. Watanabe, H. Naganuma, M. Oogane, Y. Ando, T. Miyazaki, Appl. Phys. Lett. 94 (2009) 122503.

[FYAN13a] F. Yang, Z. Kang, X. Chen, Y. Xue, J. Phys. D: Appl. Phys. 46 (2013) 325003.

[GEBA71a] G. E. Bacon, J. S. Plant, J. Phys. F: Met. Phys. 1 (1971) 524.

[GEBL82a] G. E. Blonder, M. Tinkham, T. M. Klapwijk, Phys. Rev. B. 25 (1982) 4515.

[GJST01a] G. J. Strijkers, Y. Ji, F. Y. Yang, C. L. Chien, J. M. Byers, Phys. Rev. B 63 (2001) 104510.

[GKRE96a] G. Kresse, J. Furthmüller, Phys. Rev. B 54 (1996) 11169.

[GKRE99a] G. Kresse, D. Joubert, Phys. Rev. B 59 (1999) 1758.

[HASA10a] H. Asano, H. Gotoh, H. Matsushima, Y. Takeda, J. Zhong, A. Rajanikanth, K. Hono, J. Phys. Conf. Series 200 (2010) 052001.

[HCKA06a] H. C. Kandpal, G. H. Feche, C. Felse, G. Schönhense, Phys. Rev. B 73 (2006) 094422.

[HCKA07a] H. C. Kandpal, V. Ksenofontov, M. Wojcik, R. Seshadri, C. Felser, J. Phys. D: Appl. Phys. 40 (2007) 1587.

[HCKA07b] H. C. Kandpal, G. H. Fecher, C. Felser, J. Phys. D: Appl. Phys. 40 (2007) 1507.

[HITO83a] H. Itoh, T. Nakamichi, Y. Yamaguchi, N. Kazama, Trans. Japan Inst. Met. 24 (1983) 265.

[HJMO76a] H. J. Monkhorst, J. D. Pack, Phys. Rev. B 13 (1976) 5897.

[HKAT04a] H. Kato, T. Okuda, Y. Okimoto, Y. Tomioka, K. Oikawa, T. Kamiyama, Y. Tokura, Phys. Rev. B 69 (2004) 184412.

[HKUR11a] H. Kurt, K. Rode, M. Venkatesan, P. Stamenov, J. M. D. Coey, Phys. Rev. B 83 (2011) 020405(R).

[HKUR11b] H. Kurt, K. Rode, M. Venkatesan, P. Stamenov, J. M. D. Coey, Phys. Stat. Solidi B 248 (2011) 2338.

[HLIU12a] H. Liu, Y. Honda, T. Taira, K. Matsuda, M. Arita, T. Uemura, M. Yamamoto, Appl. Phys. Lett. 101 (2012) 132418.

[HLIU15a] H. Liu, T. Kawami, K. Moges, T. Uemura, M. Yamamoto, F. Shi, P. M Voyles, J. Phys. D: Appl. Phys. 48 (2015) 164001.

[HMRI67a] H. M. Rietveld, Acta Cryst. 22 (1967) 151.

[HMRI69a] H. M. Rietveld, Acta Cryst. 2 (1969) 65.

[HNAK88a] H. Nakamura, Y. Kitaoka, K. Asayama, Y. Onuki, T. Komatsubara, J. Magn. Magn. Mater. 76 (1988) 467.

[HNII96a] H. Niida, T. Hori, H. Onodera, Y.Yamaguchi, Y. Nakagawa, J. Appl. Phys. 79 (1996) 5946.

[HOKA08a] H. Okada, K. Koyama, K. Watanabe, Y. Kusakari, T. Kanomata, H. Nishihara, Appl. Phys. Lett. 92 (2008) 062502.

[HPAU68a] H. Pauly, A. Weiss, H. Witte, Z. Metallk 59 (1968) 47.

[HPWI91a] H. P. Wijn, Magnetic Properties of Metals, Springer, Berlin (1991).

[HSGO13a] H. S. Goripati, T. Furubayashi, Y. K. Takahashi, K. Hono, J. Appl. Phys. 113 (2013) 043901.

[HVAN95a] H. van Leuken, R. A. de Groot, Phys. Rev. Lett. 74 (1995) 7.

[IGAL02a] I. Galanakis, Phys. Rev. B 66 (2002) 012406.

[IGAL02b] I. Galanakis, P. Dederichs, N. Papanikolaou, Phys. Rev. B 66 (2002) 174429.

[IGAL02c] I. Galanakis, P. H. Dederichs, N. Papanikolaou, Phys. Rev. B 66 (2002) 134428.

[IGAL03a] I. Galanakis, Ph. Mavropoulos, Phys. Rev. B 67 (2003) 104417.

[IGAL04a] I. Galanakis, J. Phys: Condans. Matter 16 (2004) 3089.

[IGAL07a] I. Galanakis, K. Ozdogan, E. Sasioglu, B. Aktas, Phys. Rev. B 75 (2007) 092407.

[IGAL11a] I. Galanakis, E. Sasioglu, Appl. Phys. Lett. 98 (2011) 102514.

[IKHT14a] Ikhtiar, S. Kasai, A. Itoh, Y. K. Takahashi, T. Ohkubo, S. Mitani, K. Hono, J. Appl. Phys. 115 (2014) 173912.

[IMIM12a] I. M. Imort, P. Thomas, G. Reiss, A. Thomas, J. Appl. Phys. 111 (2012) 07D313.

[JCTU13a] J. C. Tung, G. Y. Guo, New J. Phys. 15 (2013) 033014.

[JKUB07a] J. Kubler, G. H. Fecher, C. Felser, Phys. Rev. B 76 (2007) 024414.

[JKUB83a] J. Kubler, A. Williams, C. Sommers, Phys. Rev. B 28 (1983) 1745.

[JKUB84a] J. K¨ubler, Physica B 127 (1984) 257.

[JMDC04a] J. M. D. Coey , S. Sanvito, Magnetic semiconductors and halfmetals. J. Phys. D: Appl. Phys. 37 (2004) 988.

[[JPPE86a] J. P. Perdew, Y. Wang, Phys. Rev B 33 (1986) 8800.

[JPPE89a] J. P. Perdew, Y. Wang, Phys. Rev B 40 (1989) 3399(E).

[JPPE96a] J. P. Perdew, K. Burke, M. Ernzerhof, Phys. Rev. Lett. 77 (1996) 3865.

[JROG12a] J. Rogge, P. Hedwig, C. Sterwerf, A. Hütten, IEEE Trans. Magn. 48 (2012) 2464.

[JSAT11a] J. Sato, M. Oogane, H. Naganuma, Y. Ando, Appl. Phys. Express 4 (2011) 113005.

[JSVO04a] J. Svoboda, Magnetic Techniques for the treatment of materials, Kluwer Academic Publishers, The Netherlands (2004).

[JWIN08a] J. Winterlik, G. H. Fecher, C. Felser, M. Jourdan, K. Grube, F. Hardy, H. von Lohneysen, K. L. Holman, R. J. Cava, Phys. Rev. B 78 (2008) 184506.

[KEHM90a] K. E. H. M. Hanssen, P. E. Mijnarends, L. P. L. M. Rabou, K. H. J. Buschow, Phys. Rev. B 42 (1990) 1533.

[KHAM12a] K. Hamaya, N. Hashimoto, S. Oki, S. Yamada, M. Miyao, T. Kimura, Phys. Rev. B 85 (2012) 100404(R).
[KHJB81a] K. H. J. Buschow, P. G. van Engen, J. Magn. Magn. Mater. 25 (1981) 90.
[KHJB83a] K. H. J. Buschow, P. G. van Engen, R. Jongebreur, J. Magn. Magn. Mater. 38 (1983) 1.
[KMAT05a] K. Matsuda, M. Hiroi, M. Kawakami, J. Phys: Condens. Matter 17 (2005) 5889.
[KNIK09a] K. Nikolaev, P. Kolbo, T. Pokhil, X. Peng, Y. Chen, T. Ambrose, O. Mryasov, Appl. Phys. Lett. 94 (2009) 222501.
[KOIK01a] K. Oikawa, L. Wulff, T. Iijima, F. Gejima, T. Ohmori, A. Fujita, K. Fukamichi, R. Kainuma, K. Ishida, Appl. Phys. Lett. 79 (2001) 3290.
[KOIK01b] K. Oikawa, T. Ota, F. Gejima, T. Ohmori, R. Kainuma, K. Ishida, Mater. Trans. 42 (2001) 2472.
[KOIK02a] K. Oikawa, T. Ota, Y. Sutou, T. Ohmori, R. Kainuma, K. Ishida, Mater. Trans. 43 (2002) 2360.
[KOIK02b] K. Oikawa, T. Ota, T. Ohmori, Y. Tanaka, H. Morito, A. Fujita, R. Kainuma, K. Fukamichi, K. Ishida, Appl. Phys. Lett. 81 (2002) 5201.
[KOZD06a] K. Ozdogan, I. Galanakis, E. Sasioglu, B. Aktas, J. Phys.: Condens. Matter 18 (2006) 2905.
[KRAZ01a] K. R. A. Ziebeck, K.-U. Neumann. Springer, Berlin, 2001, pp. 64 314.
[KRKU08a] K. R. Kumar, N. H. Kumar, G. Markandeyulu, J. A. Chelvane, V. Neu, P. D. Babu, J. Magn. Magn. Mater. 320 (2008) 2737.
[KRKU09a] K. R. Kumar, K. K. Bharathi, J. A. Chelvane, S. Venkatesh, G. Markandeyulu, N. Harishkuma, IEEE Trans. Magn. 45 (2009) 10.
[KRKU10a] K. R. Kumar, J. A. Chelvane, G. Markandeyulu, S. K. Malik, N. H. Kumar, Solid State Commun. 150 (2010) 70.
[KULL96a] K. Ullakko, J. K. Huang, C. Kantner, R. C. O'Handley, V. V. Kokorin, Appl. Phys. Lett. 69 (1996) 1966.
[KULL97a] K. Ullakko, J. K. Huang, V. V. Kokorin, R. C. O'Handley, Scripta Mater. 36 (1997) 1133.
[KWAT76a] K.Watanabe, Trans. Jpn. Inst. Met. 17 (1976) 220.
[LGUA10a] L. Guan-Nan, J. Ying-Jiu, L. Jae, Chin. Phys. B 19 (2010) 097102.
[LHTH27a] L. H. Thomas, Proc. Camb. Phil. Soc. 23 (1927) 542.
[LJSI04a] L. J. Singh, Z. H. Barber, Y. Miyoshi, Y. Bugoslavsky, W. R. Branford, L. F. Cohen, Appl. Phys. Lett. 84 (2004) 2367.
[LMAK13a] L. Makinistian, M. M. Faiz, R. P. Panguluri, B. Balke, S. Wurmehl, C. Felser, E. A. Albanesi, A. G. Petukhov, B. Nadgorny, Phys. Rev. B 87 (2013) 220402(R).
[MHAK13a] M. Hakimi, M. Venkatesan, K. Rode, K. Ackland, J. M. D. Coey, J. Appl. Phys. 113 (2013) 17B101.
[MHOR04a] M. Horne, P. Strange, W.M. Temmerman, Z. Szotek, A. Svane, H.Winter, J. Phys.: Condens. Matt. 16 (2004) 5061.
[MJHA04a] M. Zhang, E. Bruck, F. R. de Boer, Z. Li, G. Wu, J. Phys. D: Appl. Phys. 37 (2004) 2049.
[MJMD95a] M. J. M. de Jong, C. W. J. Beenakker, Phys. Rev. Lett. 74 (1995) 1657.
[MJOT89a] M. J. Otto, R. A. M. van Woerdenl, P. J. van der Valkt, J. Wijngaardl, C. F. van Bruggent, C. Haasl, K. H. J. Buschow, J. Phy. : Cond. Matter. 1(1989) 2341.

[MKAW81a] M. Kawakami, Y. Yoshida, T. Nakamichi, S. Ishida, H. Enokiya, J. Phys. Soc. Japan 50 (1981) 1041.
[MMEI11a] M. Meinert, J. M. Schmalhorst, G. Reiss, E. Arenholz, J. Phys. D: Appl. Phys. 44 (2011) 215003.
[MOOG09a] M. Oogane, M. Shinano, Y. Sakuraba, Y. Ando, J. Appl. Phys. 105 (2009) 907C903.
[MPUS69a] M. Puselj, Z. Ban. Croat. Chem. Acta, 41 (1969) 79.
[MWUT01a] M. Wuttig, J. Li, C. A. Craciunescu, Scripta Mater. 44 (2001) 2393.
[MZHA04a] M. Zhang, E. Bruck, F. R de Boer, Z. Li, G. Wu, J. Phys. D: Appl. Phys. 37 (2004) 2049.
[MZIE00a] M. Ziese, Phys. Rev. B 62 (2000) 1044.
[NFUK13a] N. Fukatani, H. Fujita,T. Miyawaki,K. U. H. Asano, J. Korean Phys. Soc. 63 (2013) 711.
[NLAK02a] N. Lakshmi, A. Pandey, K. Venugopalan, Bull. Mater. Sci. 25 (2002) 309.
[NPDU07a] N. P. Duong, L. T. Hung, T. D. Hien, N. P. Thuy, N. T. Trung, E. Bruck, J. Magn. Magn. Mater. 311 (2007) 605.
[OHEU34a] O. Heusler, Ann. Phys. 155 (1934) 411.
[PBRU91a] P. Bruno, C. Chappert, Phys. Rev. Lett. 67 (1991) 1602.
[PGDE66a] P. G. de Gennes, Superconductivity in metals and alloys, W. A. Benjamin, New York 1966.
[PGRU86a] P. Grunberg, R. Schreiber, Y. Pang, M. B. Brodsky, H. Sowers, Phys. Rev. Lett. 57 (1986) 2442.
[PGVA83a] P. G. van Engen, K. H. J. Bushow, R. Jongebreuer, M. Erman , Appl. Phys. Lett. 42 (1983) 202.
[PHOH64a] P. Hohenberg, W. Kohn, Phys. Rev. 136 (1964) 3864.
[PJWE69a] P. J. Webster, Contemp. Phys. 10 (1969) 559.
[PJWE73a] P. J. Webster, K. R. A. Ziebeck, J. Phys. Chem. Solids 34 (1973) 1647.
[PJWE81a] P. J. Webster, J. Appl. Phys. 52 (1981) 2040.
[PJWE84a] P. J. Webster, K. R. A. Ziebeck, S. L. Town, M. S. Peak, Philos. Mag. B 49 (1984) 295.
[PJWE88a] P. J. Webster, K. R. A. Ziebeck, in Alloys and Compounds of d-Elements with Main Group Elements, Part 2, edited by H. P. J. Wijn, Landolt-B¨ornstein, New Series, Group III, Vol. 19/c (Springer, Berlin, 1988), pp. 75-184.
[PMTE94a] P. M. Tedrow, R. Meservey, Phys. Rep. 238 (1994) 173.
[QDQI06a] Q. D. Qin, Y. G. Zhao, P. J. Cong, Y. H. Liang, W. J. Zhou, J. Alloys Compd. 420 (2006) 121.
[QFLI12a] Q. F. Li, H. F. Zhao, X. Zhong, J. L. Su, J. Magn. Magn. Mater. 324 (2012) 1463.
[RADE83a] R. A. de Groot, F. M. Mueller, P. G. van Engen, K. H. J. Buschow, Phys. Rev. Lett. 50 (1983) 2024.
[RADE91a] R.A. de Groot, Physica B 172 (1991) 45.
[RCAR00a] R. Carey, D. M. Newman, M. L. Wears, Phys Rev B 62 (2000) 1520e3.
[RDAS11a] R. Das, A. Perumal, A. Srinivasan, IEEE Trans. Magn. 47 (2011) 2463.
[RDAS13a] R. Das, A. Perumal, A. Srinivasan, J. Alloys Compd. 572 (2013) 192.
[RDAS13b] R. Das, P. Saravanan, D. Arvindha Babu, A. Perumal, A. Srinivasan, J. Magn. Magn. Mater. 344 (2013) 152.
[RFED85a] R. Feder, Ed., Polarized Electrons in Surface Physics, (World Scientific, Singapore, 1985).

[RJSO98a] R. J. Soulen, Jr. J. M. Byers, M. S. Osofsky, B. Nadgorny, T. Ambrose, S. F. Cheng, P. R. Broussard, C. T. Tanaka, J. Nowak, J. S. Moodera, A. Barry, J. M. D. Coey, Science 282 (1998) 85.

[RKAI06a] R. Kainuma, Y. Imano, W. Ito, Y. Sutou, H. Morito, S. Okamoto, O. Kitakami, K. Wikiwa, A. Fujita, T. Kanomata, K. Ishida, Nature 439 (2006) 957.

[RKAI96a] R. Kainuma, M. Ise, C. C. Jia, H. Ohtani, K. Ishida, Intermetallics 4 (1996) S151.

[RMA14a] R. Ma, Q. Xie, J. Huang, Intermetallics 46 (2014) 12e17.

[RMOH15a] R. Mohankumar, S. Ramasubramanian, M. Rajagopalan, M. Manivel Raja, S. V. Kamat, J. Kumar, J. Mater Sci. 50 (2015) 1287.

[RYUM12a] R. Y. Umetsu, A. Okubo, R. Kainuma, J. Appl. Phys. 111 (2012) 073909.

[SBLU01a] S. Blundell, Magnetism in Condensed Matter, oxford university press, New York, 2001.

[SCHA09a] S. Chadov, G. H. Fecher, C. Felser, J. Minar, J. Braun, H. Ebert, J. Phys. D: Appl. Phys. 42 (2009) 084002.

[SIFU95a] S. I. Fujii, A. S. Shoji, J. Phys. Soc. Jpn. 64 (1995) 6.

[SISH78a] S. Ishida, J. Ishida, S. Asano, J. Yamashita, J. Phys. Soc. Jpn. 45 (1978) 1239.

[SISH80a] S. Ishida, Y. Kubo, J. Ishida, S. Asano, J. Phys. Soc. Jpn. 48 (1980) 814.

[SISH95a] S. Ishida, S. Fujii, S. Kashiwagi, S. Asano, J. Phys. Soc. Jpn. 64 (1995) 2152.

[SKCL04a] S. K. Clowes, Y. Miyoshi, O. Johannson, B. J. Hickey, C. H. Marrows, M. Blamire, M. R. Branford, Y. V. Bugoslavsky, L. F. Cohen. J. Magn. Magn. Mater. 272 (2004) 1471.

[SKHO09a] S. Khosravizadeh, S. J. Hashemifar, H. Akbarzadeh, Phys. Rev. B 79 (2009) 235203.

[SLDU98a] S. L. Dudarev, G. A. Botton, S. Y. Savrasov, C. J. Humphreys, A. P. Sutton, Phys. Rev. B 57 (1998) 1505.

[SMIZ09a] S. Mizusaki, T. Ohnishi, A. Douzono, Y. Nagata, T. C. Ozawa, H. Samata, Y. Noro, J. Appl. Phys. 105 (2009) 07E513.

[SMIZ10a] S. Mizusaki, A. Douzono, T. Ohnishi, Y. Nagata, T.C. Ozawa, H. Samata, Y. Noro, J. Phys. Conf. Series 200 (2010) 052017.

[SNMI85a] S. N. Mishra, D. Rambabu, A. K. Grover, P. N. Tandon, J. Magn. Magn. Mater. 51 (1985) 359.

[SOKI12a] S. Oki, K. Masaki, N. Hashimoto, S. Yamada, M. Miyata, M. Miyao, T. Kimura, K. Hamaya, Phys. Rev. B 86 (2012) 174412.

[SOKI13a] S. Oki, S. Yamada, K. Tanikawa, K. Yamasaki, M. Miyao, K. Hamaya, Appl. Phys. Lett. 103 (2013) 212402.

[SPIC02a] S. Picozzi, A. Continenza, A. Freeman, Phys. Rev. B 66 (2002) 094421.

[SPIC04a] S. Picozzi, A. Continenza, A. J. Freeman, Phys. Rev. B 69 (2004) 094423.

[SSAK05a] S. Sakurada, N. Shutoh, Appl. Phys. Lett. 86 (2005) 082105e8.

[SSAR11a] S. Sarma and A. Srinivasan, AIP Conf. Proc. 1347 (2011) 111.

[SVAN97a] S. V. Andreev, M. I. Bartashevich, V. I. Pushkarsky, V. N. Maltsev, A. Pamyatnykh, E. N. Tarasov, N. V. Kudravatykh, T. J. Goto, Alloys Compd. 260 (1997) 196.

[SVKA06a] S.V. Karthik, A. Rajanikanth, Y.K. Takahashi, T. Ohkubo, K. Hono, Appl. Phys. Lett. 89 (2006) 052505.

[SVKA07a] S. V. Karthik, A. Rajanikanth, T. M. Nakatani, Z. Gercsi, Y. K. Takahashi, T. Furubayashi, K. Inomota, K. Hono, J. Appl. Phys. 102 (2007) 043903.

[SVKA07b] S. V. Karthik, A. Rajanikanth, Y. K. Takahashi, T. Ohkubo, K. Hono, Acta. Mater. 55 (2007) 3867.

[SWUR05a] S. Wurmehl, G. H. Fecher, H. C. Kandpal, V. Ksenofontov, C. Felser, H. J. Lin, Morais, J. Phys. Rev. B 72 (2005) 184434.

[SWUR06a] S. Wurmehl, G. H. Fecher, H. C. Kandpal, V. Ksenofontov, C. Felsera, H. Lin, Appl. Phy. Lett. 88 (2006) 032503.

[TAKA83a] T. Nakamichi, C. V. Stager, J. Magn. Magn. Mater. 31 (1983) 85.

[TGRA09a] T. Graf, F. Casper, J. Winterlik, B. Balke, G. H. Fecher, C. Felser, Z. Anorg, Allg. Chem. 635 (2009) 976.

[TGRA11a] T. Graf, C. Felser, S. S. P. Parkin, Prog. Solid St. Chem. 39 (2011) 50.

[TKAN06a] T. Kanomata, M. Kikuchi, H. Yamauchi, J. Alloys Compd. 414 (2006) 1.

[TKRE05a] T. Krenke, E. Duman, M. Acet, E. F. Wassermann, X. Moya, L. Ma˜nosa, A. Planes, Nat. Mater. 4 (2005) 450.

[TKRE07a] T. Krenke, E. Duman, M. Acet, E. F. Wassermann, X. Moya, L. Mañosa, A. Planes, E. Suard, B. Ouladdiaf, Phys. Rev. B 75 (2007) 104414.

[TKUB09a] T. Kubota, K. Kodama, T. Nakamura, Y. Sakuraba, M. Oogane, K. Takanashi, Y. Ando, Appl. Phys. Lett. 95 (2009) 222503.

[TMNA07a] T. M. Nakatani, A. Rajanikanth, Z. Gercsi, Y. K. Takahashi, K. Inomata, K. Hono, J. Appl. Phys. 102 (2007) 033916.

[TMNA10a] T. M. Nakatani, T. Furubayashi, S. Kasai, H. Sukegawa, Y. K. Takahashi, S. Mitani, K. Hono, Appl. Phys. Lett. 96 (2010) 212501.

[TMNA12a] T. M. Nakatani, N. Hase, H. S. Goripati, Y. K. Takahashi, T. Furubayashi, K. Hono, IEEE Trans. Magn. 48 (2012) 1751.

[TMNA13a] T.M. Nakatani, Ye Du, Y.K. Takahashi, T. Furubayashi, K. Hono, Acta Mater. 61 (2013) 3695.

[TSCH14a] T. Scheike, H. Sukegawa, T. Furubayashi, Z. Wen, K. Inomata, T. Ohkubo, K. Hono, S. Mitan, Appl. Phys. Lett. 105 (2014) 242407.

[TSHI01a] T. Shishidou, A.J. Freeman, R. Asahi, Phys. Rev. B 64 (2001) 180401.

[VKSE10a] V. Ksenofontov, M. Wojcik, S. Wurmehl, H. Schneider, B. Balke, G. Jakob, C. Felser, J. Appl. Phys. 107 (2010) 09B106.

[VNIC77a] V. Niculescu, T. J. Burch, K. Rai, J. I. Budnick, J. Magn. Magn. Mater. 5 (1977) 60.

[VSPA83a] V. S. Patil, R. G. Pillay, P. N. Tandon, H. G. Devare, Phys. Stat. Sol. (b) 118 (1983) 57.

[VVSU90a] V. V. Surikov, V. N. Zhordochkin, T. Y. Astakhova, Hyperfine Interact. 59 (1990) 469.

[WEPI96a] W. E. Pickett, Phys. Rev.Lett. 77 (1996) 3185.

[WFER13a] W. Ferng, Y. Shin, S. Cho, D. D. Dung, J. Korean Phys. Soc., 63 (2013) 1055.

[WKOH65a] W. Kohn, L. J. Sham, Phys. Rev. 140 (1965) A1133.

[WSYU12a] W. S. Yun, G. Cha, I. G. Kim, S. H. Rhim, S. C. Hong, J. Phys.: Condens. Matter 24 (2012) 416003.

[WWWNa] www.nims.go.jp/apfim/halfmetal.html

[WWWNb] www.nims.go.jp/apfim/PCAR.html

[XYXI01a] X. Y. Xiong, T. R. Finlayson, B. C. Muddle, J. Phys. D: Appl. Phys. 34 (2001) 2845.

[YFUK11a] Y. Fukuma, L. Wang, H. Idzuchi, S. Takahashi, S. Maekawa, Y. Otani, Nature Mater. 10 (2011) 527.

[YKTA11a] Y.K. Takahashi, A. Srinivasan, B. Varaprasad, A. Rajanikanth, N. Hase, T.M. Nakatani, S. Kasai, T. Furubayashi, K. Hono, Appl. Phys. Lett. 98 (2011) 152501.

[YKTA12a] Y. K. Takahashi, S. Kasai, S. Hirayama, S. Mitani, K. Hono, Appl. Phys. Lett. 100 (2012) 052405.

[YKTA13a] Y. K. Takahashi, N. Hase, M. Kodzuka, A. Itoh, T. Koganezawa, T. Furubayashi, S. Li, B. S. D. Ch. S. Varaprasad, T. Ohkubo, K. Hono, J. Appl. Phys. 113 (2013) 223901.

[YKUS07a] Y. Kusakari, T. Kanomata, K. Fukushima, H. Nishihara, J. Magn. Magn. Mater. 310 (2007) e607.

[YLEN08a] Y. Leng, J. Wiley & Sons (Asia) Pvt. Ltd., Singapore (2008).

[YMIU04a] Y. Miura, K. Nagao, M. Shirai, Phys. Rev. B 69 (2004) 144413.

[YNIS11a] Y Nishino, IOP Conf. Series: Mat. Sci. Eng. 18 (2011) 142001.

[YNIS97a] Y. Nishino, M. Kato, S. Asano, K. Soda, M. Hayasaki, U. Mizutani, Phys. Rev. Lett. 79 (1997) 1909.

[YSAK06a] Y. Sakuraba, M. Hattori, M. Oogane, Y. Ando, H. Kato, A. Sakuma, T. Miyazaki, H. Kubota, Appl. Phys. Lett. 88 (2006) 192508.

[YSAK10a] Y. Sakuraba, K. Izumi, T. Iwase, S. Bosu, K. Saito, K. Takanashi, Phy. Rev. B 82 (2010) 094444.

[YSAK13a] Y. Sakuraba, K. Izumi, T. Koganezawa, S. Bosu, R. Okura, M. Ueda, T. Kojima, K. Saito, K. Takanashi, IEEE Trans. Magn. 49 (2013) 2464.

[YTAK08a] Y. Takamura, R. Nakane, H. Munekata, S. Sugahara, J. Appl. Phys. 103 (2008) 07D719.

[YWU13a] Y. Wu, J. Zhang, Q. Xiong, S. Gao, X. Xu, J. Miao, Z. He, Y. Jiang, Appl. Phys. Expr. 6 (2013) 113003.

[YYOS81a] Y. Yoshida, M. Kawakami, T. Nakamichi, J. Phys. Soc. Japan 50 (1981) 2203.

[ZGER06a] Z. Gercsi, A. Rajanikanth, Y. K. Takahashi, K. Hono, M. Kikuchi, N. Tezuka, K. Inomota, Appl. Phys. Lett. 89 (2006) 082512.

[ZGER07a] Z. Gercsi, K. Hono, J. Phys.: Cond. Matt. 19 (2007) 326216.

[ZQJI98a] Z. Q. Jin, W. Tang, J. R. Zhang, H. X. Qin, Y.W. Du, Phys. J. B 3 (1998) 41.

[ZWEN12a] Z. Wen, H. Sukegawa, S. Kasai, M. Hayashi, S. Mitani, K. Inomata, App. Phys. Exp. 5 (2012) 063003.

Publications in journals originating from the thesis work:

1. Magnetic properties of Ge substituted Ru_2FeSi alloys,
   Bhargab Deka, Rahul Das and A. Srinivasan, **J. Magn. Magn. Mater.** 347 (2013) 101.

2. Magnetic properties of $Co_2Fe(Ga_{1-x}Si_x)$ alloys,
   Bhargab Deka, Dibyashree Chakraborty and A. Srinivasan, **Physica B: Cond. Matter.** 448 (2014) 173.

3. Magnetic and structural properties of $(Ru_{1-x}Co_x)_2FeSi$ alloys,
   Bhargab Deka and A. Srinivasan, **Physica B: Cond. Matter**. 476 (2015) 118.

4. Search for fully compensated ferrimagnet in Co substituted Mn_2VGa alloy,
   Bhargab Deka, R. K. Singh, A. Srinivasan, **J. Magn. Magn. Mater.** 395 (2015) 240.

5. Experimental and *ab initio* studies on sub-lattice ordering and magnetism in $Co_2Fe(Ge_{1-x}Si_x)$ alloys,
   Bhargab Deka, Ashis Kundu, Subhradip Ghosh and A. Srinivasan, **J. Appl. Phys.** 118 (2015)133906.

6. Effect of Co substitution for Mn on spin polarization and magnetic properties of ferromagnetic Mn_2VAl ,
   B. Deka, A. Srinivasan, R. K. Singh, B. S. D. Ch. S. Varaprasad, Y. K. Takahashi and K. Hono, **J. Alloys Compd.** 662 (2016) 510.

7. Effect of electron-electron correlation and site disorder on the magnetic moment and half metallicity of $Co_2FeGa_{1-x}Si_x$ alloys,
   Bhargab Deka, Ashis Kundu, Subhradip Ghosh and A. Srinivasan, **Mater. Chem. Phys.** (Accepted) doi: 10.1016/j.matchemphys.2016.04.071.

Paper presented in conference:

1. Magnetic properties of $Co_2Fe(Ga_{1-x}Si_x)$ alloys, International Conference on Magnetic Materials and Applications (MAGMA 2013)
   Bhargab Deka, Dibyashree Chakraborty and A. Srinivasan.
2. Magnetic properties of $Ru_2Fe(Si_{1-x}Ge_x)$ alloys, Condensed Matter Days (CM Days) 2012
   Bhargab Deka, Rahul Das and A. Srinivasan.
3. Magnetic properties of Ruthanium based Heusler alloys, 5th IEEE magnetic Society Summer School 2012
   Bhargab Deka and A. Srinivasan.
4. Magnetic properties of $Ru_2MnSi(Ge)$ alloys, Condensed Matter Days (CM Days) 2011
   Bhargab Deka, Rahul Das and A. Srinivasan.

***** *****